Vol. 38 / 1&2
January, 2026

ISRAPS Bulletin

'FRONTIERS IN OPTOELETRONICS AND FUNCTIONAL MATERIALS'

Guest Editor
Dr. Aruna kumar Mora

A Publication of
Indian Society for
Radiation and Photochemical Sciences

Asmi Analytical

304, Srusti vihar, Near Vasant Vihar Club, Phokharan Road No-2 ,Thane West
Mumbai 400610 Email :-asmianalytical@gmail.com
Mobile 7738087733/7798997733

Contact us for

- CDS Analytical products Pyrolizer,Thermal Desorber, Purge & Trap
- Gas Chromatography accessories & Consumables.
- High Pressure & High Temperature Catalytic Reactors.
- Gas Generators and Chromatography Calibration Standards.
- Advance Training on GC and GC Analyzers

India Distributer for CDS analytical USA

https://www.cdsanalytical.com/

CDS Analytical USA products

CDS 4000
CDS's most cost effective single temperature Pyroprobe.

CDS 6200
CDS's 6th Generation Pyroprobe with trapping capabilities for reactant gas apps.

Autosampler Module
CDS's autosampler module with Dynamic Loading to improve productivity for any 6000 series pyroprobe.

CDS 6150
CDS's 6th Generation Pyroprobe with up to 10 programmed temperature steps.

CDS HPR
CDS's HPR Pyroprobe allows pyrolysis at elevated pressure with built-in reactor.

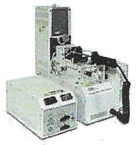

Photoprobe

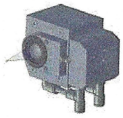

Photoprobe is a device that irradiates sample in the Drop In Sample Chamber with high intensity UV light

Purge and trap, Thermal Desorber, Autosamplers

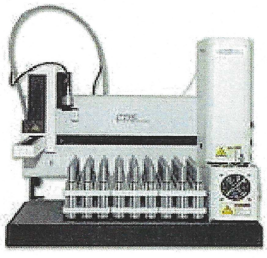

Message from the President and Secretary, ISRAPS

Dear ISRAPS Members,

Greetings from the Executive Council of ISRAPS!

We wish you all a very Happy New Year 2026 and take this opportunity to acknowledge the contributions of all our members towards activities of ISRAPS.

At the beginning of the year, the Trombay Symposium on Radiation & Photochemistry (TSRP-2026), one of the most important events organized by ISRAPS, is being held at the DAE Convention Centre, Bhabha Atomic Research Centre, Mumbai during January 06–10, 2026. The special issue of the ISRAPS bulletin, released on this occasion, is a compilation of articles on recent developments in the field of optoelectronics and functional soft materials contributed by eminent scientists invited to TSRP-2026. The Executive Council (EC) of ISRAPS thanks Dr. Aruna Kumar Mora, Guest Editor of this special issue, for his efforts in bringing out a bulletin containing seven articles of varied interest within the realm of radiation and photochemical sciences. We also acknowledge the support of all contributors for making this special issue highly informative.

One of the mottos of ISRAPS is the dissemination of recent advances in the fundamental research areas of radiation and photochemical sciences, and their applications in allied fields such as spectroscopy, atmospheric chemistry, materials science, radiation biology, and related subjects. In this regard, ISRAPS has been actively involved in organizing discussion meetings and symposia. This year, the National Symposium on Radiation and Photochemistry (NSRP-2025) was organized at the National Institute of Science Education and Research (NISER), Bhubaneswar, Odisha during January 23–25, 2025. The symposium was a grand success, and young researchers were highly enthusiastic in sharing their research work through oral and poster presentations. The EC thanks all participants and the organizing team from NISER and BARC for their contributions to the success of NSRP-2025.

A one-day discussion meeting on “New Frontiers of Radiation Processes in Polymers, Paints and Nanocomposites” was organized on July 19, 2025, at the Institute of Chemical Technology (ICT), Mumbai. The EC thanks Prof. Anagha S. Sabnis (ICT), as well as all speakers and participants, for contributing to the success of this meeting.

We invite scientists and students working in the fields of radiation and photochemical sciences and allied areas to become members of ISRAPS and contribute to the growth of its activities across India. We express our sincere gratitude to each and every member of ISRAPS for their support and look forward to their continued cooperation in the future endeavours of the society.

Dr. A.C. Bhasikuttan
President, ISRAPS

Dr. P. Mathi
Secretary, ISRAPS

ISRAPS Bulletin

A Publication of
Indian Society for Radiation and Photochemical Sciences

Editor's Desk...

I am delighted to present this special issue of the ISRAPS Bulletin, dedicated to 'Frontiers in Optoelectronics and Functional Soft Materials' marking the occasion of TSRP-2026. For thirty years, this symposium has united the global research community. Upholding the ISRAPS tradition, it is an honor to guest-edit this volume, which highlights cutting-edge developments in radiation and photochemical science.

In this edition with seven articles, we are pleased to present a diverse collection of articles highlighting significant strides in advanced instrumentation, functional materials, and therapeutic applications. This issue begins by detailing the indigenous dual-target, dual-laser cluster beam facility, which leverages photoionization spectroscopy and DFT to uncover molecular-level insights into catalysis and bond activation in metal clusters. Comprehensive characterization of ultrafast fiber lasers spanning 1 μm to 2 μm is presented, highlighting their robustness and efficiency for applications in nonlinear photonics and biomedical imaging.

Energy and sustainability remain central themes. Readers will find a comprehensive review of next-generation OLEDs focusing on TADF and color purity, alongside an investigation into singlet fission dynamics in anthracene-based materials aimed at boosting solar cell efficiency. The article on CuNCs (low stability, weak PL) by detailing strategies like supramolecular assembly and triplet-state harvesting to control structure-property relationships for photonics/catalysis.

Finally, the issue addresses chemical innovation for specialized environments. We discuss the radiation stability of Deep Eutectic Solvents (DESs), identifying choline acetate-based systems as robust, green alternatives for nuclear applications. This is paired with promising biomedical research on selenium-functionalized biopolymers, which demonstrates significant potential as anticancer and radio-sensitizing agents. Together, these contributions underscore the pivotal role of precise molecular engineering and advanced spectroscopy in addressing contemporary scientific challenges.

On behalf of ISRAPS, I sincerely acknowledge the cooperation of all the contributors, and we hope you enjoy this enlightening edition. I also thank ISRAPS for entrusting this editorial responsibility to me.

Dr. Aruna Kumar Mora Joined Bhabha Atomic Research Centre, Mumbai, India after graduating from BARC training school. He completed M. Sc. in chemistry from University of Hyderabad in 2009. He received his Ph. D. degree in 2017 from Homi Bhabha National Institute, Mumbai, for his work on ultrafast structural dynamics in amyloid fibril probes. Dr. Mora is recipient of University Gold Medal and Homi Bhabha Gold Medal and conferred with young scientist award by the Department of Atomic Energy in 2017 and by the National Academy of Sciences, India in 2021. His current research interest includes developing bio sensors, 2DIR spectroscopy and Ultrfast spectroscopy of complex organic and inorganic materials.

INDIAN SOCIETY FOR RADIATION AND PHOTOCHEMICAL SCIENCES (ISRAPS)

EXECUTIVE COUNCIL (2024-2026)

President

Dr. A. C. Bhasikuttan

Vice-Presidents

Prof. Anindya Dutta
Dr. Yatender K. Bhardwaj

Secretary

Dr. P. Mathi

Jt. Secretary

Dr. Beena G. Singh

Treasurer

Dr. Sumana Sengupta

Executive Members

Dr. Atanu Barik	Prof. Shamik Chakraborty	Dr. Sharmistha Dutta Choudhury
Dr. Awadhesh Kumar	Dr. Amit Kunwar	Dr. Jyotirmayee Mohanty
Dr. Sukhendu Nath	Dr. Chandra N. Patra	Dr. R. Puspalata
Dr. Madhab C. Rath	Prof. Geeta K. Sharma	Dr. V. Sudarsan
	Dr. Ankur Saha	

Co-opted Members

Dr. Nihrendu Choudhury	Prof. Hirendra N. Ghosh	Dr. Narender K. Goel
Prof. Sriram K. Gundimeda	Dr. Manoj Kumbhakar	Prof. Avinash Kumbhar
Dr. Nandita Maiti	Prof. Jai P. Mittal	Prof. Tulsi Mukherjee
Prof. Prakash D. Naik	Prof. Anil K. Singh	Prof. Avesh K. Tyagi

Web Master

Dr. Abhishek Das and Shri. Subhamoy Saha

Contact details:
C/o Radiation & Photochemistry Division
Bhabha Atomic Research Centre, Mumbai-400085
E-mail: israps.secretary@gmail.com
Telephone:(022)- 25593771/25592668/25590302

Contents

Message from President & Secretary, ISRAPS	i
Editor's desk	iii
Structure and Reactivity of Rare-Earth Metal Clusters Investigated Using an Indigenously Built Cluster Beam Facility at BARC *Soumen Bhattacharyya*	1
Advances in Ultrafast Fiber Laser Architectures for Real-time Elemental Analysis *J. Dey, S. Maity, U. K. Samanta, A. M. Mullick, S. D. Chowdhury, D. Pal and A. Pal.*	7
Molecular Structural Correlation with Singlet Fission Dynamics and Yield: Case Studies on Anthracene Based Singlet Fission Materials *B. Manna, A. Nandi and R. Ghosh*	18
A short review on current strategies for development of emitters for efficient OLED *K.V. Barhate and N. Agarwal*	26
Spectroscopic Signatures of Copper Nanoclusters: Assembly, Intercluster Conversion, and Excited-state Dynamics *S. Agrawal and S. Mukherjee*	35
Deep Eutectic solvents and ionizing radiation: An overview of generation of highly energetic species and search of a radiation stable DES *Laboni Das*	51
Synthesis and Biological Activities of Selenium Functionalized Biopolymers *M. Nayak, J. Aishwarya, B.G. Singh, A. Bari and, A. Kunwar*	62

Structure and Reactivity of Rare-Earth Metal Clusters Investigated Using an Indigenously Built Cluster Beam Facility at BARC

Soumen Bhattacharyya
Atomic & Molecular Physics Division (A&MPD),
Physics Group, Bhabha Atomic Research Centre, Trombay, Mumbai 400 085
E-mail: sbhatt@barc.gov.in

Abstract

Metal clusters—aggregates comprising a few to several tens of atoms—bridge the molecular and condensed phases, enabling the exploration of size-dependent properties under controlled gas-phase conditions. An indigenously developed dual-target, dual-laser vaporization supersonic cluster beam facility at the Atomic & Molecular Physics Division (A&MPD), Bhabha Atomic Research Centre (BARC), has opened new avenues for investigating metal, bimetallic, alloy, and metal oxide clusters, focusing on their structures and reactivity. Using threshold photoionization spectroscopy coupled with density functional theory (DFT), we have established the geometric structures, electronic properties, bonding characteristics, and charge-transfer behavior of small clusters of lanthanum (La_n), lanthanum monoxide (La_nO), yttrium monoxide (Y_nO), and yttrium oxides (Y_nO_2). The facility has further enabled studies on small-molecule activation, including O_2 dissociation by yttrium oxide clusters and NH_3 dehydrogenation by early transition-metal clusters. This article summarizes the experimental setup and major scientific outcomes, highlighting geometric and electronic structure evolution, ionic–covalent bonding cooperativity in monoxide clusters, and cluster-size-dependent oxygen and ammonia activation mechanisms.

1. Introduction

Metal clusters are atomically precise aggregates of a few to several tens of atoms whose properties differ fundamentally from their bulk counterparts. In this quantum size regime, where each atom significantly influences structure and reactivity, the concept of "each atom counts" aptly describes their behavior. Since the pioneering work of Smalley and co-workers[1] in the 1980s—who produced supersonic beams of metal clusters using laser vaporization—cluster science has evolved into a vibrant field linking molecular and condensed-matter domains.[2] Discoveries of "magic-number" clusters in alkali and coinage metals[3] led to the formulation of shell models and electron-counting rules, laying the foundation for understanding stability and bonding at the nanoscale.

Beyond monometallic systems, bimetallic and alloy clusters provide model systems for studying how atomic-scale interactions evolve toward bulk metallic behavior. They also serve as building blocks for functional nanomaterials with applications in catalysis[4], magnetism, and optoelectronics. Achieving precise control over cluster composition and size is essential for exploring these size-dependent phenomena and for establishing reliable structure–property relationships.

Rare-earth metal oxides such as La_2O_3 and Y_2O_3 are technologically important as catalyst supports, high-k dielectrics, optical materials, and chemical sensors. Understanding their behavior requires probing the smallest structural units—metal and metal oxide clusters—where the addition or removal of a single atom can drastically alter magnetism, reactivity, and electronic structure. However, experimental data on neutral rare-earth clusters have remained scarce, mainly due to their high vaporization temperatures and complex electronic correlation.

To overcome these challenges and establish indigenous capability, a laser-vaporization supersonic cluster beam facility was conceived, designed, and built at the Atomic & Molecular Physics Division (A&MPD), Bhabha Atomic Research Centre (BARC).[5] This setup enables controlled generation, cooling, and mass-spectrometric detection of pure metals, bimetals, alloys, semiconductor, and metal oxide clusters and new nanomaterials that are not stable in bulk form. The setup operates on the principle of laser ablation of a metal target followed by supersonic expansion of the ablated plasma in a pulsed carrier gas (typically helium). Clusters form through cooling and condensation within the source channel and emerge as a collimated beam cooled to ~30–40 K.[6] The facility allows atomic-level precision in cluster synthesis, mass selection of specific clusters, and a range of laser spectroscopic and mass-spectrometric investigations, including photoionization, photofragmentation, and gas-phase chemical reactions. Preformed clusters can also be deposited on substrates for further studies.

This article presents an overview of the indigenous cluster beam facility, along with representative scientific results on lanthanum and yttrium clusters and their oxides, highlighting the evolution of structure, bonding, and reactivity in these rare-earth systems.

2. Development of an Indigenous Metal Cluster Facility

The metal cluster beam facility at A&MPD, BARC (Figure 1) operates on the principle of laser vaporization and supersonic expansion for producing metal and metal oxide clusters under controlled gas-phase conditions. The method involves ablating a solid metal target with the second harmonic (532 nm) of a pulsed Nd:YAG laser (pulse energy 10–25 mJ, duration 5–8 ns) in the presence of a pulsed helium carrier gas. The ablated metal atoms are rapidly cooled and condensed within a cluster formation channel, forming dimers, trimers, and larger aggregates through three-body collisions assisted by helium. The helium atoms act as a third body to remove condensation heat and promote sequential cluster growth. The resulting clusters emerge in a supersonic beam cooled to a translational temperature of about 30–40 K, providing atomic-level control over cluster composition and size.

The cluster source employs dual-target, dual-laser vaporization, allowing the formation of bimetallic clusters with tunable stoichiometry.[5,6] The design incorporates a movable sample holder carrying two adjacent 1 mm-thick metal foils (25 × 7 mm^2), pressed against a specially designed cooling block mounted on a pulsed molecular beam valve. The gas flow and laser channels are arranged orthogonally, enabling precise overlap of the ablation plume with the carrier gas pulse. The source can be cooled down to liquid nitrogen temperatures, improving cluster yield and stability.

The beam transport system consists of a series of differentially pumped chambers maintained at base pressures of ~5×10^{-8} mbar using turbomolecular and dry roots pumps. The cluster beam is skimmed and directed into the interaction region of a custom-built reflectron time-of-flight mass spectrometer (Re-TOFMS) for mass analysis. Clusters are produced in neutral, cationic, and anionic forms; neutral clusters are probed using photoionization at the center of the TOF ion source by nanosecond laser pulses from either excimer lasers (193 nm, 157 nm) or a tunable optical parametric oscillator (OPO). The resulting ions are accelerated, mass-separated,

Figure. 1. Metal cluster laboratory at A&MPD, BARC.

and detected on a multichannel plate detector, producing high-resolution mass spectra recorded on a fast 1 GHz digital oscilloscope.

The optimization of helium pulse duration (270–320 µs), gas backing pressure (~10 bar), laser pulse energy (10–15 mJ), and nozzle geometry (25 mm × 3 mm) enabled the successful production of clusters of a series of transition metals like Ti, V, Co, and Ni and rare earth elements like Y, La and Ce, their oxides, and a few bimetallic clusters of these elements.

3. Cluster Growth & Stability: Mass spectrometric characterization

Mass spectrometric investigations of lanthanum (La_n), yttrium (Y_n), and their oxide clusters (La_nO_m, Y_nO_m) reveal broad size distributions without pronounced "magic-number" intensities. Figure 2 displays the mass spectrum of La_n, n = 1–50, clusters. As mentioned, no particularly enhanced intensity was observed for any specific cluster size[5], implying the absence of "magic-number" stability predicted theoretically for La_7 and La_{13}.[7] This indicates that, unlike alkali or coinage metal clusters, the rare-earth systems do not exhibit electronic shell closures. Instead, their bonding and stability are primarily governed by localized metal d-electrons, leading to complex size-dependent variations in abundance.

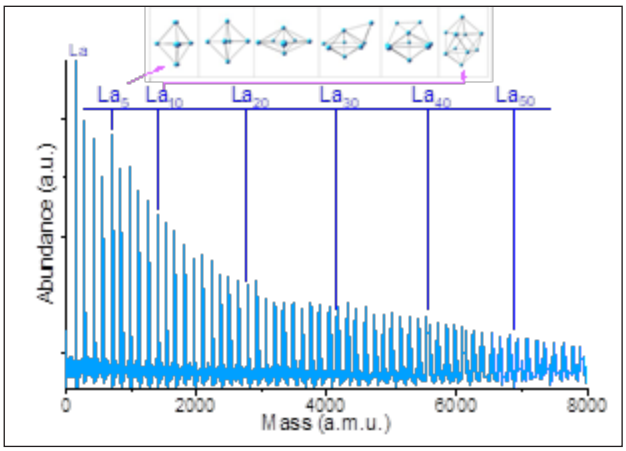

Figure 2. Mass abundance spectrum of lanthanum clusters La_n (n = 1–50).

The mass spectra of yttrium oxide clusters (Figure 3) recorded under low oxygen-seeding conditions show that monoxides (Y_nO) dominate for small cluster sizes, while higher oxides appear with decreasing abundance.[8] Interestingly, the pattern of Y_nO_m clusters do not follow a simple sequential addition of oxygen atoms with increasing m. Even and odd oxide clusters coexist, suggesting that both molecular and dissociative oxygen chemisorption processes contribute to cluster growth. Increasing oxygen concentration beyond a few percent suppresses cluster formation, reflecting the sensitivity of the growth process to oxidation conditions. These results demonstrate that growth of rare-earth oxide clusters is non-sequential and composition-dependent, highlighting the intricate interplay between metal–oxygen bonding and cluster stability in the gas phase.

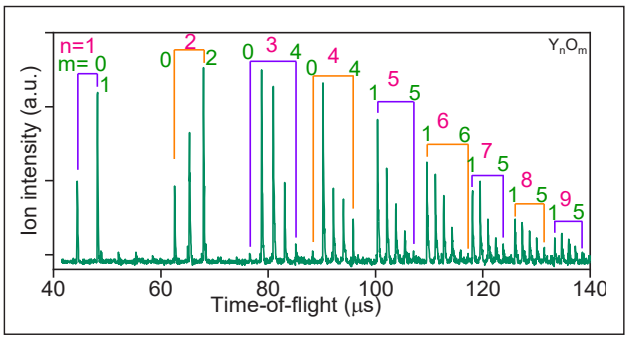

Figure 3. Mass spectrum of Y_nO_m clusters.

4. Structure: A Combined Experimental–Theoretical Approach

Establishing the ground-state geometric structure of a cluster is crucial because its reactivity, magnetism, and optical behavior strongly depend on atomic arrangement in this non-scalable size regime. Direct structural determination is not feasible under low-density gas-phase conditions; therefore, a synergistic combination of experiment and theory is required to uncover reliable structure–property relationships.

The key experimental observable for neutral clusters is the adiabatic ionization energy (AIE)—the minimum photon energy

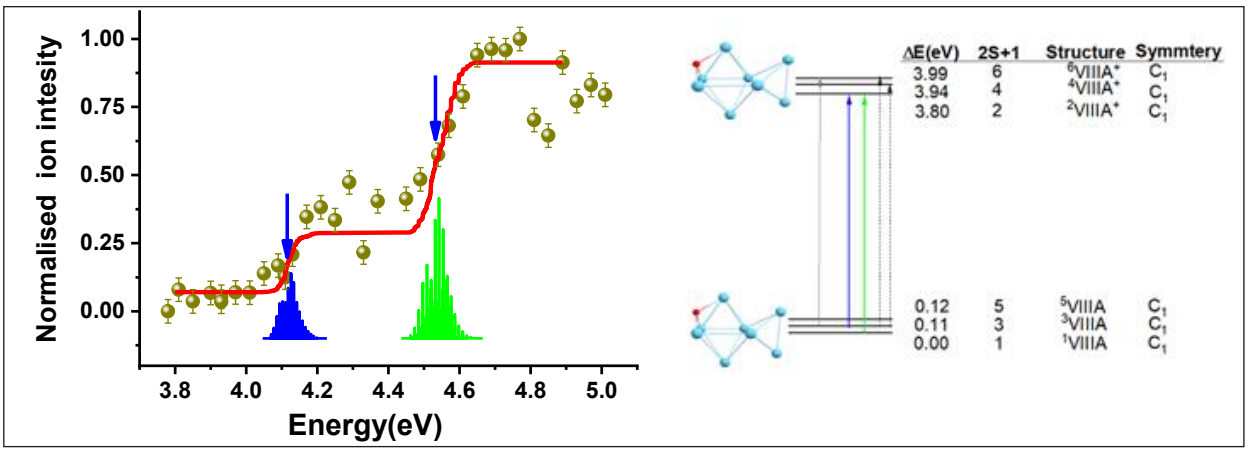

Figure. 4. Photoionization efficiency (PIE) spectrum of La_8O cluster. Experimentally recorded and calculated PIE spectra are shown as dots and solid lines, respectively.

needed to ionize a cluster. This is obtained from threshold photoionization spectroscopy, where the photoionization efficiency (PIE) spectrum—ion signal versus photon energy—reveals the ionization threshold.

In parallel, density functional theory (DFT)-based global structural searches are performed to identify possible low-energy isomers on the potential energy surface. Theoretical AIEs and simulated PIE spectra are then computed for these candidate structures using Franck–Condon (FC) factor calculations.[9] Comparison between measured and simulated PIE spectra enables unambiguous assignment of the correct ground-state geometry.

As an example, excellent agreement between calculated and experimental PIE spectra for the La_8O cluster confirmed its ground-state structure as the low-lying 8a isomer (Figure 4), providing a reliable framework for interpreting its bonding and reactivity.

By using this methodology, the structure of small La_n,[5] Y_n, La_nO,[9] Y_nO[8] clusters of n up to 12 atoms have been established. The geometric structures of small La_n and Y_n clusters exhibit a strong competition between icosahedral and octahedral growth motifs. Icosahedral packing, typical of van der Waals–bound systems such as rare gases or alkaline-earth clusters (ns^2 configuration), favors compact, close-packed geometries. In contrast, the emergence of octahedral or cubic elements reflects the influence of directional d-orbital bonding, characteristic of transition metals. Owing to their mixed s–d valence character, La_n and Y_n clusters display this interplay between close-packed and directional bonding, resulting in size-dependent structural transitions as the clusters grow.[10] Their monoxide clusters are 3-dimensional from n≥ 3. The O atom stays outside, bridging a triangular face of pure metal (La_n and Y_n) clusters (Figure 5).

5. Chemical bonding, charge transfer and photoionization in La and Y monoxide clusters

The chemical bonding between the metal atoms is mostly covalent for the smaller clusters up to 6 atoms, and for the larger clusters, some

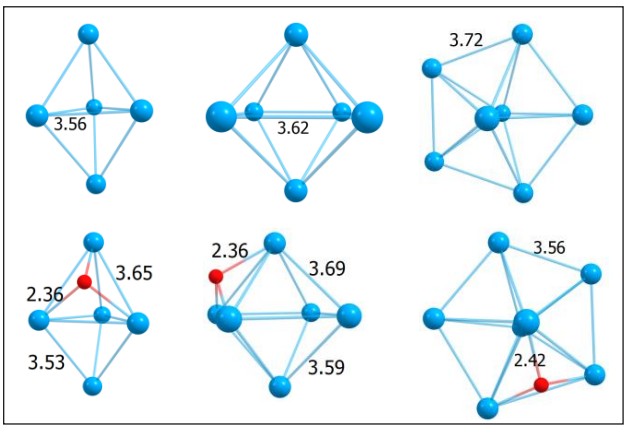

Figure 5. *The first and second rows display the ground state structures of La_n and La_nO (n = 5−7) clusters.[5,9] Bond lengths are in Å.*

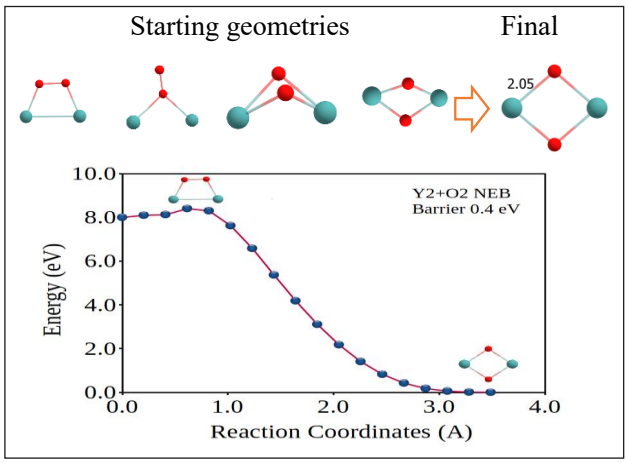

Figure 6. The first row shows few initial structures of Y_2O_2 which is like O_2 absorbed on Y_2 converged to Y_2O_2 ground state. The second row depicts the reaction of Y_2+O_2 through a transition state to the final product Y_2O_2 ground state.[12]

ionic interaction is detected. The chemical bonding between the metal (La and Y) and O atoms is mostly ionic. The excess charge on the oxygen atom is around 1.4e, transferred from the yttrium atoms bonded with it. Yttrium atoms are mostly covalently bonded. However, for the bigger clusters, free charges of both polarities appear on yttrium atoms that are not bonded with oxygen, indicating ionic interactions. Frontier orbitals consist of mainly delocalized 4d electrons with some 5s contributions, forming Y–Y bonding interactions, but with little contribution and zero contribution from the oxygen orbitals, regardless of the cluster size.[8]

Interesting conclusions are drawn from the photoionization. It was previously believed that threshold photoionization in Y_nO clusters occurs from a localized 4d orbital rather than a delocalized band derived from 5s valence electrons.[11] In contrast, we found that the lost electron of Y_nO^+ comes mostly from a delocalized metal-based 5s orbital. As the number of Y atoms per cluster increases from n=5, the lost electron of Y_nO^+ comes from the s-d hybridized orbitals of all the yttrium atoms.[8] The nature of chemical bonding, average bond lengths, and HOMO−LUMO energy gaps indicate that these clusters are non-metallic in the size range of up to 12 atoms studied by us. However, the onset of the evolution of bulk-like behaviour starts with a 7-atom oxide cluster.

6. Activation of small molecules like O_2 and NH_3 by isolated metal clusters

Combined threshold photoionization measurements and DFT calculations show that small yttrium oxide clusters (Y_mO_n) readily activate molecular oxygen. While intact O_2 adsorption is generally unstable, O_2 dissociates spontaneously when it binds to low-coordinated sites (corners or edges) of Y_n clusters. Nudged-elastic-band calculations reveal a barrierless or low-barrier pathway leading to Y_nO_2 formation, driven by charge transfer from Y to O_2, weakening the O–O bond and enabling the two O atoms to migrate to different binding sites (Figure 6). TDOS/PDOS analyses indicate enhanced electronic density near the Fermi level during this process, consistent with strong Y–O interaction and high reactivity toward O_2 activation.[12]

Ammonia activation studies using laser-vaporized early transition-metal clusters (Ti, V, Fe, Co, Ni) exhibit distinct metal- and size-dependent reactivity trends.[13] Ti clusters show strong nitride formation, producing $(TiN)_n$ species efficiently. V_n and Fe_n clusters predominantly form mononitrides, with NH_3 dehydrogenation efficiency varying with cluster size and charge state. Co_n clusters display limited reactivity, showing mostly molecular adsorption and partial N–H bond cleavage. In contrast, Ni_n clusters exhibit extensive NH_3 uptake and release $Ni^+ + H_2$, indicating complete dehydrogenation pathways and efficient hydrogen elimination.

Together, these results highlight how atomic-scale variations in metal electronic structure govern the activation of small molecules. Rare-earth clusters excel at O_2 dissociation, while transition-metal clusters show a rich spectrum of NH_3 activation and nitride formation mechanisms, offering molecular-level insight into catalytic processes relevant to oxidation and hydrogen-carrier chemistry.

7. Summary and Conclusion

The indigenously built dual-target, dual-laser cluster beam facility at A&MPD, BARC has enabled systematic investigations of the

geometric structure, electronic properties, and reactivity of rare-earth and transition-metal clusters under well-defined gas-phase conditions. The combination of threshold photoionization spectroscopy and DFT-based global structural searches provides a powerful framework for determining ground-state structures and uncovering size-dependent trends that are inaccessible by experiment alone.

For lanthanum and yttrium clusters, the interplay between compact icosahedral motifs and directional d-orbital–driven geometries govern structural evolution. Their monoxide clusters show clear signatures of ionic–covalent cooperativity and charge-transfer–mediated stabilization, while maintaining overall non-metallic character up to medium cluster sizes. Rare-earth oxide clusters also exhibit efficient activation of O_2, with low-coordinated metal sites promoting spontaneous O–O bond cleavage through charge transfer and adsorption-driven rearrangement.

Transition-metal clusters display distinct patterns in ammonia activation, ranging from strong nitride formation in Ti clusters to stepwise dehydrogenation and H_2 release in Ni clusters. Together, these studies demonstrate how precise cluster formation, spectroscopic control, and quantum-chemical modeling can provide molecular-level insights into catalysis, oxidation, and hydrogen-carrier chemistry.

The indigenous facility in A&MPD, BARC, has thus established a foundation for advanced cluster science and opens the door to future research on supported clusters, size-selected catalysis, hydrogen storage materials, and new functional nano-architectures.

Acknowledgements

The author acknowledges the support of the Atomic & Molecular Physics Division, BARC, in the development and operation of the metal cluster facility. The work presented here benefited from contributions by several colleagues involved in cluster source design, mass spectrometry, laser spectroscopy, and theoretical calculations, whose collective efforts enabled the results summarized in this article.

References

(Endnotes)

1. T. G. Dietz, M. A. Duncan, D. E. Powers, R.E. Smalley, *J. Chem. Phys.* 74, (1981) 6511−6512.
2. A.-M. Hada, M. Lamy de la Chapelle, M. Focsan, S. Astilean, *Molecules* 30 (2025) 38489 (1-39).
3. W. D. Knight, K. Clemenger, W. A. de Heer, W. A. Saunders, M. Y. Chou, and M. L. Cohen, *Phys. Rev. Lett.* 52, (1984) 2141−2143.
4. T. Li, R. Zhang, N. Fang, Y. Shi, J. Li, C. Hea, Y. Chua, *Nanoscale*, 17 (2025) 9834-9869.
5. S. Bhattacharyya, D. Bandyopadhyay, S. Mukund, P. Sen, S.G. Nakhate, *J. Phys. Chem. A* 126 (2022) 3135-3144.
6. W. Bouwen, P. Thoen, F. Vanhoutte, S. Bouckaert,F. Despa, H. Weidele, R. E. Silverans, P. Lievens, *Rev. Sci. Instrum.* 71 (2000) 54−58.
7. D.-B. Zhang, J. Shen, *J. Chem. Phys.* 120, (2004) 5104−5109.
8. V. V. Deshpande, V. Chauhan, D. Bandyopadhyay, A. Anoop, S. Bhattacharyya, *Phys. Chem. Chem. Phys.* 26 (2024) 20123-20133.
9. S. Bhattacharyya, V. V. Deshpande, *J. Phys. Chem. A* 127 (2023) 7460-7469.
10. A. Lyalin, A. V. Solov'yov, W. Greiner, *Phys. Rev. A* 74, (2006) 043201−10.
11. M. Knickelbein, *J. Chem. Phys.* 102, 1 (1995).
12. V. V. Deshpande, D. Bandyopadhyay, V. Chauhan, G. Kumari, S. Bhattacharyya, Dalton Trans. 54 (2025) 6402-6410.
13. V. Chauhan, C. P. Bhat, V. V. Deshpande, D. Bandyopadhyay, S. Bhattacharyya, *J. Phys. Chem. A* 129 (2025) 8577-8584.

Dr. Soumen Bhattacharyya *obtained his M.Sc. in Physics from the University of Burdwan and joined the Bhabha Atomic Research Centre (BARC) in 1998 after graduating from the 41st batch of the BARC Training School. He received his Ph.D. from the University of Mumbai in 2007 and subsequently carried out postdoctoral research in the Clusters and Laser Spectroscopy group at KU Leuven, Belgium. His research interests include metal and metal-oxide cluster science, spectroscopy of jet-cooled molecules, and first-principles computational studies on molecular and cluster systems.*

Advances in Ultrafast Fiber Laser Architectures for Real-time Elemental Analysis

Jishnu Dey,[1,2] Subhranil Maity,[2] Uttam kumar Samanta,[3] Abdul Malek Mullick,[1] Sourav Das Chowdhury,[1] Debasis Pal,[1] Atasi Pal,[1,*]

[1]*Fiber Optics and Photonics Division, CSIR-Central Glass and Ceramic Research Institute, Kolkata – 700032, India*

[2]*Department of Physics, Jadavpur University, Kolkata – 700032, India*

[3]*Laboratory of Photonics, Physics Unit, Faculty of Engineering and Natural Sciences, Tampere University, 33720 Tampere, Finland*

**Corresponding Author Email: atasi.cgcri@csir.res.in*

Abstract:

Ultrafast fiber lasers generating fs-ps pulses have revolutionized time-resolved spectroscopy and nonlinear photonics by enabling direct observation of ultrafast photon–matter interactions, deep tissue imaging and precise micromachining. Evolving from conventional Ti:sapphire laser systems, fiber-based architectures offer compactness, thermal efficiency, and long-term stability. This article presents the design and comprehensive characterization of ultrafast fiber lasers operating at 1 μm, 1.55 μm, and 2 μm, each representing distinct physical and application advantages. While Yb-doped 1 μm systems provide high gain and power scalability for industrial and nonlinear optics, Er-doped 1.55 μm systems exploit the telecom low-loss window for spectroscopy and frequency metrology, and Tm/Ho-doped 2 μm systems enable various biomedical applications.

1. Introduction

The advent of ultrafast laser technology, producing pulses in the femtosecond (fs, 10^{-15} s) to picosecond (ps, 10^{-12} s) domain, has enabled the probing of fundamental steps in photon–matter interactions, including excited-state dynamics, electron transfer, and molecular rearrangement, with unprecedented temporal precision. The advent of femtosecond laser science dates back to the 1980s [1] while the introduction of Kerr-lens mode-locking (KLM) in Ti:sapphire lasers by Spence and Sibbett [2] revolutionized ultrafast photonics by providing a stable, broadband platform capable of generating pulses shorter than 100 fs. However, such bulk solid-state systems required critical optical alignment, precision cooling, and vibration isolation—limiting their widespread use in long-term analytical and industrial environments. In the ultrafast laser domain, fiber lasers have traditionally represented a trade-off between power and compactness—offering a robust, alignment-free platform for fs-pulse generation with superior stability and compactness, been inherently been limited in achievable pulse energy. Fiber lasers began attracting attention in the late 1990s as a promising alternative to Ti:sapphire systems, primarily due to their optical fiber waveguide geometry, high optical gain, and excellent heat dissipation. Early experiments using Erbium (Er)-doped silica fibers, operating near 1.55 μm, achieved ps-pulse generation through passive mode-locking using nonlinear polarization evolution (NPE) or semiconductor saturable absorber mirrors (SESAMs). The NPE mechanism exploited the intensity-dependent refractive index (Kerr effect) to induce self-amplitude modulation within the fiber cavity, achieving stable mode-locking without external modulators [3]. These early Er-doped systems, although limited to modest pulse energies (~1 nJ) and milliwatt average powers, demonstrated that fiber-integrated ultrafast pulse generation could achieve remarkable stability

and repeatability along with the compactness and robustness critical for field-deployable analytical instruments. Over time, ultrafast fiber lasers incorporate multiple loop configuration, environmental isolation, and all-polarization-maintaining (PM) fiber designs, achieving long-term operational stability with sub-0.5% pulse-to-pulse energy fluctuations [4]. This robustness is particularly important in analytical spectroscopy, where reproducibility and signal fidelity are critical for quantitative accuracy. Their turnkey operation has also made them attractive for laboratory automation, remote radiation monitoring, and field-deployable photochemical diagnostics, far beyond the practical scope of traditional Ti:sapphire systems [5].

This article reviews recent advances, at CSIR-CGCRI, in the design and characterization of ultrafast fiber lasers operating at 1 μm, 1.5 μm, and 2 μm, integrating simulation and experimental studies for performance optimization across application domains. Yb-doped fiber lasers at 1 μm offer high gain efficiency, excellent thermal handling, and scalability for industrial micromachining, biomedical imaging, and nonlinear frequency conversion. Er-doped systems at 1.55 μm, aligned with the low-loss telecom window, enable ultrafast spectroscopy, optical frequency combs, and time–frequency metrology. Thulium/Holmium-doped fiber lasers at 2 μm leverage strong water absorption and atmospheric transparency for biomedical, surgical, and LIDAR applications. Through integrated simulation and experimental validation, these platforms advance the control of nonlinear pulse dynamics and enhance laser–matter interaction, enabling precise, high-speed spectroscopic diagnostics for elemental detection and related applications.

2. Ultrafast fiber laser configuration

Ultrafast pulse generation within optical fiber can be realized through active or passive mode-locking. Active mode locking [6], which employ electro-optic or acousto-optic modulators for amplitude or phase modulation, can achieve high repetition rates but typically generate ps-pulses and involve critical electronics control. In another way, passive mode-locking—based on saturable absorbers (SAs)—is favoured for its simplicity, compactness, and ability to achieve sub-100 fs pulses without external modulation. The SA mechanism relies on intensity-dependent transmission, where parameters such as modulation depth, saturation power, and recovery time govern pulse stability and duration. Depending on implementation, SAs can be physical or artificial. Physical SAs, including SESAMs [7,8], carbon nanotubes (CNTs), graphene, [8-10] and other two-dimensional (2D) materials [11], provide reliable, self-starting operation and wavelength selectivity, but are limited by material damage thresholds and fixed modulation parameters. In contrast, artificial SAs exploit the Kerr nonlinearity in fiber to emulate intensity-dependent loss. These include nonlinear polarization rotation (NPR) [7] and Sagnac loop–based interferometric schemes. Sagnac loop configurations incorporating nonlinear optical loop mirrors (NOLMs) [12-13] or nonlinear amplifying loop mirrors (NAbLMs) [14,15] achieve passive mode-locking through intensity-dependent interference between counter-propagating pulses. In the NAbLM, asymmetric nonlinear phase accumulation within the loop—due to gain or path length imbalance—enables constructive interference for high-intensity pulses and destructive interference for low-intensity noise, realizing effective saturable absorption. These architectures offer excellent environmental stability, high damage tolerance, and all-fiber integration, though stable self-starting operation requires careful optimization of loop phase bias and polarization state.

To understand how different fiber-laser platforms harness these mechanisms, it is useful to compare how the dispersion landscape and nonlinear dynamics shape their preferred mode-locking strategies. Each wavelength band has a characteristic dispersion profile and available gain media, which naturally guide the cavity design and pulse-shaping regime. As a result, ultrafast

Erbium-, Ytterbium-, and Thulium/Holmium-doped systems adopt distinct pulse-formation principles optimized for stability, energy scaling, and application-specific performance.

A. 1.55 µm wavelength region: Stretched pulse cavity design

Fiber lasers operating near 1.55 µm, typically using Er-doped fiber, are a cornerstone of telecommunications and mid-infrared nonlinear optics. In this wavelength region, ultrafast operation is commonly achieved using the stretched-pulse fiber laser design. The cavity is deliberately constructed with segments of anomalous-dispersion ($\beta_2 < 0$) and normal-dispersion ($\beta_2 > 0$) fiber, causing the pulse to periodically stretch and compress on each round trip. This controlled breathing of the pulse lowers its peak intensity inside the cavity, which in turn suppresses excessive nonlinear phase accumulation and supports stable operation at higher pulse energies. After external compression, such systems routinely produce sub-100 fs pulses. Because all components are fiber-integrated, the architecture is inherently alignment-free and mechanically robust, and the use of PM fiber further enhances long-term environmental stability.

B. 1 µm wavelength region: Dispersion-managed dissipative soliton mode-locking

Fiber lasers operating near 1 µm, primarily based on Yb-doped fibers play an increasingly important role in mid-infrared photonics, high-harmonic generation (HHG), and frequency-comb development. In this wavelength region, **dispersion-managed dissipative soliton** mode-locking has emerged as the preferred design strategy. By constructing the cavity entirely from fibers with normal group-velocity dispersion ($\beta_2 > 0$), the laser generates strongly chirped pulses that remain stable in the cavity and are subsequently compressed outside it. Mode-locking is achieved using fiber-integrated techniques such as saturable absorbers or nonlinear polarization evolution, providing robust self-starting operation. This regime supports high pulse energies with low phase noise—an essential requirement for coherent mid-IR sources, supercontinuum generation, micromachining and high-harmonic generation

C. 2 µm wavelength region: Solitonic mode-locked cavity design

Fiber lasers operating near 2 µm, primarily based on Tm- or Ho-doped fibers play an increasingly important role in mid-infrared photonics, high-harmonic generation (HHG), and frequency-comb development. The essential physics hinges on net anomalous dispersion within the laser cavity ($\beta_2<0$), balancing group velocity dispersion with nonlinear effects—primarily self-phase modulation (SPM). Mode-locking is typically achieved through fiber-integrated saturable absorbers or nonlinear polarization evolution, producing conventional solitons or in some case noise like pulses (NLPs) with pulse durations in the nanosecond to picosecond regime. At 2 µm, the naturally strong anomalous dispersion of available gain fibers readily supports clean, stable solitonic pulses, providing an excellent platform for coherent mid-IR sources, broadband supercontinuum generation, frequency combs, and high-harmonic generation toward the UV—ultimately enabling pathways to attosecond pulse generation.

2.1 Numerical simulation

Numerical simulation enables precise tuning of parameters for both physical SAs and artificial SAs, predicting pulse stability, duration, and self-starting behaviour for optimizing passively mode-locked fiber lasers. The understanding of the interplay between dispersion, nonlinearity, and saturable absorption accelerates the design of compact, robust ultrafast fiber lasers with controlled pulse dynamics. The system dynamics are modelled using the split-step Fourier method (SSFM) [16] to solve the nonlinear Schrödinger equation (NLSE) for passive fibers and the Ginzburg–Landau equation (GLE) for gain media as given by equation (1).

$$\frac{\partial A}{\partial z} = \frac{G}{2}A + \frac{G}{2\Omega_G^2}\frac{\partial^2 A}{\partial t^2} - i\frac{\beta_2}{2}\frac{\partial^2 A}{\partial t^2} + \frac{\beta_3}{6}\frac{\partial^3 A}{\partial t^3} + i\gamma$$
$$\left(1 + \frac{i}{\omega_0}\frac{\delta}{\delta t}\right) \times \left(A\int_{-\infty}^{\infty} R(\tau)|A(t-\tau)|^2\delta\tau\right) \quad (1)$$

$$T_{SA} = \frac{1}{2}\left[1 - dr\cos\left(\frac{\pi(1-\varphi)}{P_{sat}}A(t)^2 + \varphi\pi\right)\right] \quad (2)$$

$$T_{SA} = 1 - \frac{m}{(1+\frac{P}{P_{sat}})} \quad (3)$$

In the GLE, "A" represents the slowly varying field envelope, β_2 and β_3 denote the second- and third-order dispersion terms, γ is the nonlinear coefficient, and g_o is the small-signal gain. The gain bandwidth Ω is modelled as broad parabolic shape of 40 nm for the EDF. The NPR mechanism is represented by a sinusoidal transfer function T_{SA} given by equation (2), incorporating the PC-induced linear phase bias Φ, and saturation power P_{sat}. Equation (3) denotes the transfer function of a physical saturable absorber like SESAM [7]. For amplifier and compressor stages, third-order dispersion (TOD) and stimulated Raman scattering (SRS) are included to capture ultrafast nonlinear effects.

The seed laser model is evolved over 2000-5000 roundtrips to confirm convergence to a steady-state pulse. The simulation outputs the complex spectral envelope, which is then propagated through the amplifier and compressor fibers to predict optimal fiber lengths yielding minimal pulse width and sidelobe formation.

2.1 Experimental

2.2.1 Mode-locked laser operation at 1.55 µm

A compact, nonlinear polarization rotation (NPR) mode-locked fiber laser producing sub-100 fs pulses at 1.55 µm is experimentally demonstrated and numerically analysed. The all-fiber system, incorporating a self-starting NPR seed oscillator, an Erbium doped fiber amplifier (EDFA) and compressor fiber. It delivers pulses as short as 96.5 fs with a repetition rate of 88.24 MHz and average power of 61.2 mW. The design eliminates all free-space components, ensuring environmental stability, and compact integration. Numerical modelling using the split-step Fourier method (SSFM) accurately predicts fiber segment lengths and pulse evolution dynamics. The results confirm that an all-fiber NPR configuration can achieve transform-limited sub-100 fs pulses.

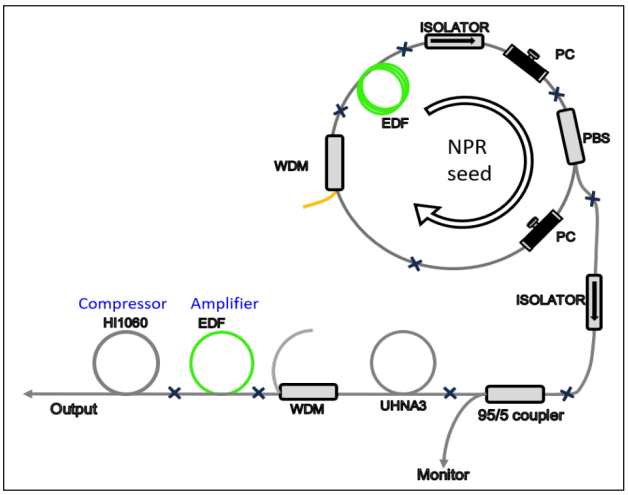

Figure 1: Schematic diagram of NPR laser configuration. WDM – Wavelength Division Multiplexer, PC – Polarization Controller, PBS – Polarization Beam Splitter

The schematic of that fiber laser architecture is shown in Fig.1. The seed cavity comprises 0.5 m of Er-doped fiber (Liekki Er40 4/125) with β_2 = +0.028 ps²/m, β_3 = −6.87×10⁻⁵ ps³/m, and nonlinear coefficient γ = 3.8 W⁻¹km⁻¹, connected to SMF-28e fiber (β_2 = −0.023 ps²/m, γ = 1.5 W⁻¹km⁻¹). A 980/1550 nm WDM couples the pump light, while two in-line polarization controllers (PCs), a polarization-independent isolator (PI-ISO), and a polarization beam splitter (PBS) complete the cavity. The PBS simultaneously acts as the output coupler and intra-cavity polarizer, eliminating the need for an additional coupler and polarizer and thus minimizing cavity length. Once the PCs are optimized at a fixed pump power of 40mW, the intra-cavity polarization evolution stabilizes, ensuring a repetitively self-starting NPR seed oscillator. The total cavity length is 2.31 m, corresponding to a fundamental repetition rate of 89.24 MHz and net cavity dispersion of −0.0183 ps² at 1550 nm. The seed output is

directed through a PI-ISO, a 95/5 coupler (both SMF28 fiber), with the 5% port as the tap to 30 cm of UHNA3 fiber and a WDM (OFS 980 fiber). For amplification a 3.35 m long EDF (same as seed) has been used which is spliced to the HI1060 compressor fiber. The length of the compressor fiber and UHNA3 was optimized through numerical simulation.

2.1.1 Mode-locked laser operation at 1 µm

A SESAM-based mode-locked seed oscillator followed by a chirped pulse amplification (CPA) has been designed using Yb-doped gain fiber for fs-pulse generation at 1 µm. The schematic of that fiber laser architecture is shown in Fig.2. The seed source is a SESAM-based linear-cavity Yb-fiber oscillator centered at 1064 nm, incorporating an 18 nm bandwidth chirped fiber Bragg grating (CFBG) with 15% reflectivity to provide intracavity dispersion control and establish a net positive cavity dispersion. The gain section consists of a 1.2 m ytterbium-doped single-clad fiber pumped at 976 nm through a wavelength-division multiplexer (WDM), while the SESAM with its sub-picosecond recovery time ensures fast response and reliable self-starting mode-locking. The oscillator produces strongly chirped pulses with a flat-topped, rectangular spectrum characteristic of dispersion-managed dissipative solitons, ideally suited for subsequent external compression.

The CPA stage follows a standard architecture comprising a core-pumped preamplifier, a fiber-based stretcher, and a double-clad large-mode-area ytterbium amplifier, forming an all-normal dispersion (ANDi) segment before culminating in a free-space diffraction-grating compressor. A polarization-insensitive isolator protects the seed, and a 99/1 coupler enables real-time monitoring.

The stretcher uses a 200 m length of HI1060 fiber to impart normal dispersion, while nonlinear effects in the preamplifier introduce controlled spectral broadening. A large-mode-area power amplifier built from 10/125 µm, NA = 0.08 double-clad Yb-doped fiber (LMA DC-YDF), boosts the pulse energy before the beam is collimated and directed into a Treacy-type compressor based on two 1200 lines/mm gratings operated near the Littrow configuration, which supply the anomalous dispersion necessary for complete chirp compensation. All the active fibers used in the setup were fabricated in-house at CSIR-CGCRI. The dispersion-managed seed laser produces dissipative soliton pulses centered at 1.064 µm with an 11 nm bandwidth and 0.88 nJ energy at 17.1 MHz. Following preamplification, stretching, cladding-pumped amplification, and Treacy-type grating compression, the system generates 350 fs pulses with 87.7 nJ energy and 1.5 W average power.

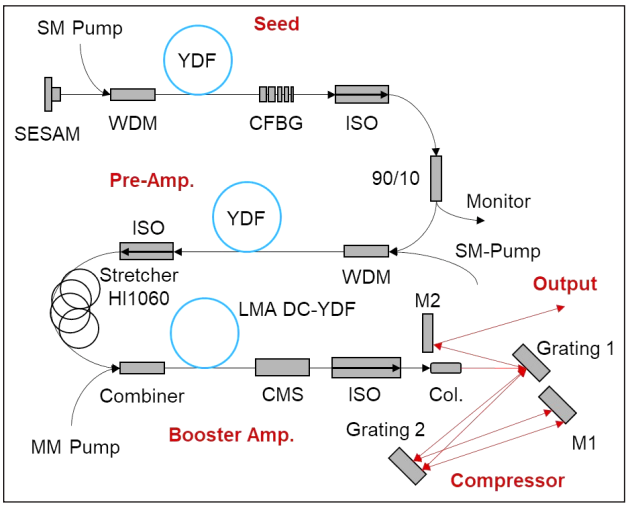

Figure 2: Schematic diagram of the developed fiber-CPA system. SM-Pump: Single Mode Pump; WDM: Wavelength Division Multiplexer; YDF: Yb-doped fiber (single clad); CFBG: Chirped Fiber Bragg Grating; ISO: Isolator; MM Pump: Multi-mode Pump; LMA DC-YDF: Large Mode Area Double clad YDF; CMS: Cladding Mode Stripper; Col: collimator; G1 and G2: Grating 1 and 2; M1 and M2: Mirror 1 and 2

2.1.2 Mode-locked laser operation at 2 µm

The design and detailed characterization of a Tm-doped fiber laser operating near 2 µm, passively mode-locked using a nonlinear absorbing loop mirror (NAbLM) is being reported. The architecture, as shown in Fig.3, exploits equal-power interference between counter-propagating waves within a loop

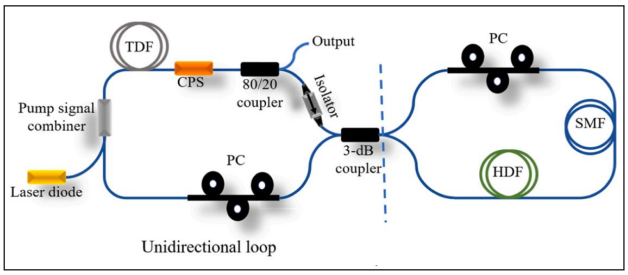

Figure 3: Schematic diagram of NAbLM-based mode-locked thulium-doped fiber laser, (b) Schematic diagram of NOLM-based mode-locked thulium-doped fiber laser PC: Polarization Controller, SMF: Single Mode Fiber, TDF: Thulium Doped Fiber, HDF: Holmium Doped Fiber, NAbLM: Nonlinear Absorbing Loop Mirror, CPS: Cladding pump stripper

containing an asymmetrically placed unpumped holmium-doped fiber acting as an absorber. This design offers enhanced modulation depth and extinction ratio compared to conventional nonlinear amplifying loop mirrors (NALM). The figure-8 laser consists of a unidirectional gain loop and a bidirectional NAbLM loop. The gain loop contains ~3 m of double-clad Tm-doped fiber forward-pumped at 793 nm with up to 15 W through a (2+1) ×1 combiner; a polarization-insensitive isolator enforces unidirectional operation, and an 80:20 coupler extracts the output. All components are fusion-spliced to minimize loss. The NAbLM loop incorporates 2 m of unpumped Ho-doped fiber as a saturable absorber and ~100 m of SMF-28 providing anomalous dispersion and nonlinear phase accumulation, with polarization controllers in each loop to set birefringence and phase bias. A 3 dB coupler splits and recombines counter-propagating waves to produce intensity-dependent interference for pulse shaping. The overall cavity length is ~116 m, yielding a 1.77 MHz repetition rate and a net anomalous dispersion of −9.35 ps² suitable for noise-like pulse generation. The laser generates stable broadband noise-like pulses (NLPs) centered at 2045 nm, with a repetition rate of 1.77 MHz and single-pulse energy of 141 nJ. The configuration demonstrates superior stability, high saturation power, and potential for high-energy ultrafast operation in the 2 µm regime, suitable for applications in spectroscopy, medical photonics, high harmonic generation (HHG) for attosecond science and mid-infrared nonlinear optics.

2.3 Results and discussion

2.3.1 Mode-locked laser operation at 1.55 µm

Stable mode-locking was obtained at a pump power of 40 mW, with the continuous-wave threshold at 20 mW and sustained mode-locking down to 35 mW due to hysteresis. The seed laser exhibited a distinct solitonic spectrum with Kelly sidebands and a 3 dB bandwidth of 13.98 nm, as shown in Fig. 4(a) while the pulse train recorded on a 20 GHz oscilloscope

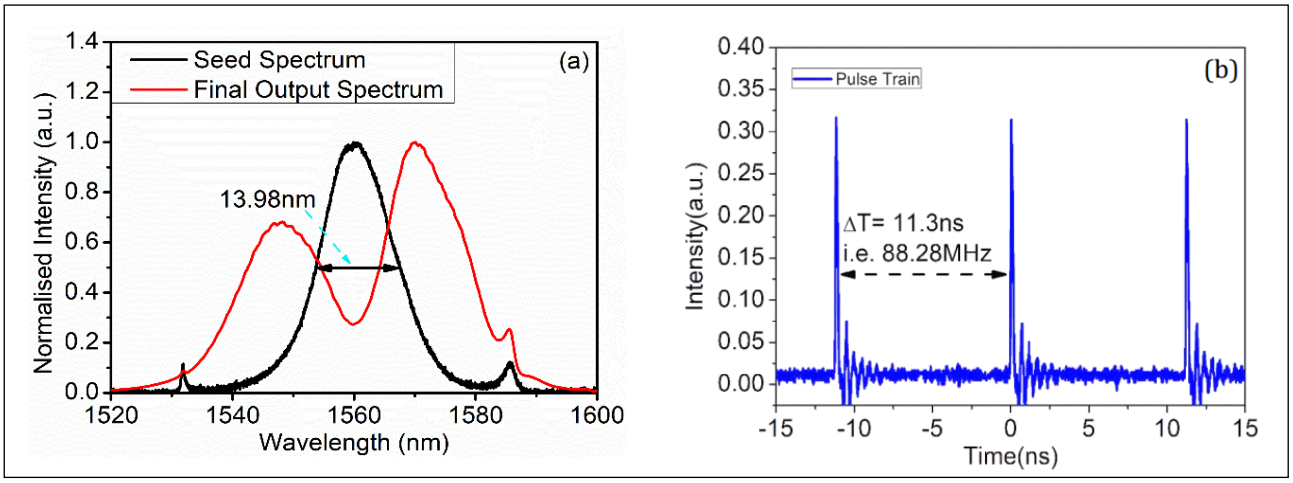

Figure 4: (a) Seed laser and final compressed pulse spectrum (b) Pulse Train

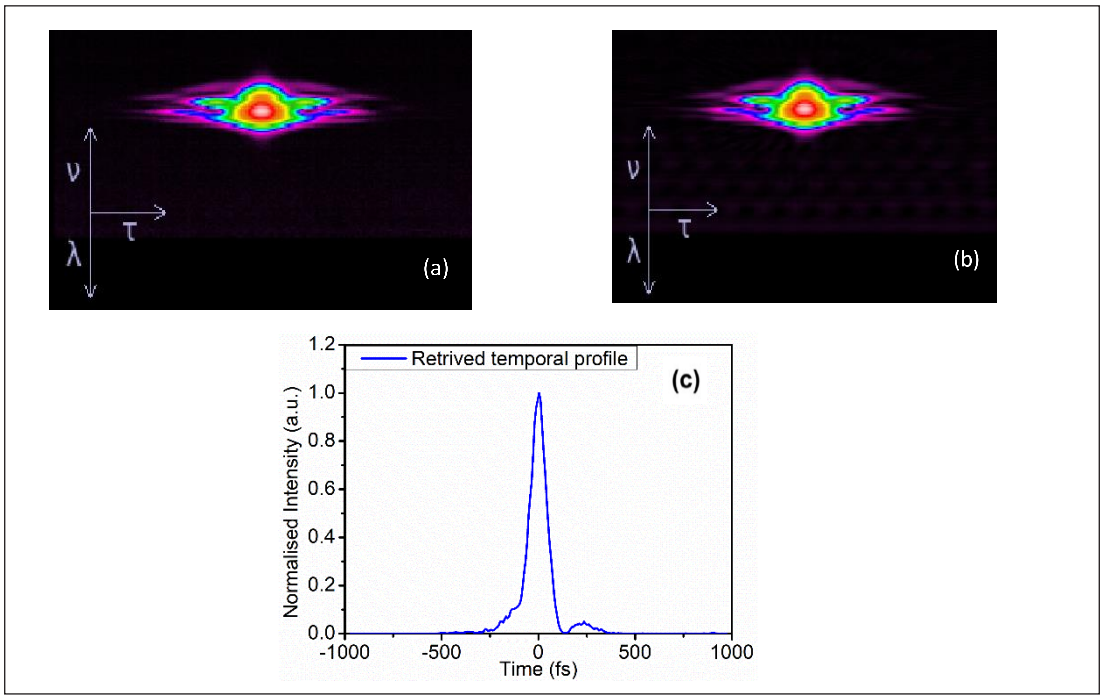

Figure 5: (a) and (b) are the measured and retrieved compressed pulse (c)corresponding retrieved pulse profile from MS-FROG measurements,

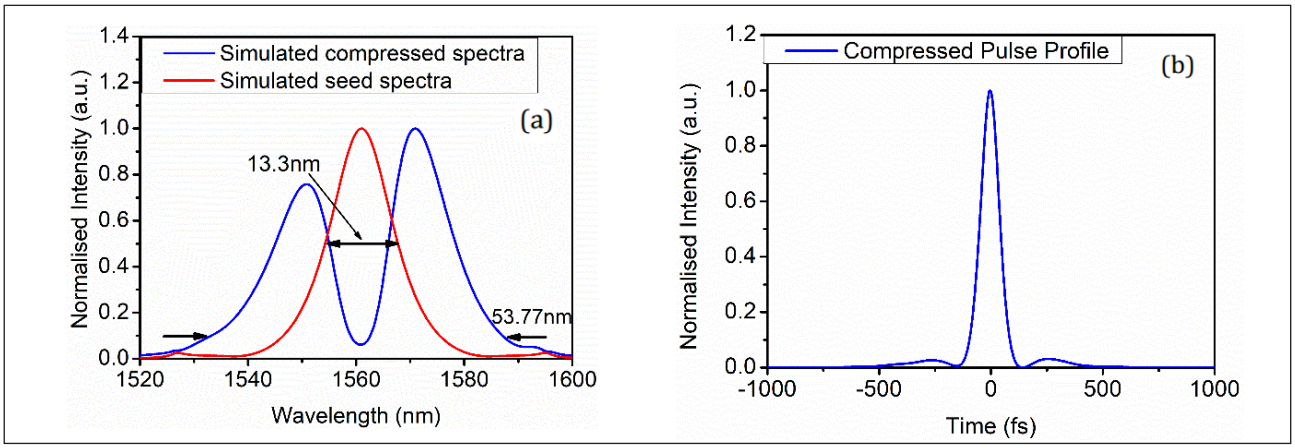

Figure 6: (a) Simulated and experimental compressed output spectra, (b) corresponding simulated pulse profile

showed (Fig.4 (b)) a repetition rate of 88.28 MHz and an SNR exceeding 82 dB, confirming excellent stability. The PBS-based output coupler provided a well-polarized beam with a polarization extinction ratio (PER) of 32.8 dB. After amplification at 60 mW pump power, the output spectrum, showed strong SPM-induced broadening with a 10 dB bandwidth of 53.24 nm and a central dip characteristic of solitonic self-compression. The average output power of 35.3 mW corresponds to 0.39 nJ pulse energy, and MS-FROG measurements revealed 96.5 fs compressed pulses with near-perfect agreement between experimental and reconstructed spectrograms, indicating minimal residual chirp as shown in Fig. 5(a), (b) and (c).

Numerical simulations closely matched these experimental results as shown in Fig. 6 (a) and (b). The simulated seed spectrum had a 3 dB bandwidth of 13.3 nm, consistent with the

measured 13.98 nm. Using an amplifier fiber length of 3.5 m and a compressor fiber of 2.8 m, the model predicted a 10 dB bandwidth of 53.77 nm and compressed pulse duration of 91.6 fs, demonstrating accurate control of dispersion compensation and nonlinear phase evolution. The strong correlation between simulated and experimental results validates the numerical model and confirms the precision in optimizing amplifier and compressor fiber lengths for clean, near-transform-limited femtosecond pulses.

2.3.2 Mode-locked laser operation at 1 μm

At the optimized operating point, continuous-wave lasing was first observed at 75 mW pump power, with stable mode-locking achieved at 88 mW. Pumping the oscillator at 92 mW produced 15 mW average power at a 17.1 MHz repetition rate, corresponding to a pulse energy of 0.88 nJ. The output spectrum exhibited an 11 nm flat-topped rectangular profile characteristic of dispersion-managed dissipative solitons, and the autocorrelation confirmed strongly chirped pulses suitable for compression. In the amplification stages, the preamplifier broadened the spectrum from 11 nm to 16.5 nm through self-phase modulation while preserving the clean spectral shape. The large-mode-area power amplifier delivered ~2 W of average power before compression at the same repetition rate, corresponding to a pulse energy of 117 nJ. After free-space collimation, the Treacy-type diffraction-grating compressor provided near-ideal dispersion compensation, yielding ~350 fs compressed pulses, as shown in the Fig.7, with an average power of ~1.5 W.

2.3.3 Mode-locked laser operation at 2 μmMode-locking in the figure-8 cavity begins at a pump threshold of ~7.1 W, following continuous-wave lasing at 5.5 W, and stable broadband noise-like pulses (NLPs) form at around 9 W. These pulses are centered near 2045 nm with a 3 dB bandwidth of 20.32 nm and exhibit a square temporal envelope of approximately 2.9 ns, confirming NLP dynamics rather than

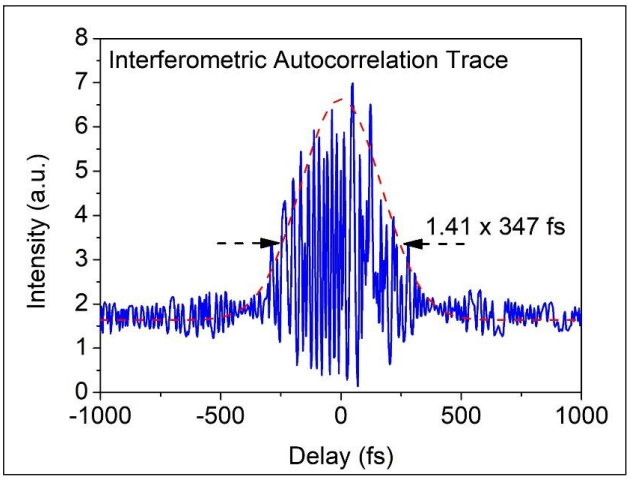

Figure 7: Single pulse auto correlation trace

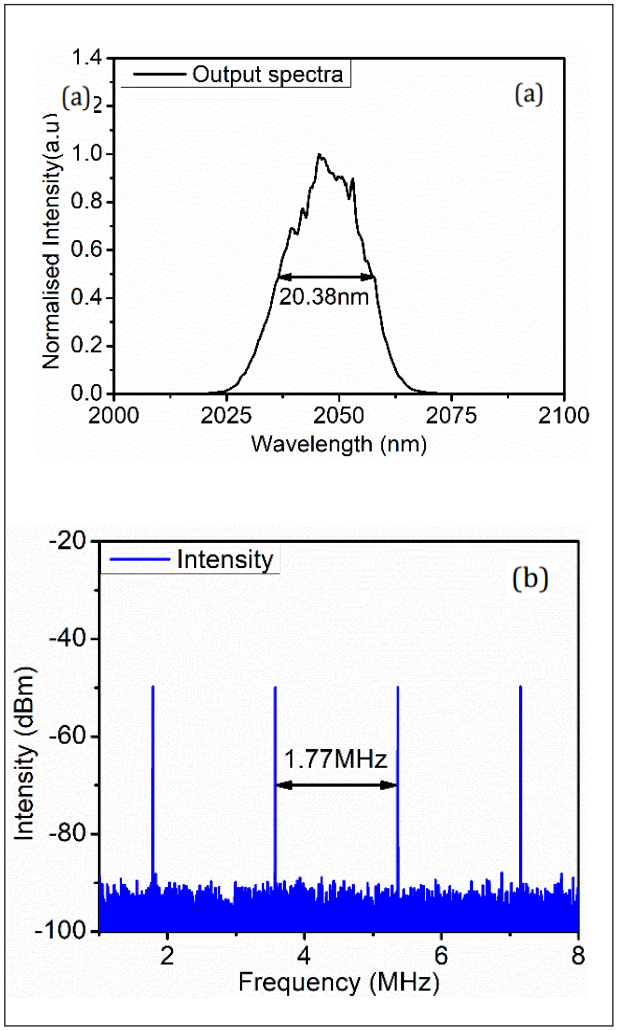

Figure 8: (a) Final spectra (b) Pulse Train

conventional solitonic behaviour. The RF spectrum, as in Fig 8 (a) and (b), shows a clean 1.77 MHz fundamental peak with ~40 dB SNR, consistent with the ~116 m cavity length, and the output power of ~250 mW corresponds to a pulse energy of 141 nJ. These characteristics arise from the strong nonlinear phase accumulation contributed by ~100 m of SMF-28, producing a large net anomalous dispersion of −9.35 ps^2, while the unpumped Ho-doped fiber enhances saturable absorption within the NAbLM. Together, the long-cavity design, high gain, and intensity-dependent interference in the loop mirror enable robust, broadband NLP generation in the 2-μm regime.

3 Effective parameter for real-time elemental analysis

Ultrafast fiber lasers have emerged as transformative tools for real-time elemental analysis, particularly in techniques such as Laser-Induced Breakdown Spectroscopy (LIBS) and Laser Ablation-Inductively Coupled Plasma-Mass Spectrometry (LA-ICP-MS). Key laser parameters including pulse duration, wavelength, pulse energy (or fluence), and repetition rate critically influence laser–material interactions, plasma formation, and subsequent analytical figures of merit. These factors collectively determine the analytical performance, including detection limits, spatial resolution, and elemental fractionation, in real-time elemental analysis.

Wavelength: The laser wavelength significantly influences the energy coupling into the sample, especially across different material types. For ultrafast pulses, this interaction becomes less dependent on the linear absorption coefficient compared to ns-pulsed lasers, owing to the dominance of nonlinear absorption processes [18]. Typically, Yb-doped fiber lasers operating near 1 μm and Er-doped systems around 1.55 μm are commonly used. In certain specialized applications, shorter wavelengths are preferred due to their higher photon energy, which enhances material coupling. To achieve such wavelengths, frequency conversion techniques are often employed.

Pulse duration: The fs-pulses interact with the material on a timescale (<10 ps) that is shorter than the electron-phonon relaxation time, leading to non-thermal ablation often termed "cold ablation" [19]. This minimizes heat diffusion into the surrounding material, resulting in a significantly smaller Heat-Affected Zone (HAZ) and minimal collateral damage [20]. Such non-thermal process drastically reduces elemental fractionation (the non-stoichiometric sampling of elements), a major challenge in ns-pulse bases system, leads to more accurate quantitative analysis. Pulses in the range of 50 fs to 500 fs are generally preferred for maximizing the benefits of cold ablation and high peak power.

Repetition rate: The high repetition rates achievable in fiber laser systems—ranging from tens of kHz to the MHz regime, and even extending to GHz in specialized designs—substantially enhance the sampling rate and the average signal level. This improved signal averaging leads to significantly lower detection limits due to reduced noise and increased measurement precision [21]. Such high repetition rates are particularly advantageous for high-speed elemental mapping and rapid data acquisition, enabling real-time analysis over large sample areas [21]. However, increasing the repetition rate also increases the risk of heat accumulation in the sample, as the time between successive pulses may be insufficient for full thermal relaxation. Therefore, the optimal repetition rate represents a trade-off between maximizing the signal-to-noise ratio (SNR) and minimizing thermal damage. This balance is strongly dependent on the material's thermal properties as well as the pulse energy used.

Pulse energy: Pulse energy and the resulting laser fluence play a central role in determining the ablation yield and the characteristics of the generated plasma. In ultrafast systems, material removal is driven by non-linear absorption processes, enabling efficient ablation even in

transparent or wide-bandgap materials [19]. fs-lasers typically exhibit lower ablation thresholds than ns-pulse systems, allowing material to be removed with reduced energy. For LIBS, an optimal fluence is required—high enough to produce plasma with adequate temperature and electron density for strong and stable emission, but not so high that it leads to excessive self-absorption or thermal effects. Thus, the pulse energy must be carefully balanced: increasing energy improves signal strength, whereas too little energy degrades detection limits. Precise control of low pulse energies (from nJ to µJ levels in fiber-based systems) is essential for achieving high spatial resolution, sub-micrometer-scale sampling, and minimal material removal, which are critical for microanalysis and depth profiling [21].

References

1. R. L. Fork, C. V. Shank, C. Hirlimann, R. Yen, and W. J. Tomlinson, Opt. Lett. 8 (1983), 1-3.
2. D. E. Spence, P. N. Kean, W. Sibbett, Opt. Lett. 16 (1991), 42.
3. K. Tamura, E. P. Ippen, H. A. Haus, and L. E. Nelson, Opt. Lett. 18 (1993), 1080-1082.
4. Pielach, M., Piechal, B., Michalska, M., & Stepanenko, Y. IEEE Access, 8 (2020), 148970–148977.
5. Niu, S.; Wang, W.; Liu, P.; Zhang, Y.; Zhao, X.; Li, J.; Xiao, M.; Wang, Y.; Li, J.; Shao, X. Photonics 11(2024), 857.
6. L. E. Hargrove, R. L. Fork, M. A. Pollack, et al., Appl. Phys. Lett. 5 (1964), 4–5.
7. Sourav Das Chowdhury, Jishnu Dey, et al. *Applied Optics* 64 (2025): F59-F66.
8. L. A. Gomes, L. Orsila, T. Jouhti, et al., IEEE J. Sel. Top. Quantum Electron. 10(2004), 129–136.
9. Y. Cui and X. Liu, Opt. Express 21 (2013), 18969–18974.
10. J. Sotor and G. Sobon, Laser Phys. Lett. 13 (2016), 125102.
11. T. Jiang, K. Yin, C. Wang, et al., Photonics Res. 8 (2020), 78–90.
12. N. J. Doran and D. Wood, Opt. Lett. 13 (1988), 56–58.
13. M. E. Fermann, F. Haberl, M. Hofer, et al., Opt. Lett. 15 (1990), 752–754.
14. J. Szczepanek, T. M. Kardas, M. Michalska, ´ et al., Opt. Lett. 40 (2015), 3500–3503
15. J. Zhao, J. Zhou, Y. Jiang, et al., 38(2020), 6069-6075.
16. Y. Chen, J. Zhao, D. Ouyang, et al., IEEE Photonics Journal, 13(2021), 1-5.
17. Bhaswar Dutta Gupta, Sourav Das Chowdhury, Devnath Dhirhe, and Mrinmay Pal, J. Opt. Soc. Am. B 37 (2020), 2278-2286.
18. Eugene G. Gamaly, "Femtosecond Laser-Matter Interaction -Theory, Experiments and Applications" Jenny Stanford Publishing, New York (2011).
19. Hergenröder R, Samek O, Hommes V. Mass Spectrom Rev. 25(2006), 551-72.
20. R. K. Singh and J. Narayan, Phys. Rev. B, 41 (1990), 8843.
21. Vassilia Zorba, Xianglei Mao, Richard E. Russo, Spectrochimica Acta Part B: Atomic Spectroscopy, 66 (2011), 189-192.

Jishnu Dey *Completed B.Sc. Physics from Asutosh College under University of Calcutta, Masters' degree in Physics from NIT, Jamshedpur. Currently working as a Junior Research Fellow at CSIR-CGCRI focussed on ultrafast fiber lasers and amplifiers, nonlinear optics and related numerical simulations.*

Shubhranil Maity *Completed B.Sc. in Physics from Midnapore College (Autonomous) under Vidyasagar University, followed by an M.Sc. in Physics from the Ramakrishna Mission Vivekananda Educational and Research Institute. He pursued his doctoral research at CSIR-CGCRI, focusing on advanced fiber lasers and optical amplifiers. He currently serves as an Assistant Manager in R&D, developing high-power fiber laser systems for additive manufacturing and other industrial applications.*

	***Dr. Uttam Kumar Samanta*** *He completed his Master's degree in Physics from the Indian Institute of Engineering Science and Technology in 2018 and earned his PhD in Science from Jadavpur University in 2024. He is currently a postdoctoral researcher at Tampere University, Finland. His research focuses on ultrafast and narrow-linewidth fiber lasers and amplifiers, advanced structured optical fibers, and the generation and amplification of structured light in fiber-based platforms.*
	***Abdul Malek Mallik*** *He holds a Diploma in Civil Engineering from the West Bengal State Council of Technical Education. He currently works as a Project Assistant, supporting research works on ultrafast and high-power fiber laser systems.*
	***Dr. Sourav Das Chowdhury,*** *M. Tech in Laser Technology from IIT Kanpur and Ph.D. Engineering from Jadavpur University, is currently Senior Scientist in Fiber Optics and Photonics Division at CSIR-Central Glass and Ceramic Research Institute, Kolkata. Priory, he was working as Manager (R&D) in Fiber Laser Development Team at Taihan Fiber Optics in Korea. His R&D activities cover both numerical simulations & experimentation on fiber lasers, nonlinear fiber optics and ultrafast optics. He has co-authored 22 SCI journals, 2 patents, won SPIE and IEEE best paper awards. He is a member of OPTICA, founding president of CSIR-CGCRI OPTICA Student Chapter and reviewer of various OPTICA, IEEE and Springer journals*
	***Dr. Debasis Pal*** *He earned his M.Sc. in Physics from the National Institute of Technology Durgapur in 2013 and completed his Ph.D. at Jadavpur University in 2020. He is currently a Scientist in the Fiber Optics and Photonics Division at CSIR–Central Glass and Ceramic Research Institute, Kolkata. His research focuses on narrow-linewidth fiber lasers and amplifiers, as well as pulsed fiber lasers for scientific, industrial, and medical applications. He is a member of Optica, the Indian Laser Association (ILA), and the Indian Ceramic Society (ICS).*
	*Dr. Atasi Pal is a Senior Principal Scientist in the Fiber Optics & Photonics Division of CSIR-CGCRI and supervises projects on design/characterization of fiber lasers in her laboratory. She received her Ph.D. in Measurement and Instrumentation from School of Engineering and Mathematical Science, City University London, UK in 2013. Following her Bachelor degree in Electronics & Telecommunication Engineering from Jadavpur University, Kolkata, India in 2003, she joined CSIR-CGCRI to participate in design, fabrication and characterization of specialty optical fiber for laser amplifiers and sensors. With over two decades of research experience, she has led multiple national and industry-sponsored projects in high-power fiber laser systems, ultrashort pulse sources, and thulium fiber laser technology translation. Her portfolio includes 1 granted patent, 2 patent applications, 3 ToTs, more than 35 SCI journal publications, and 40 conference presentations.*

Molecular Structural Correlation with Singlet Fission Dynamics and Yield: Case Studies on Anthracene Based Singlet Fission Materials

B. Manna,* A. Nandi and R. Ghosh*
Radiation & Photochemistry Division, Bhabha Atomic Research Centre, Mumbai-400085
Email: bmanna@barc.gov.in

Abstract:

Singlet fission (SF) is a multiexciton generation process observed in organic semiconductors, where a photoexcited singlet exciton generates two long-lived triplet excitons. In this article, we present SF dynamics of various anthracene-based materials employing time-resolved emission and absorption spectroscopic techniques. These materials exhibit high triplet energies (>1.2 eV), making them promising candidates for enhancing the efficiency of silicon-based solar cells. The impact of molecular structure on SF yield—both favourable and detrimental effects—has been systematically examined. Additionally, the potential role of triplet-triplet recombination and the formation of excimer state in iso-energetic SF systems is experimentally explored. The influence of particle or grain size variation is also considered, and based on these findings, we discuss the structural requirements for optimizing SF in anthracene-based materials.

Introduction

The solar cell industry predominantly relies on silicon-based photoabsorbing materials due to their natural abundance, broad solar absorption range, and excellent ambient stability. Silicon has a band gap of approximately 1.1 eV. However, as the solar spectrum extends from about 4 eV to below 1 eV, silicon-based cells face two significant energy losses during solar-to-electric conversion.Photons with energies below 1.1 eV are not absorbed, while those with higher energies lose their excess energy through thermalization to 1.1 eV before charge extraction (Figure 1). As a result, the single junction solar cell reported to convert maximum 33% of solar energy into electricity, also well-known as Shockley−Queisser (SQ) limit.[1]To mitigate this thermalization loss, in inorganic nanomaterials researchers have explored various strategies, including the introduction of multijunction solar cells with different band gaps, hot-carrier extraction, and multiexciton generation.

In organic semiconductors, singlet fission (SF) is one promising approach, wherein a single photoexcited singlet exciton splits into two long-lived triplet excitons (Equation 1).[2] Thus

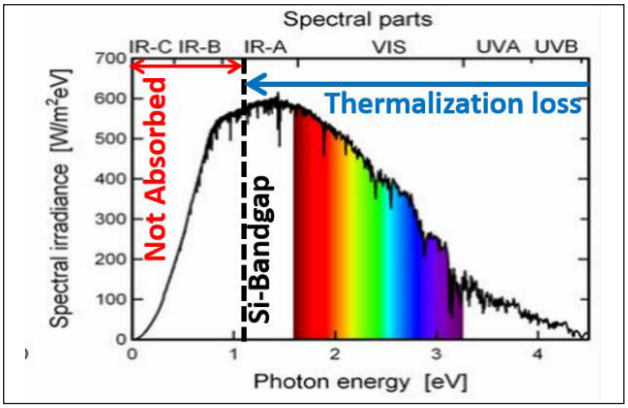

Figure 1: *Schematic showing the solar spectrum, silicon bandgap, and loss due to thermalization and not absorption loss.*

have been extensively investigated by different research groups for exploration of new efficient SF systems or to obtain mechanistic insights for better effeciency.[2-10]

$$S_1(\uparrow\downarrow) + S_0(\uparrow\downarrow) = T_1(\uparrow\uparrow) + T_1(\downarrow\downarrow) \qquad (1)$$

If these triplets have energies greater than 1.1 eV, they could potentially transfer energy to silicon, thereby improving solar cell efficiency. This concept has been demonstrated using tetracene as the SF material, coupled with silicon by Einzinger et. al.[11] While SF is endothermic

in anthracene itself, the introduction of ethynyl substitutions at the 9,10-positions of anthracene has been shown to alter the energetics and enable SF.[12-15] Anthracene-based SF materials typically exhibit triplet energies around 1.2–1.3 eV, making them promising candidates for energy transfer to silicon. Moreover, some anthracene derivatives are commercially available, cost-effective, and offer better solubility and ambient stability compared to tetracene.

Therefore, in this study, we investigate two anthracene-based systems (Scheme 1) and analyse the influence of molecular structure and particle size on SF dynamics and yield.

Experimental Section

9,10-bis[phenylethynyl]anthracene (BPEA) and 9,10-bis[(trisopropylsilyl)ethynyl]anthracene derivatives (TIPS-An) were purchased from Mark and used as received. Nanoaggregates (NAs) and thin films were prepared via reprecipitation and physical vapor deposition (PVD), respectively. Morphological characterization was performed using dynamic light scattering (DLS) [Malvern 4800 Autosizer with a 7132 digital correlator], atomic force microscopy (AFM) [NT-MDT, Solver Model], and X-ray diffraction (XRD) [Agilent Super Nova X-ray diffractometer]. Steady-state absorption and emission spectra were recorded at room temperature using a V-670

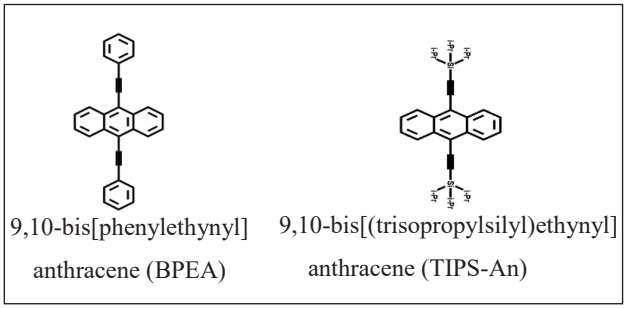

Scheme 1: *Structure of the BPEA and TIPS-An molecules*

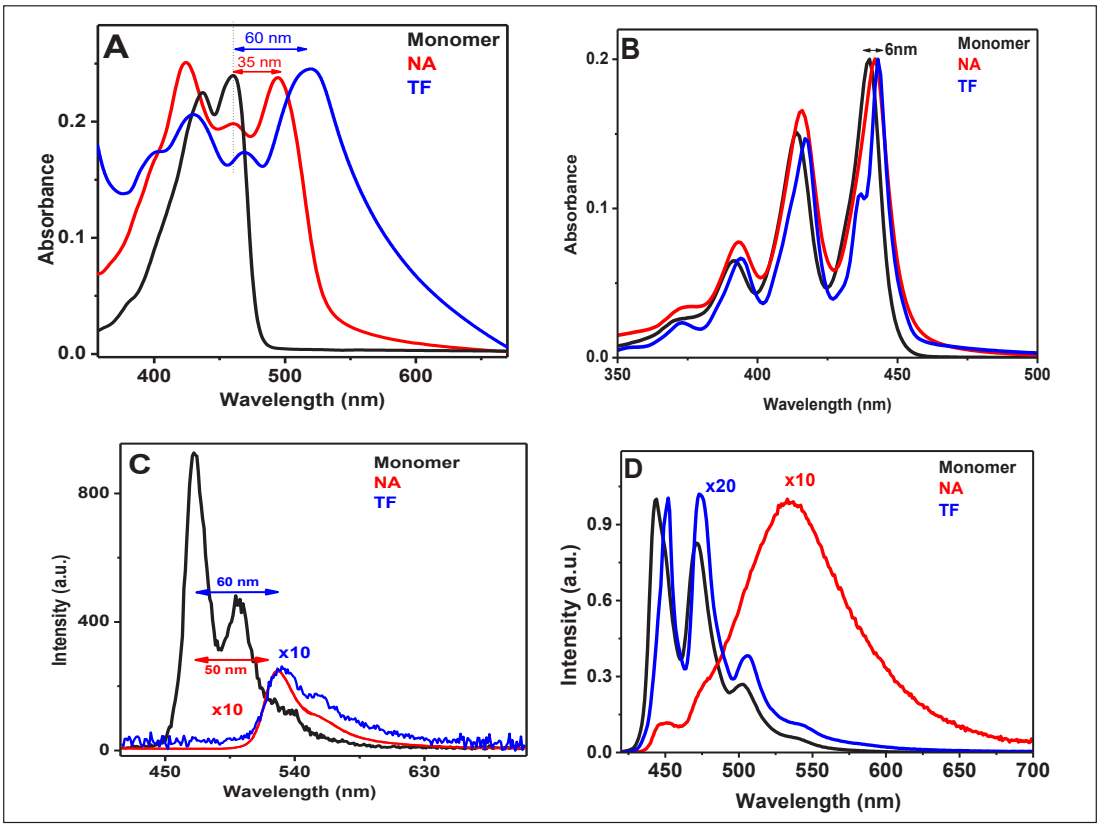

Figure 2: *The steady state UV-Visible absorption (A:BPEA),(B:TIPS-An) Room temperature photoluminescence spectra(C:BPEA), (D:TIPS-An) for BPEA and TIPS-An in their monomeric, NA and TF forms. These figures are reproduced from Ref 12 and 13.*

spectrophotometer (JASCO) and a Fluorolog-3 spectrofluorometer (Horiba JobinYvon), respectively. Time-resolved emission studies were carried out using a time-correlated single photon counting (TCSPC) setup (IBH, U.K.) in the sub-nanosecond to nanosecond time domain, while ultrafast measurements were performed using up-conversion techniques [FOG-100, CDP Corporation, Russia]. Singlet fission and triplet dynamics were monitored with ultrafast transient absorption (UTA) [ExciPRO, CDP Corporation, Russia] and nanosecond-resolved flash photolysis (FP) techniques [Edinburgh Instruments, UK, model LP920]. To investigate triplet-triplet annihilation (TTA)-mediated excimer formation, nanoaggregate samples were doped with zinc-octaethylporphyrin (ZnOEP).

Results & Discussions

Morphological analysis via DLS (for NAs) and AFM confirmed the formation of nanoaggregates with sizes ranging from 200–400 nm and thin films with a thickness of 100 ± 10 nm. XRD patterns revealed peaks associated with monoclinic molecular packing. However, TIPS-An NAs exhibited broad scattering backgrounds, indicating a significant contribution of random molecular packing, while thin films displayed less scattering, suggesting better packing.

Steady-state absorption spectra revealed a significant redshift (35–60 nm) for BPEA nanoaggregates and thin films compared to its monomeric form (Figure 2A), indicating stabilization of the singlet band due to strong intermolecular interactions.[12,13] In contrast, TIPS-An exhibited a smaller shift (5–6 nm, Figure 2B), suggesting less favourable molecular packing, likely due to the bulky iso-propyl groups attached to each Si atom.[14]

The steady-state emission intensity decreased by nearly 50 times for BPEA in its nanoaggregate and thin film forms (Figure 2C, Table 1).[12] For TIPS-An, a 10–20 times reduction in emission yield was observed from monomeric to aggregate or thin film form(Figure 2D, Table 1).[13] This low emission yield is characteristic of efficient SF materials, where SF is a nonradiative process that outcompetes the radiative decay channel. Thus, this behaviour is considered advantageous for these materials. Additionally, TIPS-An nanoaggregates displayed a broad, structureless redshifted emission band, indicative of excimer formation, alongside a weaker excitonic emission.

TCSPC measurements revealed a significant reduction in the singlet exciton lifetime for both systems in their nanoaggregate and thin film

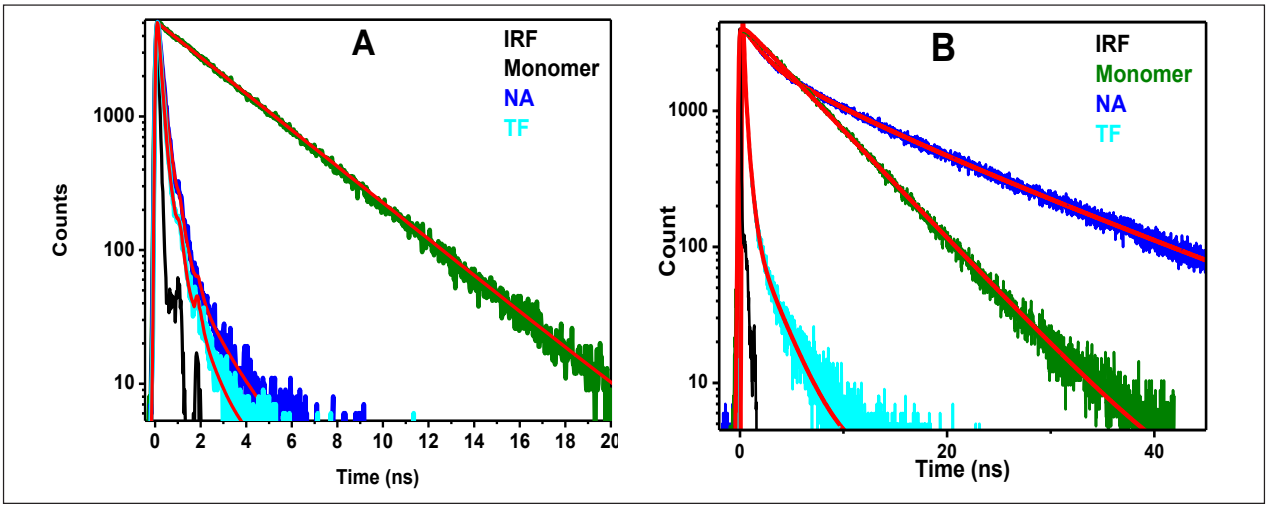

Figure 3: *Photoluminescence decay kinetics recorded after excitation with 405 nm light for BPEA (A) and TIPS-An (B) in monomeric, NA and TF forms at the emission maximum of the corresponding samples. These figures are reproduced from Ref 12 and 13.*

forms. Although the kinetics are wavelength-dependent and multiexponential, the major component was faster than the instrument response function (IRF) (Figure 3, Table 1). In particular, TIPS-An exhibited an emission maximum redshifted by approximately 0.7 eV, with a major decay component of 15 ns, which is nearly three times longer than its monomeric lifetime, suggesting the involvement of an excimer state.

Table 1: *Photophysical parameters of BPEA and TIPS-An in THF solution, NA and TF. The data are reproduced from Ref 12 and 13.*

Molecular System	Sample form	Φ_{fl}	τ
BPEA	Monomer	1	3.18 ns
	NA	0.018	20 ps
	TF	0.020	22 ps
TIPS-An	Monomer	0.71	5.43ns
	NA	0.07	~ 15 ns[a]
	TF	0.03	< 0.2ns[a]

[a]*Lifetime of major decay component probed at emission maximum*

The shortest lifetime component, unresolved by TCSPC, was examined with femtosecond up-conversion experiments. The singlet lifetimes for BPEA nanoaggregates and thin films were found to be 20 and 18 ps, respectively, while TIPS-An showed singlet lifetimes of 2.5 and 1 ps in its nanoaggregate and thin film forms.

UTA measurements on BPEA nanoaggregates and thin films revealed that, immediately after photoexcitation, the spectra exhibited excited state absorption (ESA) and ground state bleach (GSB) signals associated with to S_0- S_1 population redistribution (Figure 4A). These signals rapidly decayed or recovered on a timescale of 5–10 ps, with a time constant of approximately 1 ps, corresponding to singlet-singlet annihilation. At high exciton densities, two S_1 excitons interact, producing one S_n exciton and one ground state molecule. After this initial process, the decay of the S_1 ESA, concomitant GSB enhancement, and T_1 ESA growth were observed with an 18–20 ps lifetime (Figure 4B, Table 2). This GSB enhancement, coupled with triplet growth, is a hallmark of SF, where one ground state molecule is promoted to a triplet state.

Triplet yield was further estimated from nanoaggregate and thin film samples, yielding 139% and 157%, respectively, indicating that SF is indeed occurring Triplet yield exceeding 100% is itself a proof for involvement of SF process.[12]

Table 2: *Fitting Parameters of the temporal profiles recorded at different wavelengths for BPEA NA. The table is reproduced from Ref 12.*

Wave-length (nm)	τ_1 (a_1)	τ_2 (a_2)	τ_3 (a_3)
475	------	20 ps (24)	Long (>300 ps) (-17.5)
508	1.2 ps (66)	24 ps (-56)	Long (>300 ps) (24.5)
650	0.9 ps (-54.5)	25 ps (-12.5)	-----

In TIPS-An nanoaggregates and thin films, excitation fluences were kept lower to minimize singlet exciton annihilation. The spectral features were similar to those of BPEA, but advanced global fitting analysis resolved three major contributors to the spectral dynamics (Figure 5). The presence of silicon atoms facilitated the formation of a fast charge transfer (CT) state, which then underwent SF with time constants of 44 ps and 10 ps in nanoaggregates and thin films, respectively.[13] SF rates were notably faster in TIPS-An thin films compared to BPEA, likely due to the higher S_1 energy levels, which favour faster SF processes.

However, laser flash photolysis (LFP) studies showed weaker triplet ESA signatures in TIPS-An nanoaggregates, with triplet yields less than 40%. In contrast, triplet ESA was more prominent in TIPS-An thin films, although it was weaker than in BPEA thin films, with an estimated triplet yield of ~78% (Figure 6).

The presence of bulky iso-propyl groups in TIPS-An leads to poor molecular packing, which, in turn, facilitates the formation of alternative decay channels, such as excimer formation. These

factors are the primary limitations for achieving an effective triplet yield in TIPS-An. Interestingly, despite these challenges, TIPS-An exhibits a

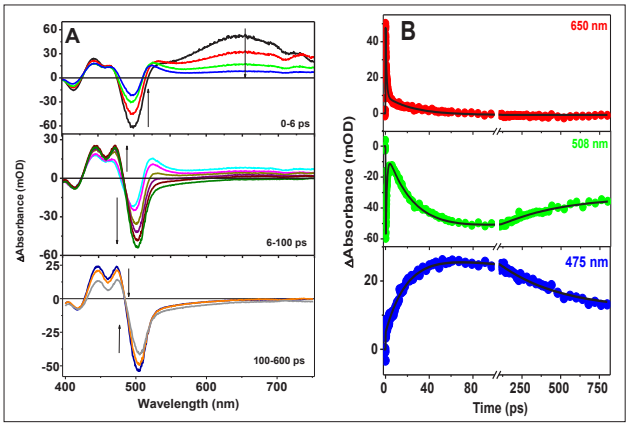

Figure 4:*(A) Transient absorption spectra recorded at different delay times for BPEA NA after excitation with 390 nm light,(B) temporal profiles along with fitted data recorded at 650 nm (ESA S_1), 508 nm (GSB) and 475 nm (ESA T_1), respectively. The figure is reproduced from Ref 12.*

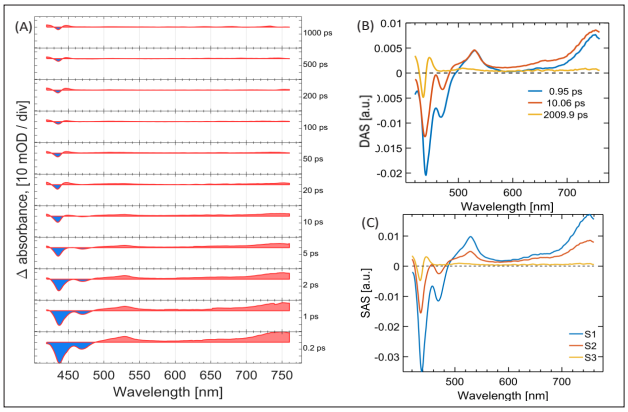

Figure 5: *(A) Transient spectral evolution of TIPSAn TF prepared by thermal vapour deposition on transparent glass substrate. Sample was excited with a 400 nm femtosecond laser having 100 nJ/pulse energy. (B) Decay associated spectra (DAS) obtained from global fitting of the TA data with three transient species. (C) Corresponding species associated spectra (SAS) obtained from global analysis. The figure is reproduced from Ref. no. 13.*

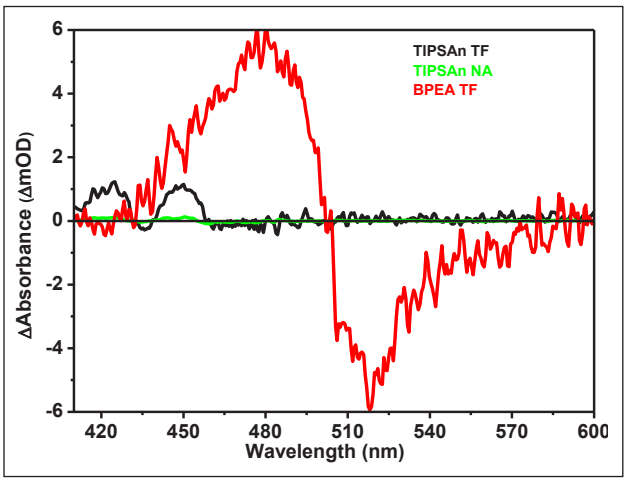

Figure 6: *Transient absorption spectra of TIPSAn NA and TF recorded 10ns time delay under identical experimental condition. OD normalized 10ns LFP spectra of BPEA TF is also incorporate in figure for comparison. The figure is reproduced from Ref. no. 13.*

sufficiently fast singlet fission (SF) rate that could potentially surpass the other decay processes. To further explore this, we investigated the role of triplet-triplet annihilation (TTA) in back-conversion from triplets to singlets, particularly its impact on excimer formation in such iso-energetic SF systems.

To elucidate the role of TTA-mediated back conversion and excimer formation, TTA upconversion experiments (Figure 7) were performed on zinc-octaethylporphyrin (ZnOEP)-doped TIPS-An nanoaggregates.[16] The sample was excited with 532 nm laser light, and the emission spectra were compared with those recorded during photoluminescence (PL) studies, where the same sample was excited at 380 nm (Figure 8). For a comparable excimer signature, the PL results showed much weaker contributions from the excitonic emission, suggesting that during TTA, two triplet

Table 3: Parameter related to SF process of different particles.

Nanoaggregate	Particle Size (nm)	Triplet yield	SF time constant (ps)	^{1}[TT] recombination time (ps) (% Amplitude)
NA1	40-150	21%	26±3	80±4 (88%)
NA2	100-500	68%	35±5	100±5 (36%)
NA3	400-1500	176%	49±5	300±11 (13%)

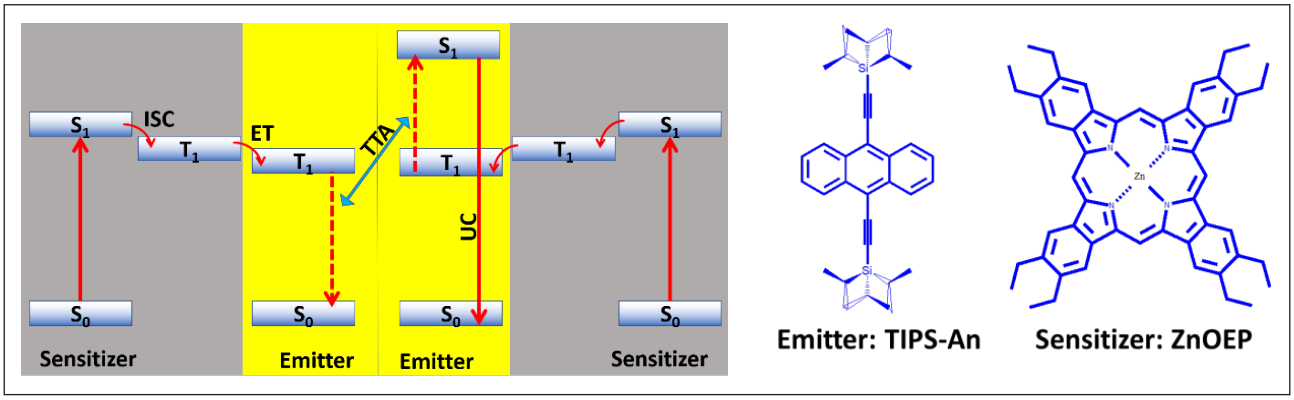

Figure 7: *Schematic of steps associated with TTA-UC and molecular structures for TIPS-An and ZnOEP used for TTA-UC.*

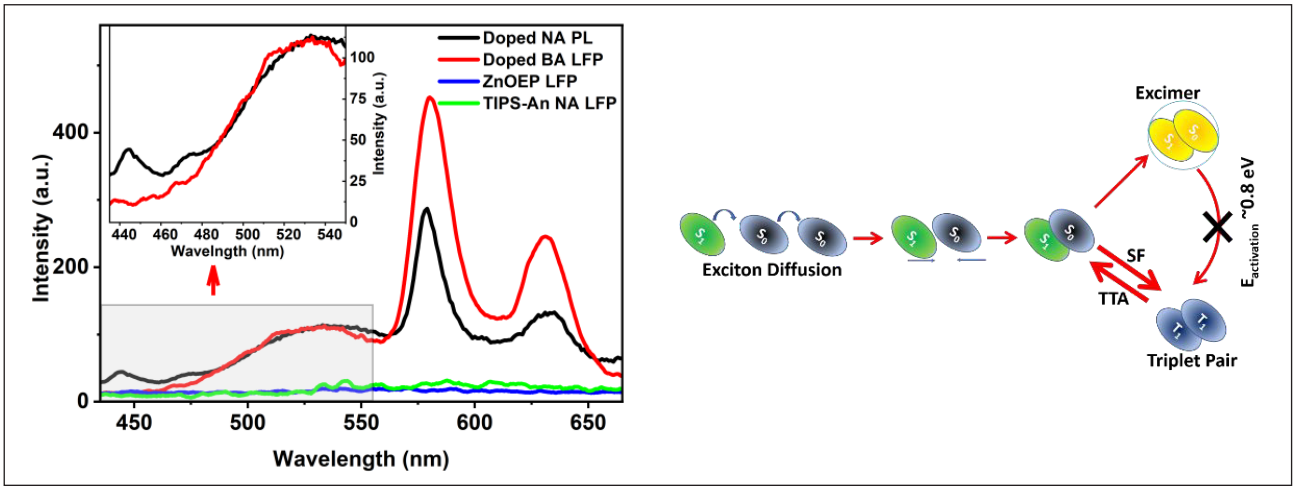

Figure 8: *TTA-UC mediated emission recorded after exciting the ZnOEP doped TIPS-An NA sample with 532 nm laser light. Inset: enlarged emission spectra for the TIPS-An upconverted emission part. Schematic: showing the comparative mechanism of TT pair and excimer formation and its reverse process. The figure is reproduced from Ref. no. 16.*

molecules approach each other closely enough to facilitate S_1-S_0 pair formation (Figure 8, scheme). This pair formation serves as an intermediate step in excimer formation, favouring excimer production over the normal photogenerated route. Once the back-converted excimer forms, it is stabilized by approximately 0.8 eV, effectively eliminating the possibility of triplet formation for the SF process. Since TIPS-An is an iso-energetic SF system, the back transfer and the associated excimer formation significantly hinder effective triplet yield.

Our findings indicate that the planar BPEA derivative exhibits superior molecular packing and a higher SF yield compared to TIPS-An. Notably, SF is also nearly iso-energetic in BPEA, highlighting the importance of defect management and molecular packing. It has been observed that as particle size increases, better molecular packing is achieved. To explore this further, we synthesized nanoparticles of various sizes through a centrifugation-mediated separation process and confirmed our hypothesis with basic steady-state absorption studies. These nanoaggregates were labelled as NA1, NA2, and NA3, with their corresponding size ranges and SF parameters summarized in Table 3. The size-dependent SF dynamics were further investigated using ultrafast transient absorption (UTA) and laser flash photolysis (LFP) studies (Figure 9).

The transient absorption dynamics of BPEA nanoaggregates were discussed earlier. Here, we

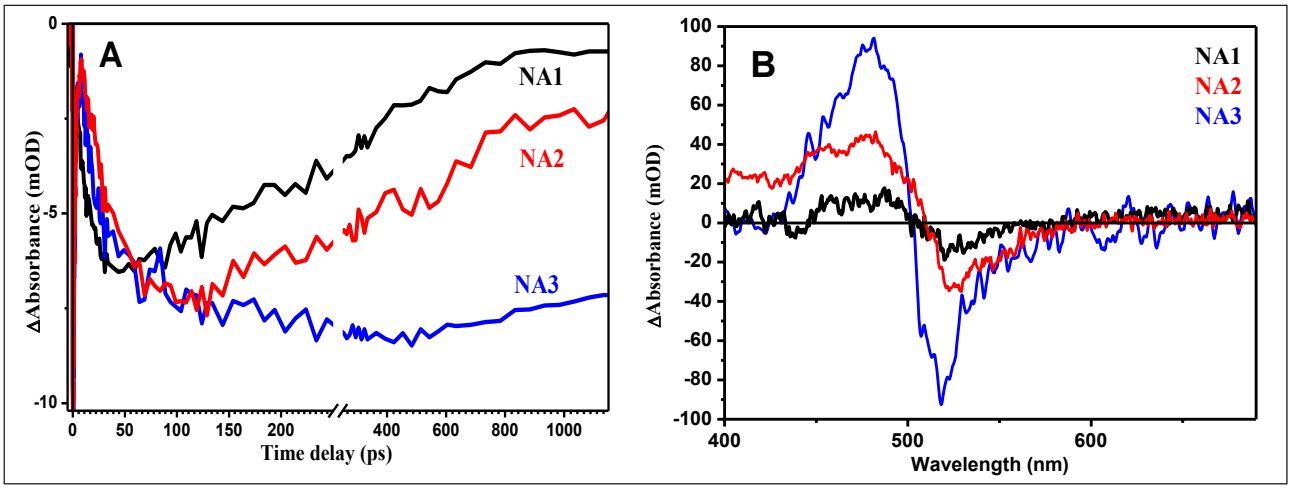

Figure 9: *(A) Ground state bleach dynamics of three different NA samples of BPEA at 510nm (B) OD corrected nanosecond flash photolysis spectra recorded at 10ns delay after photoexcitation. The figure is reproduced from Ref 17.*

observe that faster SF dynamics are evident for NA1, with slower dynamics as the particle size increases. Moreover, the triplet ESA and ground-state bleach (GSB) signals exhibited faster decay or recovery in the nanosecond time domain for NA1, and as the particle size increases, these features slowdown, which suggests more available triplets for energy extraction (Figure 9A). The fast decay is attributed to triplet-triplet recombination in these smaller particles.

The absorption band shift for particles of different sizes was found to be size-dependent. Specifically, as the particle size increases, the absorption band undergoes a more pronounced redshift, indicating better stabilization of the S_1 energy level due to enhanced intermolecular interactions associated with improved molecular packing. In smaller particles, a higher S_1 energy level promotes faster triplet pair exciton production via the SF mechanism. However, improper packing results in inefficient triplet separation, leading to significant recombination losses within the picosecond timescale. Additionally, the formation of lower-energy excimer states also contributes to reduced effective triplet yield. As a result, only 21% of triplets survive after 1 ns. In larger particles, the larger grain size and better molecular packing facilitate efficient triplet separation, resulting in a high yield of long-lived free triplet excitons (~176% after 1 ns). These systematic studies highlight the influence of particle size on the SF dynamics of BPEA. Since higher free triplet exciton yield and longer triplet lifetime are essential for efficient energy extraction, we propose that larger, well-ordered crystallite particles are ideal for organic solar cell (OSC) applications.

Conclusions

In this study, we investigated two anthracene-based systems, focusing on the molecular structure and the role of packing in SF dynamics. Our results demonstrate that planar BPEA molecules enable better molecular packing, which reduces losses due to defect trapping and excimer formation. Larger particle sizes lead to a significant redshift in the steady-state absorption band, indicative of near-crystal packing, which facilitates longer lifetimes of SF-mediated triplets. In contrast, the bulky iso-propyl groups in TIPS-An hinder molecular packing, resulting in increased defect-mediated losses and less efficient triplet yield. Importantly, TTA upconversion studies revealed that excimer formation is favoured during the TTA process, while back conversion from the excimer state leads to the formation of S_1-S_0 pairs. This back-transfer process reduces the possibility of triplet formation for SF, thus lowering the effective triplet yield. Therefore, it can be concluded that planar molecules with optimal packing are better

suited for enhancing triplet yield and overall SF efficiency. Substituents should be carefully chosen to avoid disrupting packing, while also tuning the energetics and SF dynamics to maximize triplet yield and improve photovoltaic performance.

References:

1. W. Shockley and H. J. Queisser, J. Appl. Phys.32 (1961) 510.
2. M. B. Smith and J. Michl, J. Chem. Rev. 110 (2010) 6891.
3. M. B. Smith and J. Michl, Annu. Rev. Phys. Chem., 64 (2013) 361.
4. M. Miyata, F. S. Conrad-Burton, F. L. Geyer and X. Y. Zhu, Chem. Rev. 119 (2019) 4261.
5. A. Rao and R. H. Friend, Nat. Rev. Mater. 2 (2017) 17063.
6. C. A. Nelson, N. R. Monahan and X.-Y. Zhu, Energy Environ. Sci. 6 (2013) 3508.
7. M. J. Y. Tayebjee, D. R. McCamey and T. W. Schmidt, J. Phys. Chem. Lett. 6 (2015) 2367.
8. N. J. Thompson, D. N. Congreve, D. Goldberg, V. M. Menon and M. A. Baldo, Appl. Phys. Lett. 103 (2013) 263302.
9. M. K. Gish, N. A. Pace, G. Rumbles and J. C. Johnson, J. Phys. Chem. C. 123 (2019) 3923.
10. R. Casillas, I. Papadopoulos, T. Ullrich, D. Thiel, A. Kunzmanna and D. M. Guldi, Energy Environ. Sci., 13 (2020) 2741.
11. M. Einzinger, T. Wu, J. F. Kompalla, H. L. Smith, C. F. Perkinson, L. Nienhaus, S. Wieghold, D. N. Congreve, A. Kahn, M. G. Bawendi and M. A. Baldo, Nature, 571 (2019) 90.
12. B. Manna, A. Nandi and R. Ghosh, J. Phys. Chem. C 122 (2018) 21047.
13. A. Nandi, B. Manna and R. Ghosh, J. Phys. Chem. C 127 (2023) 12621.
14. Y. J. Bae, G. Kang, C. D. Malliakas, J. N. Nelson, J. Zhou, R. M. Young, Y. L. Wu, R. P. V. Duyne, G. C. Schatz and M. R. Wasielewski, J. Am. Chem. Soc. 140 (2018) 15140.
15. K. Bhattacharyya and A. Datta, J. Phys. Chem. C 121 (2017) 1412.
16. B. Manna, J. Phys. Chem. C 129 (2024) 9809.
17. A. Nandi, B. Manna and R. Ghosh, J. Photochem. Photobiol. A: Chem, (2025) (Just Accepted)

Dr. Biswajit Manna did his B.Sc. in Chemistry from the University of Calcutta and M.Sc. from Indian Institute of Technology, Bombay. Subsequently he joined Bhabha Atomic Research Centre in 2011. He obtained Ph. D. in 2018 from Homi Bhabha National Institute, Mumbai. Dr. Manna went to University of South Carolina for his postdoctoral research work in 2022 and worked in multidimensional rate spectroscopy. He was conferred with young scientist award by the National Academy of Sciences, India in 2022. Presently he is continuing his work in the field of photochemistry and ultrafast spectroscopy. His main research interests are exciton dynamics of organic nanostructure materials. Apart from this, he is also presently engaged in the development of optical pump terahertz probe spectrometer.

Dr. Amitabha Nandi completed his B.Sc. in Physics from the University of Calcutta and M.Sc. from IIT Kanpur. He joined RPCD at the Bhabha Atomic Research Centre in 2013 and earned his Ph.D. in 2022 from Homi Bhabha National Institute, Mumbai. His research focuses on photochemistry, ultrafast spectroscopy, and femtolysis, with an emphasis on morphology-dependent excited state dynamics of organic materials. His work is particularly aimed at advancing photovoltaics, improving efficiency, and enhancing solar energy technologies.

Dr. Rajib Ghosh is a scientific officer at Bhabha Atomic Research Centre, Mumbai, India. After completing M. Sc. in chemistry from University of Burdwan, he joined Bhabha Atomic Research Centre in 2007. He received his Ph. D. degree in 2015 from Homi Bhabha National Institute, Mumbai, for his work on ultrafast structural dynamics in charge transfer molecules in solution. Dr. Ghosh pursued postdoctoral research on ultrafast coherent spectroscopy in Max-Planck Institute for Structure and Dynamics of Matter, Hamburg, Germany. Dr. Ghosh is recipient of University Gold Medal and Homi Bhabha Gold Medal and conferred with young scientist award by the Department of Atomic Energy in 2015and by the National Academy of Sciences, India in 2018. His current research interest includes ultrafast spectroscopy, exciton dynamics and coherent spectroscopy of organic and inorganic materials of optoelectronic interest.

A short review on current strategies for development of emitters for efficient OLED

Komal Vasant Barhate and Neeraj Agarwal*

School of Chemical Sciences, UM DAE Center for Excellence in Basic Sciences, University of Mumbai, Kalina, Santacruz (E), Mumbai 400098, India.

E-mail: na@cbs.ac.in

Abstract

OLED technology has evolved during past few years by using fluorescent, phosphorescent, advanced thermally activated delayed fluorescence (TADF) and hybrid systems focusing on improvising the efficiency, stability, and colour purity. Challenges such as efficiency roll-off, broad emission spectra, and limited device stability continue to hinder commercial applications requiring high colour purity, particularly in emerging display technologies. This review highlights recent advances in multi-resonance TADF, emerging concepts such as CPL and radical-based doublet emission driving the development of next-generation high-performance and long-lifetime OLEDs.

Introduction

Organic light-emitting diodes (OLEDs) have substantially advanced modern display and lighting technologies owing to their remarkable capabilities such as flexibility, low power consumption, lightweight, and fast response times. The emitter materials play a pivotal role in determining OLED device performance and have evolved significantly over the years, forming distinct generations based on their emission mechanisms and efficiency improvements.

The first report on an OLED was presented by Tang and VanSlyke in 1987, who demonstrated electroluminescence from 8-hydroxyquinoline aluminium (Alq_3) with an external quantum efficiency (EQE) of 1% and brightness exceeding 1000 $cd.m^{-2}$.[1] This pioneering work sparked tremendous research interest in OLED technology. Fluorescent materials exhibited excellent colour purity and fast emission lifetimes, but their EQEs were limited to ≤ 5% (maximum internal quantum efficiency, $IQE_{max} \approx 25\%$) due to spin statistics restricting emission to only singlet excitons, while triplet excitons remained non-radiative.[2,3] The arrival of second-generation phosphorescent emitters based on Ir(III) and Pt(II) complexes revolutionized OLED efficiency by utilizing strong spin–orbit coupling (SOC) to enable harvesting of both singlet and triplet excitons, achieving IQE_{max} approaching 100% and EQEs exceeding 20%.[4,5] However, these systems faced challenges such as high material cost, limited operational stability especially for blue emitters and complex synthesis routes. Alternatively, triplet harvesting can be achieved by exploiting a small ΔE_{ST} for reverse intersystem crossing, transforming triplet excitons to singlet excitons and leading to third-generation thermally activated delayed fluorescence (TADF) emitters.[6] This has been attributed to a small ΔE_{ST} value, which is represented[7,8] by

$$E_s = E + K + J \quad (1)$$

$$E_T = E + K - J \quad (2)$$

$$\Delta E_{ST} = (E + K + J) - (E + K - J) = 2J \quad (3)$$

where E_S and E_T are the lowest singlet and triplet excited energy. E is the orbital energy, K is the electron-repulsion energy, and J is the electron exchange energy. Thus, from equation 3, J is the key parameter for decreasing ΔE_{ST}, and it can be

expressed by

$$J = \iint \phi_{HOMO}(r_1)\phi_{LUMO}(r_2)\frac{1}{|r_2-r_1|}\phi_{HOMO}(r_2)\phi_{LUMO}(r_1)dr_1dr_2 \quad 4$$

where ϕ_{HOMO} and ϕ_{LUMO} are the spatial distributions and r_1 and r_2 are the position vectors of the HOMO and LUMO wavefunctions, respectively. Thus, ΔE_{ST} can be lowered by either by spatially separating the HOMO and LUMO orbital distributions or by increasing $|r_2\text{-}r_1|$ via introducing a spacer linkage between D-A.[9-11] TADF relies on reverse intersystem crossing (RISC), a process by which non-radiative triplet excitons are thermally up-converted to the singlet state and subsequently emit via fluorescence which can be expressed in terms of ΔE_{ST},

$$k_{rISC} = \frac{2\pi}{\hbar}|\langle S|\hat{H}_{SOC}|T\rangle|^2\rho_{FC} \quad 5$$

Where $|\langle S|\hat{H}_{SOC}|T\rangle|$ denotes spin-orbit coupling (SOC) matrix element and ρ_{FC} represents frank codon density[12,13] given by eq. 2,

$$\rho_{FC} = \frac{1}{\sqrt{4\pi\lambda k_B T}} exp\left[\frac{-(\Delta E-\lambda)^2}{4\lambda k_B T}\right] \quad 6$$

ΔE is the activation energy of rISC, λ specifies the reorganization energy, k_B is the Boltzmann constant, and T denotes the absolute temperature. Thus, efficient TADF requires small ΔE_{ST}[14,15], which is achieved through molecular design strategies that spatially separate the highest occupied molecular orbital (HOMO) and lowest unoccupied molecular orbital (LUMO) over donor and acceptor moieties, respectively. The conventional donor-acceptor (D-A) strategy has enabled highly efficient TADF-OLEDs, but their long-range CT states typically cause large Stokes shifts and broad emissions (FWHM ≈ 80 nm), limiting colour purity. Hatakeyama et al. (2016) introduced the multi-resonance (MR) design, in which HOMO and LUMO are positioned on adjacent atoms within a rigid BN-doped framework, producing short-range CT, reduced reorganization energy, and narrow emission bands (<30 nm).[16] This localized electron distribution also lowers ΔE_{ST} and enhances the k_{rISC}, making MR-TADF emitters highly attractive for high-purity OLED displays.[17] Other hybrid systems like circularly polarized luminescent (CPL) emitters and doublet emitters are also being explored which have proven to simplify the OLED architecture. Lately, fourth generation i.e., hyperfluorescent OLEDs are widely explored. In hyperfluorescent system

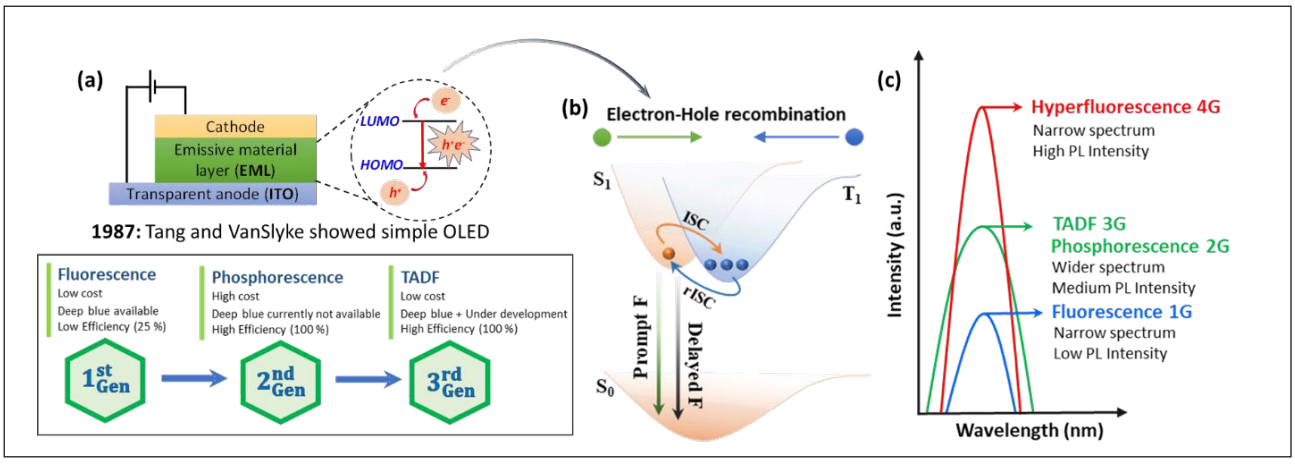

Figure 1: *a) Simple OLED structure and schematic illustration of different generations of emitters, b) schematic illustration of emission mechanism under electrical excitation and c) comparative diagram of emission intensity and colour purity among the different generation of emitters.*

generally a triplet sensitizer used to populate the dopant emitter leading to increase in efficiency. This article summarizes trending emitters co relating their emission mechanisms and molecular design.

TADF Emitters: TADF emitters offer high efficiencies without the use of precious metals. Adachi *et al* first reported a design strategy based on a twisted donor and acceptor framework, owing to steric hinderance effectively reduces the overlap between HOMO and LUMO thereby causing the lowering of ΔE_{ST}. In 2012, they developed **4CzIPN** with multiple carbazole donors and benzonitrile as the acceptor, setting a major milestone in TADF-OLED emitter development. An OLED with **4CzIPN** as the emitter showed an outstanding EQE of 19.3 % compared to traditional fluorescent emitters. [6] Later, several reports were published on donor acceptor TADF emitters.

Carbonyl-based cores act as strong electron-withdrawing acceptors and contain oxygen atoms with lone pairs that influence excited-state behaviour.[18–21] From equation 5, it can be inferred that along with small $\Delta E_{ST,}$ sizable SOC is crucial for efficient rISC process.[22] Thus, incorporating aromatic carbonyl units to enhance SOC and using D-A architectures to reduce the ΔE_{ST} is one of the widely explored molecular design. In 2016, Su et al. reported a deep blue ketone derivative named **i-DMAC C** that used two rigid donors, 9,9-dimethyl-10- phenyl-9,10-dihydroacridine, to link with a carbonyl group (Figure 2a). The rigid, compactly conjugated structure yielded narrow deep-blue emission in toluene (λ_{PL} = 414 nm, FWHM = 49 nm), but its extended conjugation results in a relatively large ΔE_{ST} (0.29 eV), slow k_{RISC} (0.3×10^3 s^{-1}), and moderate PLQY (48%), leading to a deep-blue device emission at 450 nm with CIE (0.15, 0.11) and an EQE of 10.9%.[23] In 2018, Data et al. reported the acridone-based TADF derivative 1 (**BCbAc**). Despite of large ΔE_{ST} (0.42 eV), **BCbAc** displayed TADF properties and its device displayed EL at 458 nm with FWHM of 53 nm and EQE of about 8.2%.[24] Recently our group also developed a N-substituted acridone-dibenzoazepine/carboline derivatives (**Aze-Me-Acr** and **Aze-Anisyl-Acr)** with twisted electron rich dibenzoazepine as donor providing limited rotation at donor–acceptor bond. OLEDs using **Aze-Me-Acr** and **Aze-Anisyl-Acr** emitted green (CIE 0.28, 0.65) and yellowish-green (CIE 0.39, 0.56), respectively, with **Aze-Me-Acr** doped in CBP achieving an EQE of 12.8%. EL profile and plot of EQE and current efficiency versus current density is shown in Figure 2d, e.[25] In 2018, Data and co-workers also showed xanthone-based donor–acceptor derivatives to achieve TADF. OLED device of 10 wt % CBP-doped **Xan-DPA** has been reported with the highest external efficiency of about 7.08%. Later our group worked on planar carbazole and twisted dibenzoazepines as donors to induce rigidity and twisted geometry in the molecular design to induce rigidity and twisted geometry in molecular design.[26] The device structure of CBP-doped OLED with **Xan-azepine** (5 wt%) is shown in Figure 2b. The doped device resulted in a maximum power efficiency, current efficiency, and EQE of 16.92 Lm/W, 11.40 Cd/A, and 19.62%, respectively, and showed a very small roll-off of 2.75% (Figure 2c). [27]

Although various D-A ketone derivatives achieve TADF primarily through twisted donor–acceptor geometries, strategies such as introducing bridging bonds, weak hydrogen bonding, or tuning donor/acceptor strength can increase rigidity, lower reorganization energy, and blue-shift the emission. While these approaches can reduce FWHM (49–70 nm), most ketone-based D–A systems still struggle to simultaneously achieve narrowband emission and high device efficiency because their long-range ICT character is intrinsically unsuitable for very sharp spectra.

MR framework has been essential based on the assimilation of donor (N, O, S) and acceptor (B, C=O) atoms localizing HOMO and LUMO on sites separated by one atom. Hatakeyama et al. in 2016 first reported **DABNA** as a blue MRTADF emitter with B and N at opposite ends, leading

to the effective separation of the HOMO and LUMO. The OLED with **DABNA** as the emitter displayed an EQE_{Max} of approximately 13.7% with an FWHM of 26 nm. [16] Yuan et al in 2019 first reported a new class of MRTADF emitter, quinolino[3,2,1-*de*] acridine-5,9-dione (**QAO**), with multiple resonance effect of the carbonyl and the nitrogen atoms for effective HOMO-LUMO separation (Figure 2). Using **QAO** as emitter in OLEDs, noteworthy EQE_{Max} of 19.4 % with a small FWHM of 39 nm could be achieved. Henceforth, **QAO** core has been widely explored with selective substitution of donor, incorporation of heteroatom, enhancing π-conjugation across the core, etc.[28] A very recent report by Jin et al on new quinolino[3,2,1- de]acridine-5,9-dione (QAO) based multi resonant emitters *viz*., **DPA-QAO**, **PhDPA-QAO** and **MeODPA-QAO**, emphasizes correlation between π-π interactions, molecular twisting and photo-physics of these materials (Figure 2). Using an exciplex co-host system, these materials achieved impressive EQEs of 23.83%, 26.01%, and 11.34%, respectively.[29] Wu et al in 2023 presented a new design strategy by fusing together boron and carbonyl containing acceptor groups in MRTADF frameworks. This new combined emitter (**DOBDiKTa**) demonstrated pure blue narrowband emission with efficient TADF character. OLED using **DOBDiKTa** as the emitter displayed EQE_{Max} of 17.4% with EL corresponding to (CIE) coordinates of (0.14, 0.12).[30] Similarly, Lin et al presented fused carbazole MR-TADF emitter **DBDSe** and **DBDS** with heavy atoms like Se and S, which gave ultra-pure deep-blue light at λ_{EL} = 456 nm (solution λ_{PL} = 453 nm) with a narrow FWHM of 17 nm and achieves a PLQY of 99%. The non-sensitized OLED using exhibits **DBDSe** as emitter displayed EQE_{Max} of 40.5%, and maintains 38.4%/28.2% at 100/1,000 cd m^{-2}, with ΔE_{ST} = 0.17 eV, k_{RISC} = 3.0×10^{6} s^{-1}, and a horizontal dipole ratio $\theta_{||}$ = 99%.[31]

Emerging Directions-CPL Active and Radical-Based Emitters: Beyond classical TADF and phosphorescent designs, two innovative directions are rapidly gaining attention:

Chiral emitters enabling circularly polarized luminescence (CPL), which can reduce external optical losses and enable high-contrast 3D/AR displays. To further enhance the performance of MR-TADF emitters, introducing asymmetry in these emitters has emerged as focal point in organic electronics.[32] Emitted light is often non polarized and is converted into circularly polarized luminescence (CPL) by using linear polarizer and quarter wave plate, however, this leads to serious loss of brightness

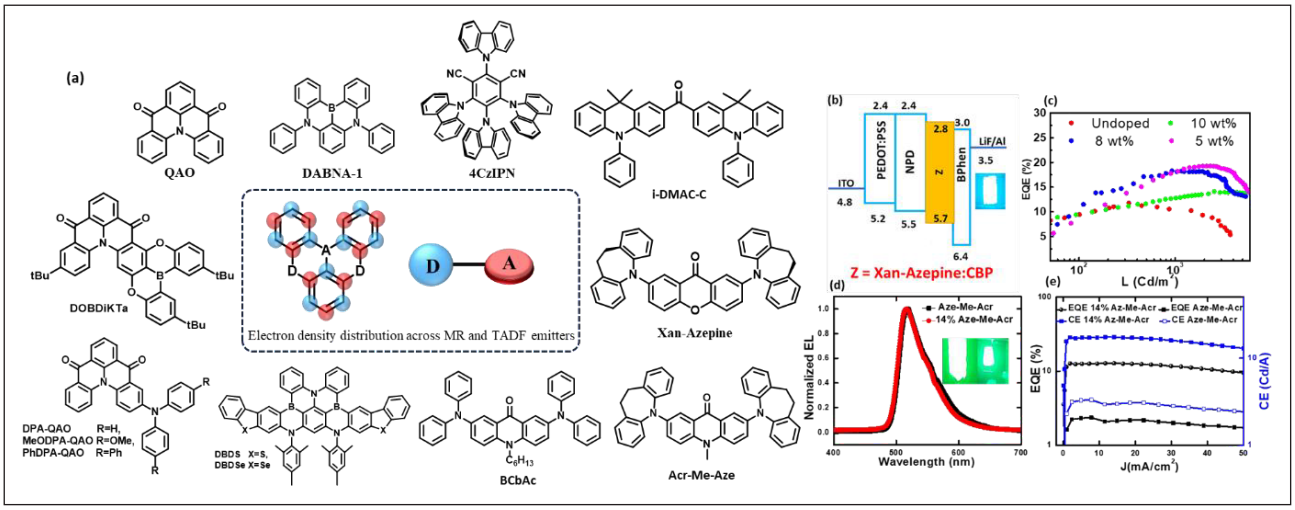

Figure 2: *(a) Selective examples of TADF and MRTADF emitters, (b), (c) device geometry & plot of EQE vs Luminescence for* **Xan-Azepine**, *(d) and (e) EL profile and plot of EQE vs current density for* **Acr-Me-Aze**.

along with complicated device architecture.[33] The degree of molecular asymmetry is quantified by the luminescence dissymmetry factor (g_{lum}), which measures the degree of circular polarization which is defined in equation:

$$g_{lum} = 2\left(\frac{I_L - I_R}{I_L + I_R}\right)$$

where I_L and I_R are the intensities of left- and right-handed light, respectively. The g_{lum} value is 0 for linearly polarized light while for perfectly right or left CP emission it can range from −2 to +2, respectively.

Although most organic CPL emitters have relatively low g_{lum} values (10^{-4} to 10^{-2}), recent advances-such as incorporating chiral moieties into TADF emitter or multi-resonant structures have shown promise in balancing high luminescence efficiency with enhanced CPL activity.[34] First report on TADF-CPL emitter was made by Hirata et al in 2015, having a stereogenic carbon center linked to donor and acceptor units. No OLED was reported using this emitter owing to its low PLQY about 26% in doped mCP films.[35] Based on the source of chirality, CP-MR-TADF molecules are categorized into point, helical, axial, and planar chirality. A few examples of chiral MR-TADF materials are shown in Figure 3. Sharma et al. first reported CP-TADF emitter with planar chirality by introducing chiral carbazolophane (Czp) donor unit in the triazine-backbone (**CzpPhTrz**). Planar chirality can be achieved by particular arrangement of substituents across the plane such that mirror image of mole ule is not superimposable. Both the enantiomers of [2.2] paracyclophane showed mirror image circular dichroism (CD) and CPL with g_{lum} of 1.3×10^{-3}. Sky blue-emitting OLEDs with **CzpPhTrz** as emitter displayed EQE_{Max} of 17% having CIE coordinates of (0.17, 0.25).[28] Later, in 2024 same group reported two enantiomeric emitters **PCP-DiKTa** and **Czp-DiKTa,** having **DiKTa** as MR-TADF moeity with different [2.2] paracyclophane (PCP) derived planar chiral groups. **PCP-DiKTa** showed narrow sky-blue emission while slightly broader redshifted emission was observed for **Czp-DiKTa** with PLQYs of ~95 % and dissymmetry factors g_{lum} of 4×10^{-4}. OLEDs with **PCP-DiKTa** and **Czp-DiKTa** displayed EQE_{max} of 25.7 and 29.2%, with λ_{EL} of 489 and 518 nm, and FWHMs of 53 and 69 nm, respectively.[36]

In 2024, Zhang et al. proposed rigidification strategy through incorporation of multiple 1,4-azaborine units. The progressive increase in the number of 1,4-azaborine units in **3-*C*2** imparted helical chirality resulting in a blue shift in emission bands. Ultranarrow fluorescence (FWHM = ~17 nm) and CPL was observed in these emitters.[37] Recently, Wang et al reported two chiral MR-TADF enantiomers with axial

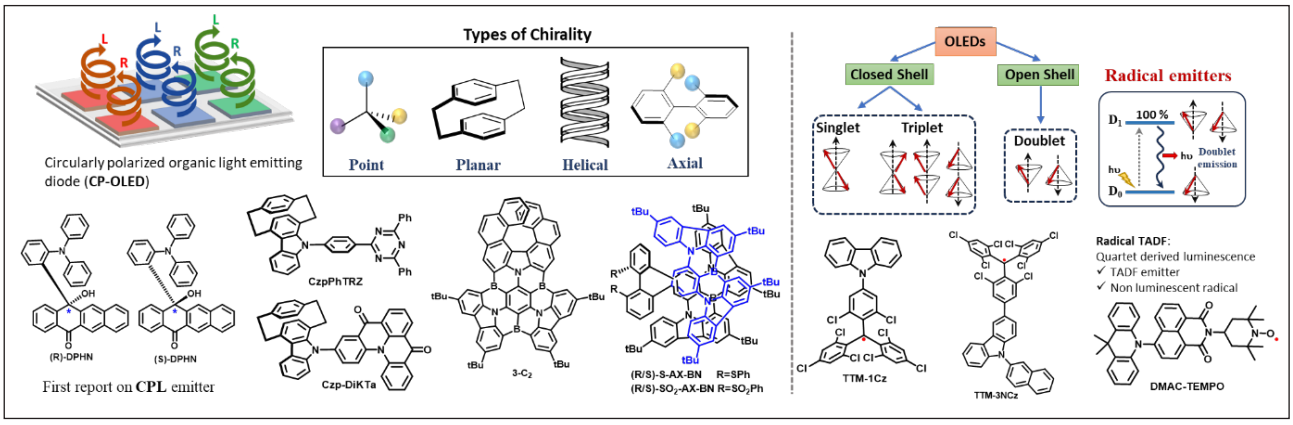

Figure 3: *Design strategy and few examples with different types of chirality used in CP-OLEDs as emitters (left) and organic radicals with doublet emission for OLED (right).*

chirality, namely **(R/S)-S-AX-BN** and **(R/S)-SO_2-AX-BN** by fusing biphenyl skeletons containing sulfur/sulfone with classic B/N-embedded PAHs. These compounds emit pure green light in toluene at wavelengths of 489 nm and 495 nm with FWHM ~20 nm achieving remarkably high PLQYs of 93% and 92% in films doped at 5 wt%. Their OLEDs (2,6-DCzPPy:5 wt% emitter) generate narrow EL at 495 nm (CIE 0.066, 0.481) and 500 nm (CIE 0.068, 0.579), with EQE_{Max} of 33.5% and 31.5%. Both enantiomers demonstrate strong circularly polarized luminescence (CPL), with $|g_{EL}|$ values of $3.3\times10^{-3}/-3.2\times10^{-3}$ for **S-AX-BN** and $2.2\times10^{-3}/-2.1\times10^{-3}$ for **SO_2-AX-BN** in OLEDs, setting record values among axial-chiral MR-TADF analogues.[38] Thus, introducing chiral units in Mr-TADF or D-A TADF emitters can further enhance their performance in OLED device.

Organic radicals with doublet emission: Recently, doublet emission has gained significant limelight due to its ability to harvest dark triplets and achieve 100 % IQE theoretically. Doublet emission occurs in open-shell molecules, specifically monoradicals, in which the outermost molecular orbital is occupied by only one electron. In doublet emission, both the ground and first excited states of monoradicals are doublet states, meaning that there is no spin-forbidden transition. This allows for efficient fluorescence from the doublet-doublet transition.

In 2015, Peng et al. first reported a doublet-emission OLED using a neutral π-monoradical (**TTM-1Cz**). The electroluminescence (EL) peak wavelength lies at 692 nm, and 2.4% EQE was obtained.[39] Later, in 2018, Ai et al reported two new TTM based radicals by incorporating naphthyl (**TTM-3NCz**) and phenyl (**TTM-3PCz**) substituted carbazole to the core. NIR OLED using **TTM-3NCz** as emitter with electroluminescence at 710 nm corresponding to CIE coordinates (0.72, 0.28) displayed EQE_{max} of 27%. This emitter set a breakthrough in doublet-emission OLEDs with highest EQE reported for deep red NIR OLED using radical emitter till date.[40] A contemporary report by Friend's group a new class of radicals showing quartet-derived emission by affixing TEMPO radical to TADF chromophore. Using this design strategy, they developed dark radical with TEMPO affixed at N position of naphthalimide (NAI) core followed by varying donors 3,6-di-*tert*-butylcarbazole (Cz), 9,9-dimethyl-9,10-dihydroacridine (DMAC), and phenoxazine (PXZ) at R1 position. Most efficient rISC from the quartet state was observed in **DMAC-TEMPO** (I_d/I_{tol} = 72%). Since the design strategy does not rely on luminescent π-radical, it promises many permutations and combinations in modelling quartet derived emission.[41]

Hyperfluorescence (HF) Emitters: In the quest for efficient OLEDs with narrow emission spectra, high color purity, and improved

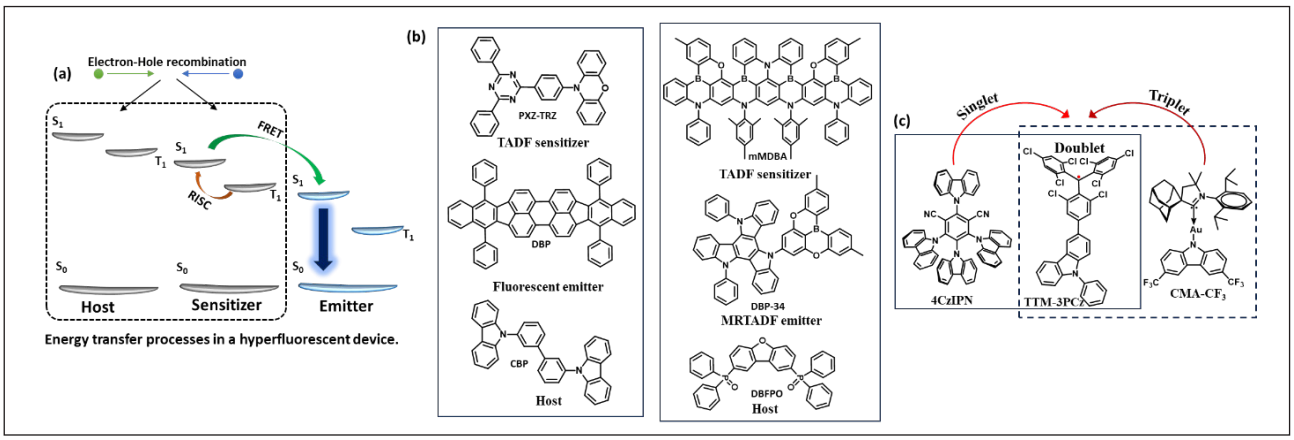

Figure 4: *(a) Schematic representation of hyperfluorescence OLED, (b) selective examples of TADF and MRTADF emitters and (c) use of singlet and triplet sensitizers in doublet emission*

operational stability, an advanced light emission mechanism known as hyperfluorescence is in lime light. Hyper fluorescence effectively bridges broad CT-type TADF emission with the superior spectral sharpness of fluorescent emitters, enabling OLEDs that meet demanding colour standards such as BT 2020.[42] This approach uses TADF or phosphorescent materials as sensitizers or assistants to generate excitons, which are subsequently transferred to highly emissive dopants (Figure 4a). In 2014, Adachi and coworkers first reported blue, green, and red hyperfluorescent OLEDs using **PXZ-TRZ** as a TADF sensitizer and **DBP** as a fluorescent emitter with an EQE_{Max} of about 18.0% (Figure 4b).[2] Recently Yang et al. reported twisted B/N/O-embedded fused-ring frameworks with fully resonating structures of MRTADF emitters. The OLED with **DPA-34** as the emitter displayed an EQE_{max} of about 39.3% with a narrow emission at 457 nm and an FWHM of about 14 nm. Furthermore, an intense blue HF-OLED using **DPA-34** (1 wt%) as the emitter, **mMDBA** (25 wt%) as the TADF sensitizer, and DBFPO as the host displayed an EQE_{Max} of 44.6 % with an FWHM of 16 nm and CIE co-ordinates (0.142,0.099) which meets the BT.2020 standards.[43]

In 2022, Li and Friend et al. demonstrated improvement in efficiency by enabling energy transfer from singlet, triplet, and doublet excitons. By employing a radical:TADF combination, that is, **TTM-3PCz:4CzIPN**, using CBP as the host displayed an EQE_{Max} of 16.4% compared to its radical-only OLED (TTM-3PCz: CBP), which showed an EQE_{Max} of 10.7% for the same charge transport architecture. Further in 2024 they reported radical:Phosphorecent combination using **TTM-3PCz: CMA-CF_3** which gave EQE_{Max} of 16%.[44,45]with subsequent rapid and efficient light emission from the doublet excitons. This is demonstrated with a model Thermally-Activated Delayed Fluorescence (TADF This shows that sensitized OLED architecture can be applied to any system consisting of a host, a triplet sensitizer (TADF/Phosphorescent emitter), and a dopant emitter having intense narrow emission to achieve high efficiency along with colour purity.

Conclusions

In this short review, we summarize recent progress in modern OLED emission pathways, covering TADF, MR-TADF, circularly polarized luminescence (CPL), doublet emission, and hyper fluorescence. Emphasis is placed on how these mechanisms and their corresponding molecular design strategies enhance internal and external quantum efficiencies while achieving narrowband, high-purity emission. We highlight advances in heteroatom-integrated conjugated cores, multi-resonance frameworks, chiral architectures, and sensitizer dopant energy-transfer systems, along with their demonstrated device performances. Overall, this mini-review provides a concise overview of emerging approaches that are shaping the next generation of efficient, color-pure OLED emitters.

Acknowledgement

We acknowledge UM–DAE CEBS for providing the resources necessary to carry out the literature survey.

References:

1 C. W. Tang and S. A. VanSlyke, *Applied Physics Letters*, 1987, 51, 913–915.

2 H. Nakanotani, T. Higuchi, T. Furukawa, K. Masui, K. Morimoto, M. Numata, H. Tanaka, Y. Sagara, T. Yasuda and C. Adachi, *Nat Commun*, 2014, 5, 4016.

3 S. J. N. Dixit, C. Gupta, T. H. Tadavi, K. R. S. Chandrakumar, S. Bose and N. Agarwal, *New J. Chem.*, 2021, 45, 16238–16247.

4 M. A. Baldo, S. Lamansky, P. E. Burrows, M. E. Thompson and S. R. Forrest, *Applied Physics Letters*, 1999, 75, 4–6.

5 H.-Y. Park, S. Ameen, T. Manigandan, H. Kim, R. Kumaresan, D. Song, M. Jeon, J. Lee, J. S. Jin, G. Kim, M. K. Song, J.-S. Jee, B. Kim and S.-H. Jin, *RSC Adv.*, 2025, 15, 7200–7208.

6 H. Uoyama, K. Goushi, K. Shizu, H. Nomura and C. Adachi, *Nature*, 2012, 492, 234–238.

7 A. Monkman, in *Highly Efficient OLEDs*, ed. H. Yersin, Wiley, 1st edn., 2018, pp. 425–463.

8 Y. Im, M. Kim, Y. J. Cho, J.-A. Seo, K. S. Yook and J. Y. Lee, *Chem. Mater.*, 2017, 29, 1946–1963.

9 X. Cai, B. Gao, X. Li, Y. Cao and S. Su, *Adv Funct Materials*, 2016, 26, 8042–8052.

10 A. A. Awasthi, N. Gupta, Q. T. Siddiqui, P. Parab, D. K. Palit, S. Bose and N. Agarwal, *J Chem Sci*, 2019, 131, 94.

11 S. J. N. Dixit, C. V. Gupta, G. S. Naidu, S. Bose and N.

Agarwal, *Journal of Photochemistry and Photobiology A: Chemistry*, 2022, 426, 113710.
12 J. Liang, C. Li, Y. Cui, Z. Li, J. Wang and Y. Wang, *J. Mater. Chem. C*, 2020, 8, 1614–1622.
13 T. Huang, W. Jiang and L. Duan, *J. Mater. Chem. C*, 2018, 6, 5577–5596.
14 H. Nakanotani, Y. Tsuchiya and C. Adachi, *Chem. Lett.*, 2021, 50, 938–948.
15 C. M. Marian, *Annu. Rev. Phys. Chem.*, 2021, 72, 617–640.
16 T. Hatakeyama, K. Shiren, K. Nakajima, S. Nomura, S. Nakatsuka, K. Kinoshita, J. Ni, Y. Ono and T. Ikuta, *Advanced Materials*, 2016, 28, 2777–2781.
17 X. Wu, S. Ni, C.-H. Wang, W. Zhu and P.-T. Chou, *Chem. Rev.*, 2025, 125, 6685–6752.
18 Y. Yu, F. Liu, X. Meng, L. Ding, L. Liao and Z. Jiang, *Chemistry A European J*, 2023, 29, e202202628.
19 K. V. Barhate, K. Glusac and N. Agarwal, *J. Phys. Chem. C*, 2025, 129, 4565–4574.
20 K. V. Barhate, A. P. Wadawale, K. R. S. Chandrakumar and N. Agarwal, *Chem. Commun.*, 2024, 60, 1408–1411.
21 Q. T. Siddiqui, A. A. Awasthi, P. Bhui, M. Muneer, K. R. S. Chandrakumar, S. Bose and N. Agarwal, *J. Phys. Chem. C*, 2019, 123, 1003–1014.
22 F. Di Maiolo, D. K. A. Phan Huu, D. Giavazzi, A. Landi, O. Racchi and A. Painelli, *Chem. Sci.*, 2024, 15, 5434–5450.
23 X. Cai, B. Gao, X. Li, Y. Cao and S. Su, *Adv Funct Materials*, 2016, 26, 8042–8052.
24 P. Pander, A. Swist, R. Motyka, J. Soloducho, F. B. Dias and P. Data, *J. Mater. Chem. C*, 2018, 6, 5434–5443.
25 K. V. Barhate, M. A. Ahemad, J. Dutta, S. Bose and N. Agarwal, *Journal of Photochemistry and Photobiology A: Chemistry*, 2025, 468, 116468.
26 Q. T. Siddiqui, A. A. Awasthi, P. Bhui, P. Parab, M. Muneer, S. Bose and N. Agarwal, *RSC Adv.*, 2019, 9, 40248–40254.
27 K. V. Barhate, P. R. Chanda, M. Poojary, S. Bose and N. Agarwal, *ACS Appl. Mater. Interfaces*, 2024, 16, 62446–62455.
28 N. Sharma, E. Spuling, C. M. Mattern, W. Li, O. Fuhr, Y. Tsuchiya, C. Adachi, S. Bräse, I. D. W. Samuel and E. Zysman-Colman, *Chem. Sci.*, 2019, 10, 6689–6696.
29 Z. Jin, C. Wu, K.-N. Tong, K. Shi, S. Jung, S. Li, X. Wang, Z. Li, W. He, M. Ye, J. Wei, Z. Si, G. Wei and F. Kang, *Materials Today Energy*, 2025, 49, 101833.
30 S. Wu, L. Zhang, J. Wang, A. Kumar Gupta, I. D. W. Samuel and E. Zysman-Colman, *Angewandte Chemie*, 2023, 135, e202305182.
31 H. Lin, Z. Ye, S. Xian, Z. Chen, J. Miao, Z. Huang, C. Zhong, S. Gong, X. Cao and C. Yang, *Advanced Materials*, 2025, 37, 2502459.
32 D. Hall, S. M. Suresh, P. L. Dos Santos, E. Duda, S. Bagnich, A. Pershin, P. Rajamalli, D. B. Cordes, A. M. Z. Slawin, D. Beljonne, A. Köhler, I. D. W. Samuel, Y. Olivier and E. Zysman-Colman, *Advanced Optical Materials*, 2020, 8, 1901627.
33 Y. Kondo, K. Yoshiura, S. Kitera, H. Nishi, S. Oda, H. Gotoh, Y. Sasada, M. Yanai and T. Hatakeyama, *Nat. Photonics*, 2019, 13, 678–682.
34 Y. Cheng, X. Fan, F. Huang, X. Xiong, J. Yu, K. Wang, C. Lee and X. Zhang, *Angew Chem Int Ed*, 2022, 61, e202212575.
35 X.-C. Fan, K. Wang, Y.-Z. Shi, Y.-C. Cheng, Y.-T. Lee, J. Yu, X.-K. Chen, C. Adachi and X.-H. Zhang, *Nat. Photon.*, 2023, 17, 280–285.
36 Y. Xu, H. Hafeez, J. Seibert, S. Wu, J. S. O. Ortiz, J. Crassous, S. Bräse, I. D. W. Samuel and E. Zysman-Colman, *Adv Funct Materials*, 2024, 34, 2402036.
37 F. Zhang, V. Brancaccio, F. Saal, U. Deori, K. Radacki, H. Braunschweig, P. Rajamalli and P. Ravat, *J. Am. Chem. Soc.*, 2024, 146, 29782–29791.
38 X. Wang, S. Xing, X. Xiao, L. Yuan, Z. Hou and Y. Zheng, *Adv Funct Materials*, 2025, 35, 2412044.
39 Q. Peng, A. Obolda, M. Zhang and F. Li, *Angew Chem Int Ed*, 2015, 54, 7091–7095.
40 X. Ai, E. W. Evans, S. Dong, A. J. Gillett, H. Guo, Y. Chen, T. J. H. Hele, R. H. Friend and F. Li, *Nature*, 2018, 563, 536–540.
41 S. Gorgon, P. Murto, D. G. Congrave, L. Matasovic, A. D. Bond, V. Riesgo-Gonzalez, W. K. Myers, H. Bronstein and R. H. Friend, *Advanced Materials*, 2025, 37, 2501164.
42 S. K. Behera and R. D. Costa, *J. Mater. Chem. C*, 2023, 11, 13647–13656.
43 T. Hua, X. Cao, J. Miao, X. Yin, Z. Chen, Z. Huang and C. Yang, *Nat. Photon.*, 2024, 18, 1161–1169.
44 F. Li, A. J. Gillett, Q. Gu, J. Ding, Z. Chen, T. J. H. Hele, W. K. Myers, R. H. Friend and E. W. Evans, *Nature Communications*, 2022, 13, 2744.
45 Q. Gu, S. Gorgon, A. S. Romanov, F. Li, R. H. Friend and E. W. Evans, *Advanced Materials*, 2024, 36, 2402790.

	*M.Sc. in Chemistry from IIT Roorkee (1998), Ph.D. from IIT, Bombay (2004). Postdoctoral positions: Bowling Green State University, OHIO (2004-05), TIFR, Mumbai (2006-09), Max Planck Institute for Polymer Research, Mainz, Germany (2009). Neeraj started his independent research career as an Assistant Professor, at UM DAE CEBS in 2010, where he was promoted to Associate Professor. In his group, research is focussed on the synthesis of heterocyclic organic materials and their excited state studies for organic electronics and biological applications. His group is also interested in the fabrication of solid-state devices such as OLEDs. He is an elected member of the National Academy of Science India (NASI) and a fellow of the Indian Chemical Society, Kolkata. He has published about 70 research articles.*
	***Ms. Komal Vasant Barhate*** *received her M.Sc. degree in Organic Chemistry from Department of Chemistry, University of Mumbai. She joined UM-DAE-CEBS as a Ph.D. student in 2021, under the supervision of Dr. Neeraj Agarwal. Her current research is focused on development of metal free pure organic emitters with TADF and RTP behaviour for their application in OLEDs.*

Spectroscopic Signatures of Copper Nanoclusters: Assembly, Intercluster Conversion, and Excited-state Dynamics

Sameeksha Agrawal* **and Saptarshi Mukherjee***
Department of Chemistry,
Indian Institute of Science Education and Research Bhopal
Bhopal Bypass Road, Bhauri, Bhopal 462 066, Madhya Pradesh, India
**Corresponding author: E-mail: sameeksha20@iiserb.ac.in, saptarshi@iiserb.ac.in*

Abstract

Atomically precise metal nanoclusters (MNCs) are considered the missing link between individual atoms and larger nanoparticles. Owing to their small size and high surface-to-volume ratio, synthesizing photostable Copper nanoclusters (CuNCs) is always difficult. Additionally, advancing their practical applications remains challenging due to difficulties in controlling their structure and optical properties, low stability from easy oxidation, and inherently weak photoluminescence (PL) quantum yields. This review focuses on addressing these challenges *via* developing strategies to enhance their PL intensities and quantum yields, while also modulating their structure and function interrelationship.

1. Introduction:

0.1 Nanoclusters: A Distinct Regime of Nanoscale Materials

The term 'nanoclusters' was first used by Steigerwald and Brus to describe "quantum semiconductor nanoclusters".[1] It was derived from the term "semiconductor clusters", which was used as an alternative for "quantum dots" by Brus in 1986.[2] Further, in 1993, several reports used the term 'nanoclusters' to describe large metal clusters of Copper, Silver, and Gold.[3-5] A metal nanocluster may consist of tens to thousands of metal atoms, in which the metal centres may have direct bonding interactions between them, or they may have the interactions through the bridging ligand as well. In general, the metal nanoclusters having a higher number of metal atoms (hundreds to thousands) do not have a well-defined structure; therefore, they do not show distinct physical and chemical properties. Consequently, the precise characterization is not possible for them as in nanoclusters, and they are termed as 'nanoparticles'.[6] Thus, metal nanoclusters are defined as the atomically precise units having tens to hundreds of metal atoms with a diameter around 2-3 nm, which show distinct photophysical and chemical properties. The metal core in the metal nanoclusters (MNCs) is protected by templates or protecting groups, thereby making the overall size of the nanocluster larger (~2-3 nm).[5] The electronic and optical properties of metal are highly dependent on its size, particularly in the nanometer range (Figure 1).[7,8] In the case of bulk metal, the freely moving electrons in the conduction band are responsible for their high electrical conducting nature and good optical reflectivity. When we reduce the size of the metal further, typically greater than 3 nm, the electrons present on the surface of metal atoms tend to oscillate collectively, if the frequency of light incident on the metal surface matches well with their oscillation frequency. This phenomenon results in surface plasmon resonance, and it renders intense colors to the nanoparticles. On further reduction of the size of the metal (less than 3 nm, i.e., in nanoclusters), the quantum confinement effect becomes operational, and the band structure of the metal gets distorted completely, thereby resulting in the discretization of the energy levels.[8,9] The discrete electronic states generate

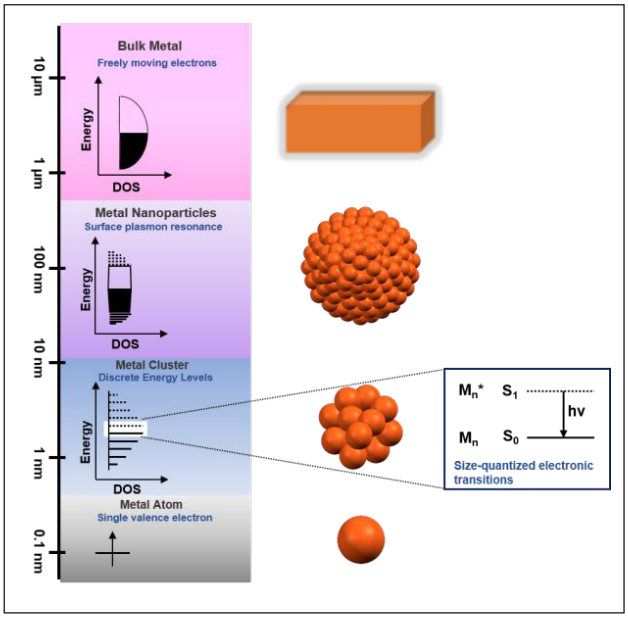

Figure 1. *Size-dependent changes in the band structure of a metal.[8] The corresponding energy differences between the states are marked in the figure.*

molecular-like properties in nanoclusters. Owing to this quantum confinement effect, on interaction with light, metal nanoclusters exhibit electronic transitions between the highest occupied molecular orbital (HOMO) and the lowest unoccupied molecular orbital (LUMO), thus displaying intense absorption and photoluminescence.[8-10] Other molecular-like properties that can be exhibited by metal nanoclusters include intrinsic chirality, catalytic activity, selectivity, and inherent magnetism. Moreover, they may also possess emissive stabilized triplet states similar to a molecule.[11]

In general, metal nanoclusters exhibit a core-shell structure, in which a rigid metallic core is protected by a shell of ligands or protecting scaffolds. There are several kinds of templates or protecting groups that are generally used for this purpose (Figure 2a). These include proteins, dendrimers, amino acids, thiols, phosphines, amines, and carbenes. In earlier stages of the nanocluster chemistry, large templating agents, *viz.*, proteins and dendrimers, were the centre of research, as preparing and stabilising the MNCs using smaller molecules was considered quite a challenging task.[12,13] However, with time, the focus shifted towards preparing MNCs using smaller molecules like thiols, phosphines, and carbenes, because of the cost-effectiveness and easier synthetic protocols.[14,15]

Ligands or protecting groups play two major roles in deciding the chemistry of MNCs:[16]

First, the surface ligands (with the help of functional groups present on their surface or aromatic moieties) interact with the exterior environment, for example, solvent, molecules, cells, and sometimes with other ligands as well, establishing their applications for different purposes (discussed later). Second, the interfacial

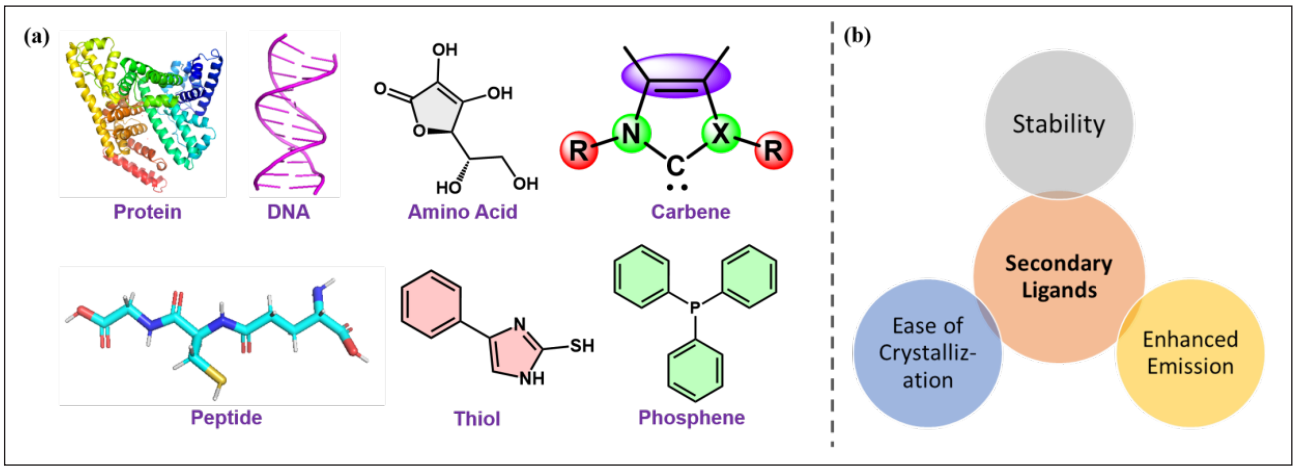

Figure 2. *(a) The different kinds of templates that can be used for the preparation of metal nanoclusters. (b) Schematic diagram representing the role of the secondary ligand upon the photophysical properties and the stability of the nanoclusters.*

chemistry between the surface ligand and metal core determines the stability of the MNCs, and also their photophysical and chemical properties. Modern-day cluster chemistry has reached a point where, by smartly designing the surface ligands, we can induce specific properties in MNCs that can be utilised for desired applications.[16] Additionally, the use of secondary ligands provides significant benefits to MNCs by improving the stability of the cluster framework, thereby preventing degradation and uncontrolled growth (Figure 2b). They also promote ease of crystallization through ordered packing and supramolecular interactions, which are essential for accurate structural determination. In addition, secondary ligands enhance the emission efficiency of MNCs by minimizing non-radiative decay channels.

As discussed earlier, when the size of the metal approaches de-Broglie's wavelength of electrons, and the electrons are confined in a tiny space inside the metal atom, then the properties of the metal are determined by the quantum confinement effect.[8,9] Similarly, in nanoclusters, due to the quantum confinement effect, the confined electron wave functions become a discrete set of energy levels, resulting in the distinct optical and electronic properties of the nanoclusters, including intense photoluminescence. The photoluminescence in MNCs can originate either from the metal core, or the ligand shell, or a combined effect of both. The solid-state photoluminescence model presented by Link *et al.* for the origin of photoluminescence in MNCs explains that, inside the metal core, two types of transitions occur, which determine the photophysical behaviour of MNCs.[17] First, the high-energy inter-band transition resulting from the radiative recombination of the sp- and d-band of the metal atoms.[17] Second, the low-energy transition resulting from the intra-band transitions between the sp-bands across the HOMO-LUMO gap.[17] Also, the surface ligands can donate or accept electrons from the metal core. Therefore, a strong charge transfer between the ligand shell and metal core results in ligand-to-metal charge transfer (LMCT) or metal-to-ligand charge transfer (MLCT).[18] These transitions cause the shift in the emission and absorption spectra of MNCs. Moreover, metal ions present on the surface of MNCs can also accept electrons from the ligands and transfer the charge to the metal core, generating ligand-to-metal-metal charge transfer (LMMCT).[18] This phenomenon also causes major shifts in the absorption and emission bands of the MNCs. Further, the electronic properties and size of the ligands can also be used to tune the size of the cluster core, which may generate different spectroscopic signatures of the MNCs.

Additionally, the supremacy of the MNCs as new generational fluorophores stems from the fact that they can be crafted according to the purpose of application. The factors contributing to the flexibility in preparing MNCs include: (i) ligand diversity: various kinds of ligands, such as, thiols, amines, phosphines, alkynes, carbenes, etc., can be used to prepare and stabilize nanoclusters.[12] (ii) choice of the metal precursors: different oxidation states of metal can lead to clusters with different core compositions.[19] (iii) solvent effects: solvents can be used as a tool to tune the properties of MNCs (discussed later).[20] (iv) reaction conditions: temperature, pH, metal-to-ligand ratio can also affect the nuclearity and geometry of the forming cluster.[21,22] (v) post-synthetic modifications: thermal annealing, use of linkers, photo-induced transformations, solvent exposure, etc., can be done to induce assembly processes, intercluster conversion, or to gain catalytic control on the MNCs.[23] The synthetic versatility of the nanoclusters not only lies in the factors mentioned that can be used to synthesise them, but also lies in the multiple synthetic strategies available.[12,24] (i) Bottom-up approach: this is the most common and widely used approach for the synthesis of MNCs.[25] In this process, the complexation of metal ions (Cu^{2+}, Ag^{+}, Au^{3+}, etc.) with the ligands is done through a process of biomineralization. Further, sometimes

the controlled reduction of the metal complex using a suitable reducing agent, for example, $NaBH_4$, Hydrazine, and Ascorbic acid, etc., leads to the formation of stable MNCs.[26] This approach can be used to produce MNCs on a large scale as well, and it offers excellent atomic precision. The use of the reducing agent may not always be required, as the ligands used can also serve the same purpose. (ii) Top-down approach: although this approach is less commonly used but it can yield monodisperse nanoclusters through high-temperature etching.[27,28] This approach involves etching of the larger-sized metal nanoparticles or bulk materials to produce smaller nanoclusters. The process of etching involves thermal or chemical degradation of larger particles, using an etching reagent at higher temperatures for long hours. Though the process is time-consuming but the clusters obtained through this process are generally pure, and it also offers cluster sorting and purification. (iii) Ligand-exchange method: In this method, the ligands present on the surface of nanoclusters are replaced by a more desirable ligand post-synthesis.[29] This method allows optical, catalytic, and chiroptical tuning of the already synthesised nanocluster. This method is extremely useful to modulate the properties of MNCs without disrupting the cluster core. The exceptional features of MNCs make them highly versatile for a range of applications (discussed later).

0.2 Copper Nanoclusters: Opportunities and Challenges

Althogh, a large number of MNCs have been designed, synthesized, and well-explored so far, yet, for copper in particular, there are several challenges to address, and many questions to answer (Figure 3).[27] Copper, being much more earth-abundant, unlike other noble metals, (like gold, silver, and platinum) paves the way to prepare cost-effective and inexpensive metal nanoclusters.[27,30] The CuNCs are scalable, making them ideal to be used in several applications such as catalysis, sensing, and optoelectronics.[27-31] On the contrary, copper offers three oxidation states, i.e., Cu(0), Cu(I), and Cu(II), that can be easily converted to one another due to its low redox potential.[32] Therefore, copper offers the possibility to prepare CuNCs with redox-active behaviour, and valence-dependent optical and catalytic properties.[32] Moreover, due to the small size of copper, the Cu(I)-Cu(I) cuprophilic (d^{10}-d^{10}) interactions can be significantly strong, sometimes comparable to hydrogen bonding in strength (~7-12 kJ/mol).[33] These interactions facilitate supramolecular assembly of CuNCs into ordered architectures and also enhance spin-orbit coupling (SOC), thus stabilizing the triplet-state.[34] Moreover, copper is non-toxic, environment-friendly, and bio-compatible, making it suitable for several biological applications such as, bio-imaging, and eco-friendly photonics.[27]

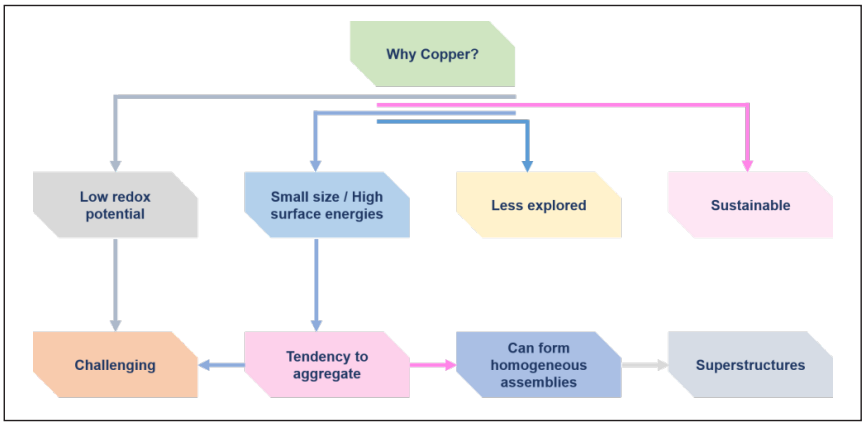

Figure 3. *Key characteristics of copper that make it an ideal candidate for exploration as metal nanocluster assemblies (superstructures).*

However, there are many challenges associated with the preparation and stabilization of copper nanoclusters. One of the major challenges linked with the CuNCs is to control their oxidation (to higher oxidation states) once formed. Copper, due to its very low redox potential, has the tendency to oxidise readily, making it challenging to prepare highly stable CuNCs with a long shelf-life.[27] Moreover, due to

their very small size and quite high surface-to-volume ratio, CuNCs tend to aggregate, making it challenging to keep their optical features intact for prolonged durations.[20,27] Therefore, CuNCs lack structural control compared to other noble metal counterparts (AuNCs, AgNCs, etc.). Thus, predicting the properties and morphology of CuNCs is exceptionally difficult. Furthermore, surface-trapped states formed due to the lower coordination of surface atoms compared to bulk atoms create a possibility for non-radiative recombination of excitons, affecting the photoluminescence quantum yields of CuNCs.[35] In this perspective/review, we have tried to address these challenges associated with the preparation, stabilization, and photophysical properties of CuNCs (Figure 4) by utilizing the phenomenon of: (i) assembly-disassembly-reassembly: to control the photoluminescence properties of CuNCs.[20] (ii) Intercluster conversion/Post-synthetic modifications: to control the molecular size and shape shifting.[36] (iii) Excited-state engineering: to harvest the emission from triplet states of CuNCs (if applicable).[34]

0.3 Assembly-Disassembly-Reassembly Dynamics in MNCs: Controlling Function through Structure

0.3.1 Supramolecular Chemistry and MNCs

Supramolecular chemistry revolves around the formation of hierarchical architectures of molecular entities through non-covalent interactions, including π-π interactions, C-H-π interactions, hydrogen bonding, hydrophobic forces, metal-ligand binding, van der Waals forces, and host-guest interactions.[37] The field of supramolecular chemistry is developing at an accelerating pace due to the interdisciplinary areas it covers, i.e., from chemistry, biology, material science, and nanotechnology to physics. Jean Marie Lehn shared the Nobel Prize in Chemistry in the year 1987 with Charles J. Pedersen, and Donald J. Cram for their "development and use of molecules with structure-specific interactions of high selectivity".[37] Later, in 2016, Ben Feringa, Fraser Stoddart, and Jean Pierre Sauvage, shared the Nobel Prize for design and synthesis of molecular machines, using the principles of

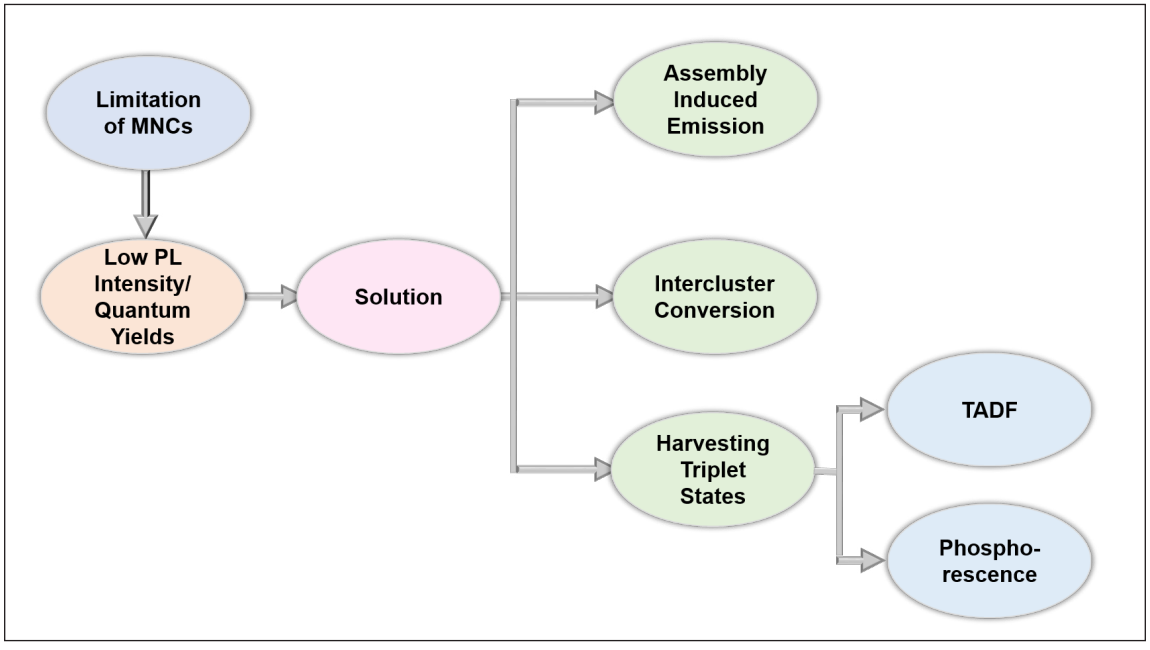

Figure 4. *Schematic representation of the challenges addressed in this review article with the help of various spectroscopic phenomena.*

supramolecular chemistry. When applied to MNCs, supramolecular chemistry has a wide area of opportunities to prepare supramolecular architectures of MNCs having a variety of functions without altering their core structure.[38] Through smart molecular imprinting of the surface ligands, desirable functional architectures of MNCs can be formed with programmable properties.[20,39] The MNCs with a variety of ligand frameworks can be utilized to form 1D nanowires, 2D nano-sheets, and 3D caspids or spheres.[38-42] The formation of these assemblies (superstructures) of MNCs influences the optical properties, emission behaviour, and energy-transfer dynamics.[38] Moreover, it is useful to enhance the catalytic activity of the MNCs, and it can also help to amplify their chirality.[40,41] In CuNCs specifically, the soft nature of Cu(I) and its labile coordination sites can lead to the formation of highly ordered supramolecular architectures.[42]

0.3.2 Driving Forces for the Assembly of MNCs

Assembling MNCs to form homogeneous assemblies requires a delicate balance between various supramolecular interactions.[43] The key driving forces involved in the formation of assemblies of MNCs are:

- Metallophilic Interactions: The non-covalent forces between the closed shell (d^8 and d^{10}) metal ions, i.e., Cu(I), Ag(I), Au(I), and Pt(II), etc., can also be utilized for the formation of self-assembled architectures.[44] In general, metallophilic interactions are considered repulsive in nature; however, for d^{10} linear geometries of the metal complexes, the Pauli repulsions are suppressed.[44,45] Henceforth, the distance between two metal ions becomes less than the sum of their van der Waals radii, resulting in the attractive nature of the forces.[44,45] Recent literature reports suggest that the metallophilic interactions can be as strong as hydrogen bonding interactions, promoting the formation of metal nanocluster assemblies.[45] Moreover, intercluster metallophilic interactions have also been reported to form self-assembled architectures of MNCs.[46]
- Electrostatic Interactions: The MNCs are protected by several organic ligands (thiols, phosphines, amines, amino acids, etc.). Hence, they can be designed to contain several functional groups at the periphery. For water-soluble MNCs, in particular, these functional groups will be present in the ionic form. By introducing another molecule of opposite charge, electrostatic interactions can be established to form the higher-order assemblies of MNCs without affecting their core compositions.[47]
- Hydrogen-Bonding Interactions: Hydrogen-bonding interactions are considered the strongest among all the non-covalent interactions. Hydrogen-bonding interactions between the surface ligands of MNCs can induce highly directional and homogeneous self-assemblies of MNCs.[20,48] These hydrogen-bonding interactions are sometimes induced by a change of solvents or a change in pH, enabling highly defined reversible assemblies of the MNCs.[20,48]
- Hydrophobic Interactions: Hydrophobic interactions can also drive the assembly formation for non-polar MNCs. The MNCs functionalised with hydrophobic surface ligands have the propensity to aggregate in polar anti-solvents, resulting in the formation of assembled superstructures of MNCs.[49]
- Other Supramolecular Interactions: Other weak non-covalent interactions like C-H-π and π-π interactions also deserve significant attention, similar to all the above-mentioned interactions, as these forces can also create highly stable and luminescent superstructures of MNCs.[20,50]

0.3.3 Importance of Controlled Dynamicity

The ability to control the dynamic behaviour of MNC-based superstructures is essential to achieve tunable functional properties. By regulating the assembly and

disassembly process in MNCs, their optical, electronic, and catalytic behaviours can be tailored precisely. By gaining such control over the supramolecular dynamics of MNCs, stimuli-responsive materials can be created that display reversible changes in response to perturbations in the external environment, such as pH, solvent, or redox conditions.[39,47,48]

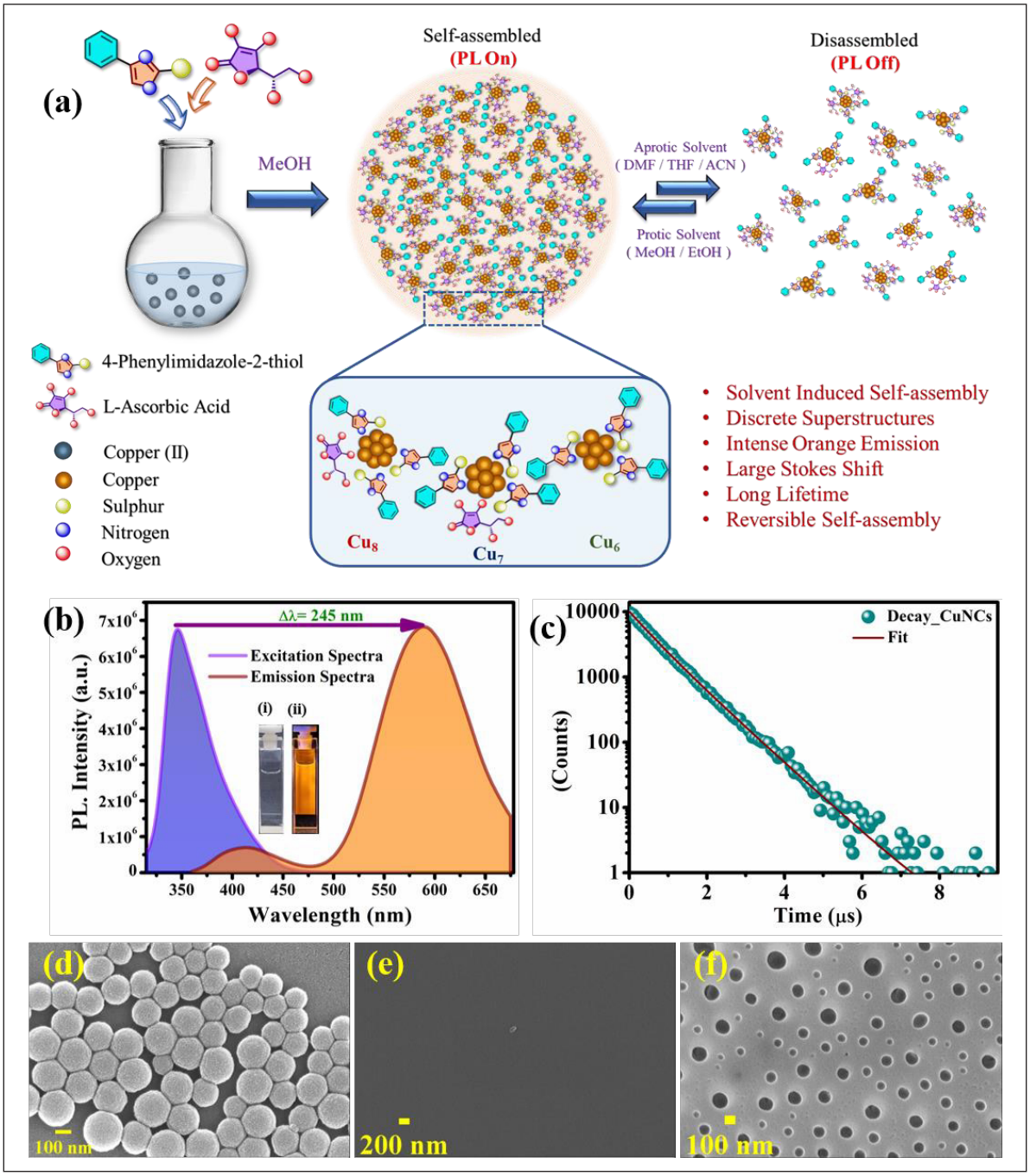

Figure 5. *(a) Schematic representation of the reversible assembly dynamics of the CuNCs using solvent as an external stimulus. (b) Excitation and emission spectra of the CuNC superstructures (CuSSs) depicting a large Stokes shift of ~245 nm. (c) Lifetime decay profile of CuSSs. CuNCs in (d) assembled, (e) disassembled, and (f) reassembled state upon changing the solvent environment from MeOH to DMF and subsequently back to MeOH, respectively. Reproduced with permission from Ref. 20. Copyright 2024, American Chemical Society.*

These materials are of significant importance for versatile applications such as chemical sensing, targeted drug delivery, and adaptive catalysis. Mukherjee and coworkers have recently reported the copper nanoclusters that form highly defined superstructures with the help of supramolecular interactions (H-bond, and CH-π interactions) between the surface ligands (Figure 5a). 4-phenylimidazole-2-thiol was chosen as a surface ligand that tends to form intermolecular H-bond interactions in polar-protic solvents, like methanol and ethanol. The CuNC superstructures display intense orange emission centred at ~590 nm with a large Stokes shift of ~245 nm (Figure 5b). The superstructures also display a very long lifetime of ~718 ns, attributed to the formation of assemblies (Figure 5c and d). Upon changing the solvent environment from polar-protic to polar-aprotic (i.e., dimethylformamide (DMF), acetonitrile (ACN), and tetrahydrofuran (THF)), which tends to act as a proton-accepting solvent, the inter-ligand interaction is disrupted, and it results in the disassembly of the CuNC superstructures (Figure 5e).[20] More importantly, the supramolecular inter-ligand interactions can be re-established by again introducing the polar-protic solvent into the disassembled CuNCs (Figure 5f). The whole process of assembly-disassembly and reassembly happens through a dramatic change in the photoluminescence properties, where it was shown that the CuNCs were emissive only in the assembled-state.[20]

In another example, Zheng and coworkers reported that the dynamic Cu(I)-Cu(I) metallophilic/coordination interactions can reorganize the non-equilibrium, where CuNCs assemble-disassemble and reassemble in a dissipative manner.[51] The switching period of these transient CuNC assemblies can be tuned by varying halide ions, ascorbic acid concentration, oxygen pressure, and pH.[51] Thus, the control over the dynamicity of superstructures offers a platform to develop intelligent, functional materials with programmable behaviour.

0.4 Inter-cluster Conversion: Molecular Shape-shifting in MNCs

0.4.1 Inter-cluster Conversion and Driving Aspects

Inter-cluster conversion in MNCs refers to the structural or compositional transformation of one MNC to another. This process often involves changes in nuclearity, geometry, oxidation state, or ligand-shell. Therefore, this process enables the rational design and synthesis of new clusters and also offers insights into the growth mechanism of MNCs and reaction pathways.[52] Moreover, it is another way to achieve tunable photophysical properties utilizing an external stimulus (light, pH, and redox conditions), which is of significant importance to designing adaptive and switchable nanomaterials (Figure 6).[52] Several driving forces that can trigger the transformation of metal nanoclusters include:

(i) **Ligand-exchange Induced Intercluster Conversion:** This is the most widely used strategy to transform MNCs into those with desirable physicochemical properties by exchanging the surface ligands. The process not only changes the surface chemistry of the nanocluster, but

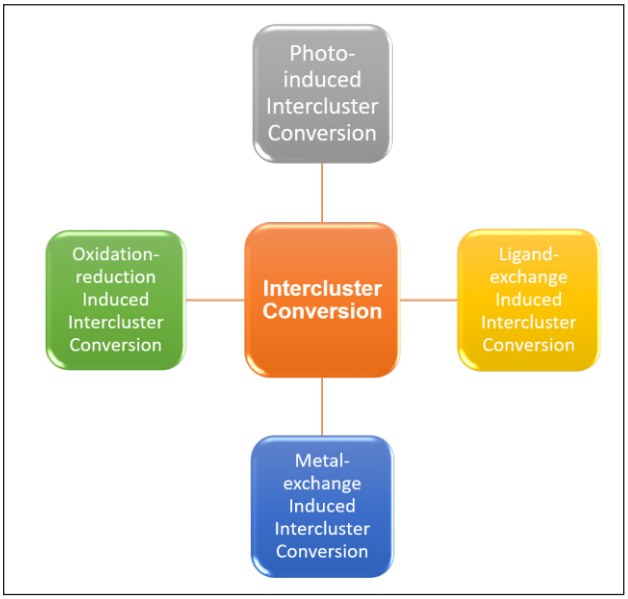

Figure 6. *Various driving forces to trigger intercluster conversion in metal nanoclusters.*

also it can drive the core rearrangement, changes in core composition, and structural isomerisation to form a different nanocluster species.[53]

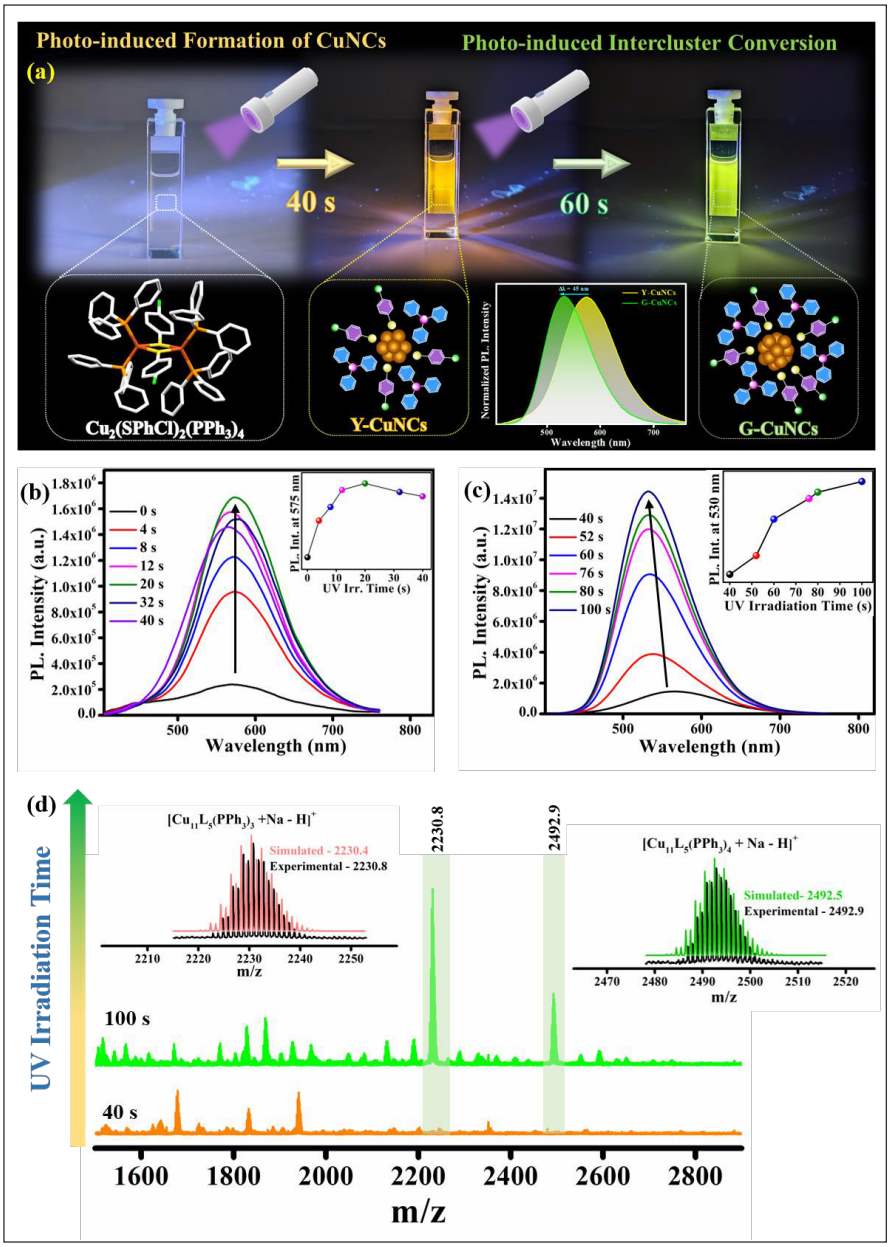

Figure 7. *(a) Schematic representation of the photo-induced formation and intercluster conversion from yellow-emitting copper nanoclusters (Y-CuNCs) to green-emitting copper nanoclusters (G-CuNCs). (b) Photoluminescence spectra depicting the enhancement in the photoluminescence intensity corresponding to 575 nm due to Y-CuNCs formation. (c) Photoluminescence spectra depicting the drastic enhancement in the photoluminescence intensity due to intercluster conversion from Y-CuNCs to G-CuNCs upon UV irradiation. (d) Emergence of two new peaks in the ESI-MS spectra corresponding to G-CuNCs upon UV-irradiation. Reproduced with permission from Ref. 36. Copyright 2024, American Chemical Society.*

(ii) **Metal-exchange Induced Intercluster Transformation:** Metal exchange is a vital strategy to form alloy nanoclusters, first proposed by Wang *et al.*.[54] It was shown that by reacting the gold nanocluster $[Au_{25}(C_2H_4Ph)_{18}]^-$ with different metal complexes of the form M-SC_2H_4Ph, where M = Ag, Cu, Cd, or Hg, customized alloy nanoclusters can be formed.[54]

(iii) **Oxidation-Reduction Induced Intercluster Transformation:** The nanoclusters are highly prone to the redox environment. Thus, changes in redox conditions may also lead to the core composition transformation. For example, Huang and coworkers reported the reversible cluster-to-cluster transformation between Au_6, Au_8, and Au_{11} induced by $NaBH_4$ and H_2O_2.[55]

(iv) **Photo-induced Intercluster Transformation:** Photo-induced intercluster conversion is another useful strategy to transform nanoclusters without the use of any harmful strong reducing reagents. Literature reports have demonstrated the photo-conversion of AgNCs, where the final

nanocluster size was modulated using different wavelengths and intensities of the light source.[56] However, achieving intercluster conversion in small molecule templated copper nanoclusters is considered extremely challenging due to the low redox potential of Copper. Recently, Mukherjee and coworkers have reported photo-induced intercluster conversion in CuNCs protected by small molecules (thiols and phosphine) using UV light as an external stimulus (Figure 7a).[36] The binuclear copper complex was used as a precursor to form yellow-emitting copper nanoclusters (Y-CuNCs) through a process of photoreduction. The process of formation of Y-CuNCs from the binuclear copper complex was monitored through spectroscopic investigations (Figure 7b). Thereafter, the Y-CuNCs displayed intercluster conversion to green-emitting CuNCs (G-CuNCs) triggered by UV-light as an external stimulus. The intercluster conversion happens through a sharp increment in the photoluminescence intensity along with a blue shift of ~45 nm (Figure 7c). The formation of new nanoclusters was evident from the ESI-MS analysis, where the emergence of two additional peaks upon UV-irradiation was attributed to the process of intercluster conversion (Figure 7d). This study emphasizes novel opportunities to control the configuration and electronic characteristics of ligand-protected metal clusters induced by light.[36]

0.4.2 Relevance to Functional Modulation

The change in shape or size of MNCs (induced by intercluster conversion), such as a change in core composition, core rearrangement, surface ligand modification, or symmetry alterations, affects the photophysics of nanoclusters in various ways. (i) The intercluster conversion affects the HOMO-LUMO gap of the system. The increase in the size of the metal nanocluster results in narrow band gaps.[8] Therefore, the larger size clusters tend to have a smaller HOMO-LUMO gap and thus show red-shifted emission bands.[8] Hence, through intercluster conversion, photophysical modulation can be achieved. (ii) The structural changes and packing of the nanoclusters affect the electron-hole mobility in the metal nanoclusters, which results in a change in charge transfer efficiencies.[57] (iii) Structural reorganization changes the surface availability for the catalysis. Low coordination of the metal centres may offer better accessibility to substrates for catalysis.[58]

0.5 Excited-state Engineering in MNCs

Excited-state engineering in MNCs revolves around the modulation of the excited-state energetics, spin-orbit couplings, and singlet-triplet energy gaps, and hence, gaining control over their optical behaviour. Quantum dots (QDs) or semiconductor nanocrystals, as a consequence of the presence of heavy-metal atom(s), display extremely high spin-orbit couplings.[59] Therefore, the exciton-states (bound electron-hole pairs) in such cases cannot be described by conventional singlet-triplet nomenclature, as there is no clear distinction between excited singlet (*S*) and triplet (*T*) states (Figure 8a). Instead, as both orbital

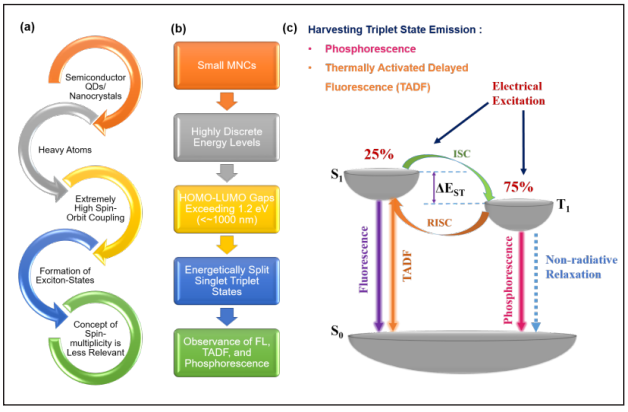

Figure 8. *Schematic representation depicting that (a) the concept of spin-multiplicity is less relevant in semiconductor quantum dots, (b) small MNCs can exhibit triplet-state phenomena. (c) Jablonski diagram representing the various spectroscopic processes in a conventional organic emitter.*

and spin contributions are involved, these states are better characterized by the total spin-orbital quantum number (J).[59,60]

However, in the case of MNCs consisting of a few to tens of metal atoms, due to discrete energy levels and comparatively high HOMO-LUMO gaps, single-electron transitions between the electronic states are possible (Figure 8b). Henceforth, they exhibit molecule-like properties and their excited-state behaviour resembles the closed-shell organic molecules.[59,60] Therefore, the photophysical behaviour in MNCs is described by excited singlet (S) and triplet (T) states using standard models of fluorescence, phosphorescence, and thermally activated delayed fluorescence (TADF).

In general, when an organic fluorophore is excited, only 25% of the molecules come back to the ground state through radiative relaxation from the singlet state; the rest of the 75 % population comes back from the excited triplet state through non-radiative relaxation processes (Figure 8c).[61] Therefore, harvesting the emission from triplet states generates new opportunities to enhance the photoluminescence quantum yields and other optical properties of MNCs. The major advantages of harvesting triplet states in MNCs include extended emission lifetimes, enabling room-temperature phosphorescence, and gaining emission through thermally activated delayed fluorescence.[62] Broadly, strategies to enhance triplet state emission in MNCs include: (i) use of heavy-atom core to enhance the spin-orbit coupling and thus facilitate the emission from triplet states.[59] (ii) formation of rigid supramolecular assemblies of MNCs restricts the molecular motions and also contributes towards stabilization of triplet-states.[34,63] (iii) use of π-acid ligands may also promote charge transfer transitions, such as LMCT/LMMCT, which enhances the emission from cluster-centred triplet-states.[64]

There are mainly two processes through which the excited-state emission from triplet states can be harvested. These are:[61]

- Phosphorescence: Phosphorescence is a distinct photoluminescence process in which, after absorbing photons, the electronically excited species undergoes intersystem crossing (ISC) from the lowest excited singlet state (S_1) to the excited triplet state (T_1). This process involves the change of spin multiplicity; hence, it is often spin-forbidden. However, enhanced spin-orbit coupling facilitates the process; subsequently, the electron returns from the excited triplet state to the ground state (S_0) through a radiative spin-forbidden pathway. Owing to this restriction of spin-forbidden transitions, the process typically exhibits significantly extended emission lifetimes, often ranging from microseconds to seconds.[61] The phosphorescence emission is highly sensitive to the external environment, temperature, and the presence of molecular quenchers, like molecular oxygen.
- Thermally Activated Delayed Fluorescence (TADF): TADF is a distinct photophysical process in which, after photon absorption, the electronically excited species undergo inter-system crossing from the lowest excited singlet state (S_1) to the excited triplet state (T_1). Subsequently, the triplet excitons are thermally up-converted back to the excited singlet-state (S_1) *via* reverse intersystem crossing (*r*ISC) followed by fluorescence emission, and hence it is termed as Thermally Activated Delayed Fluorescence (TADF). The delayed fluorescence has a comparatively longer lifetime than usual fluorescence, often in the microseconds to milliseconds range.[61] The delayed fluorescence is highly dependent on temperature; higher temperature promotes *r*ISC and hence, TADF. For an efficient TADF in a system, the energy gap between the excited-singlet state (S_1) and the excited-triplet state (T_1) should be sufficiently small (< 370 meV) to promote rISC effectively.

In MNCs, phosphorescence and TADF are often facilitated by spin-orbit coupling due to

the presence of metal atoms (Au, Ag, Cu, and Pt), rigid environment (e.g., supramolecular assemblies, crystallization, etc.) and also due to the suppression of non-radiative decay, etc.[59,60] Furthermore, ligand-to-metal charge transfer (LMCT), ligand-to-metal-metal charge transfer (LMMCT), and cluster-centred emission also stabilize the emission from triplet-states. [64]

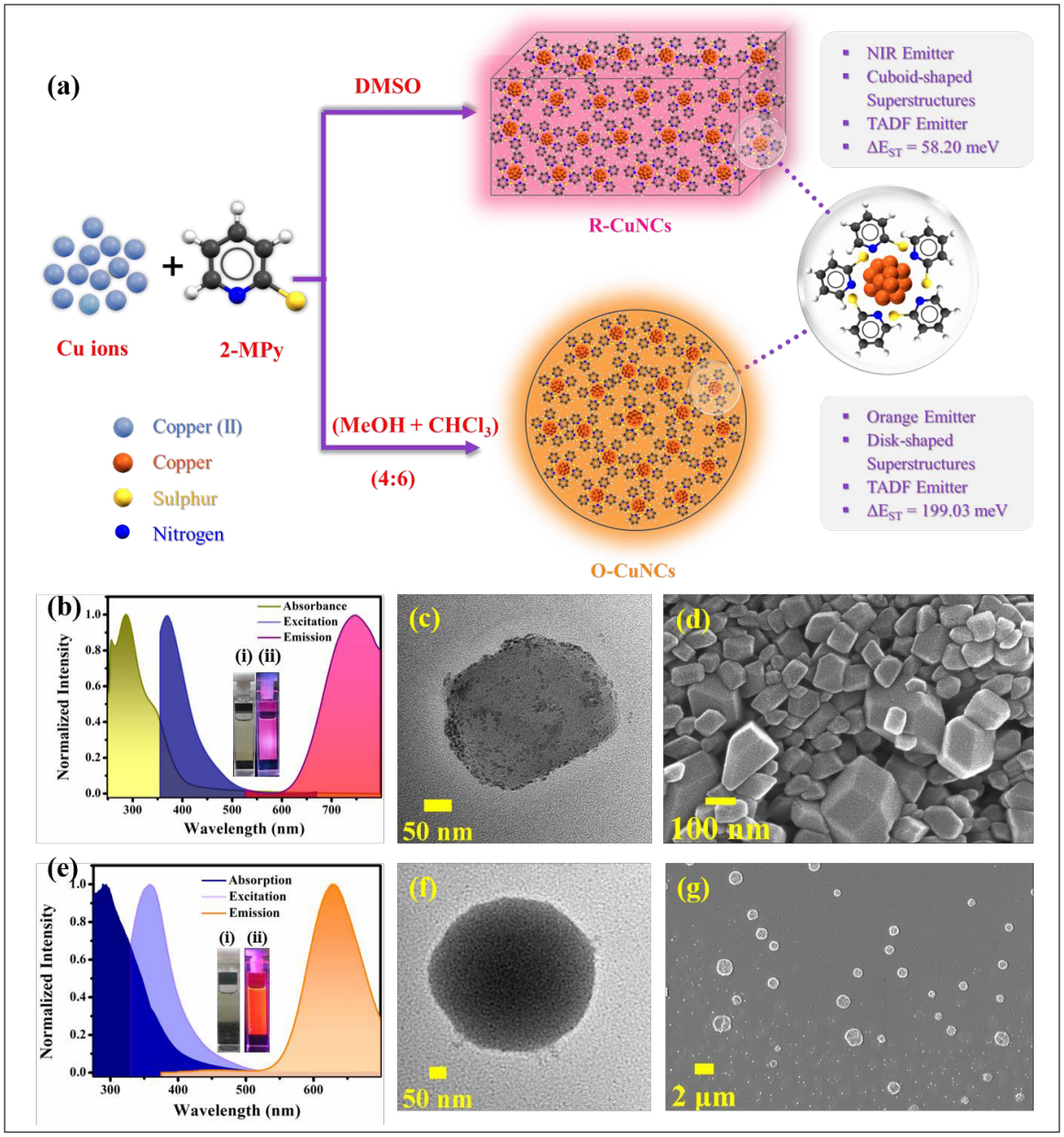

Figure 9. *(a) Schematic representation of the drastic changes in photophysical and morphological signatures of the CuNCs in different solvent environments. (b) Absorption, excitation, and emission spectra of NIR emitting CuNCs in DMSO (R-CuNCs), the inset represents the photographic images of CuNCs under ambient light and (ii) under UV-light. (c) Transmission electron microscopy, and (d) scanning electron microscopy image of R-CuNCs. (e) Absorption, excitation, and emission spectra of orange-emitting CuNCs in MeOH-CHCl3 mixture (O-CuNCs), the inset represents the photographic images of CuNCs; (i) under ambient light and (ii) under UV-light. (f) Transmission electron microscopy, and (g) scanning electron microscopy image of O-CuNCs. Reproduced with permission from Ref. 34. Copyright 2024, the Royal Society of Chemistry.*

Copper, especially in its +1 oxidation state, is considered an ideal choice for achieving TADF and RTP.[65] The Cu(I) centres in nanoclusters due to d_{10} configuration promote moderate spin-orbit coupling, strong enough to promote intersystem crossing from the excited singlet-state (S_1) to triplet-state (T_1) and, in contrast, not overly strong to enhance non-radiative transitions.[65] Moreover, for getting TADF signatures, a small excited singlet-triplet energy gap (ΔE_{ST}) with favourable reverse intersystem crossing (*r*ISC) is also required, which is less encountered in other heavy metals like Au and Pt, which favour phosphorescence rather than TADF.[66] Furthermore, the copper centres form highly flexible coordination geometries which can be tuned with π-acid ligands to enhance metal-to-ligand charge transfer states with long-lived triplet character.[67] In a very recent report, Mukherjee and coworkers demonstrated the copper nanoclusters that display near infrared emission guided by thermally activated delayed fluorescence (TADF). The authors reported how subtle changes in the solvent environment can modulate the energy gap between the excited singlet and triplet state (ΔE_{ST}), which can be further utilized to modulate the photophysical signatures of the CuNCs (Figure 9a). The study emphasizes the fact that the different morphologies of the superstructures of CuNCs tend to stabilize the excited-triplet states to different extents, thus generating dramatic changes in the photophysical signatures.[34] The CuNCs, when studied in DMSO as a solvent, display NIR emission and form cuboidal superstructures (Figure 9b-d). Further, when the CuNCs were prepared in a mixed solvent system of MeOH and $CHCl_3$, intense orange emission was observed. The morphological investigations reveal that the CuNCs form spherical (instead of cuboidal) superstructures in the mixed-solvent environment, resulting in significant changes in the photophysical signatures of CuNCs (Figure 9e-g).[34]

The structural rigidity and compactness of the MNC assemblies play an important role in stabilizing the excited triplet states. The major factors contributing to excited state stabilization and relaxation include: (i) formation of assemblies through intercluster interactions limits the intramolecular rotations and vibrations of the surface ligands, which in turn suppresses the relaxation of excited states through non-radiative decay.[43] Moreover, the assemblies protect the quenching of triplet states from environmental quenchers like molecular oxygen.[68] Embedding the MNCs in a host matrix, e.g., silica, zeolites, may also help to suppress triplet state quenching through molecular oxygen.[69,70] (ii) cuprophilic interactions greatly influence the excited state relaxation dynamics in CuNCs. The degree of compactness of the assemblies plays a critical role in determining the strength of intercluster and intracluster cuprophilic interactions. The increased compactness in the CuNC assemblies enhances the cuprophilic interactions and the average Cu(I)…Cu(I) distances shorten, resulting in a decrease in emission energy and a red shift in the emission maximum.[71] On the contrary, further increment in the compactness of the CuNC assemblies favours greater intercluster cuprophilic interactions, resulting in the increment in the average Cu(I)… Cu(I) distances thus generate a blue shift in the emission maxima.[71] Pradeep and coworkers have recently reported carborane thiol-protected copper nanoclusters, which display strong phosphorescence in the solid state that can be tuned by mechanical grinding. The tunable phosphorescence arises from changes in the cluster packing or environment upon mechanical grinding.[72]

0.6 Application Relevance

At first, MNCs can be served as an efficient catalyst for several organic-inorganic reactions, including oxidation, reduction/hydrogenation, various coupling reactions (C-C coupling, C-N coupling, etc.), click-chemistry, etc.[73] Second, the ultra-small size of MNCs renders them accessible inside the cells, hence, allowing deep tissue penetration, making them a suitable candidate for bio-imaging, drug delivery, and

photo-therapy, etc.[74-76] Moreover, the strong luminescence of MNCs with controlled tunability is highly desirable for their application in sensing, imaging, light-harvesting, and for the fabrication of optoelectronic devices, etc.[21,22,77-79] Additionally, chiral MNCs are opening new possibilities in asymmetric catalysis, spintronics, and for crafting circularly polarized luminescence (CPL) based devices.[80] Phosphorescence and TADF-based MNCs hold significant potential for application in several fields owing to their high emission quantum yields and long-lived emission lifetimes.[81] In optoelectronics, these MNCs can be used to craft next-generation light-emitting diodes (LEDs) with near unity quantum efficiency.[81] The MNCs with long-lived lifetimes can be used for time-gated bio-imaging to eliminate the short-lived component due to background auto-fluorescence, providing better contrast and sensitivity.[14] The phosphorescent MNCs promote the generation of singlet-state oxygen. Hence, they are highly recommended for photo-dynamic therapy.[82] Moreover, the emission intensity and lifetimes of such MNCs are highly sensitive to the exterior environment, oxygen concentration, and temperature, making them suitable for applications based on sensing and environmental monitoring.[83] In photocatalysis, the extended excited-state lifetimes enhance charge transfer and energy transfer processes, promoting photo-redox transformations.[84] Collectively, the phosphorescence and TADF-based MNCs offer a versatile platform for multifunctional, high-performance optical, sensing, and catalytic systems.

1.7 Summary and Outlook

This review focuses on the design, structural engineering, and surface modulation of copper nanoclusters (CuNCs). The central idea of the review revolves around the strategies to improve the photoluminescence intensity and quantum yields of CuNCs, wherein assembly-induced-emission, intercluster conversion, and harvesting the emission from triplet states were demonstrated to work as an effective technique. The challenges associated with the CuNCs have been addressed by establishing rational strategies for controlled supramolecular assembly, modulation of the photophysical properties in the presence of external stimuli, and simultaneously developing an understanding of the structure-property relationship of CuNCs. These help the nanocluster community to uncover the fundamental insights into cluster behaviour while simultaneously advancing their application potential in areas ranging from photonics to catalysis.

Acknowledgements

SA thanks IISER Bhopal for providing the fellowship. SM thanks SERB-ANRF, Govt. of India, for financial assistance. We acknowledge IISER Bhopal for the research infrastructure and the Department of Science and Technology (DST), India, FIST for the TEM facility, Department of Chemistry, IISER Bhopal.

References

1. Steigerwald, M. L.; Brus, L. E. Synthesis, *Annu. Rev. Mater. Sci. 19* (**1989**), 471–495.
2. Brus, L. *J. Phys. Chem. 90* (**1986**), 2555–2560.
3. Burns, J. L.; Spontak, R. J. *J. Microsc. 169* (**1993**), 67–74.
4. Magruder, R. H., III; Yang, L.; Haglund, R. F., Jr; White, C. W.; Yang, L.; Dorsinville, R.; Alfano, R. R. *Appl. Phys. Lett. 62* (**1993**), 1730–1732.
5. Park, H. J.; Shin, D. J.; Yu, J. *J. Chem. Educ. 98* (**2021**), 703–709.
6. Schmid, G.; Fenske, D. *Philos. Trans. A Math. Phys. Eng. Sci. 368* (**2010**), 1207–1210.
7. Kelly, K. L.; Coronado, E.; Zhao, L. L.; Schatz, G. C. *J. Phys. Chem. B 107* (**2003**), 668–677.
8. Díez, I.; Ras, R. H. A. *Nanoscale 3* (**2011**), 1963–1970.
9. Ramalingam, G.; Kathirgamanathan, P.; Ravi, G.; Elangovan, T.; Arjun kumar, B.; Manivannan, N.; Kasinathan, K. Quantum Confinement Effect of 2D Nanomaterials. In *Quantum Dots - Fundamental and Applications*; Divsar, F., Ed.; IntechOpen: London, England, 2020.
10. Du, X.; Zhang, X.; Ma, H.; Zhou, M.; Higaki, T.; Wang, G.; Wang, H.; Jin, R. *ChemElectroChem* 11 (**2024**), e202300528.
11. Zhang, M.; Ji, S.; Zhang, Z.; Zhu, M.; Yao, Q.; Xie, J. *CCS Chem* **2025**, 1–54.
12. Chakraborty, S.; Mukherjee, S. *Chem. Commun. (Camb.) 58* (**2021**), 29–47.
13. Qiao, Z.; Zhang, J.; Hai, X.; Yan, Y.; Song, W.; Bi, S. *Biosens. Bioelectron. 176* (**2021**), 112898.
14. Rai, S.; Agrawal, S.; Mukherjee, S. Intracellular Subdegree Temperature Sensing and Dynamics by Thermoresponsive Silver Nanoclusters as Molecular Probes. *J. Phys. Chem.*

Lett. 16 (**2025**), 9316–9324.
15. Chakraborty, S.; Mukherjee, S. Role of Small Moiety of a Large Ligand: Tyrosine Templated Copper Nanoclusters. *J. Phys. Chem. Lett. 12* (**2021**), 3266–3273.
16. Zhang, B.; Chen, J.; Cao, Y.; Chai, O. J. H.; Xie, J. *Small 17* (**2021**), e2004381.
17. Link, S.; Beeby, A.; FitzGerald, S.; El-Sayed, M. A.; Schaaff, T. G.; Whetten, R. L. *J. Phys. Chem. B 106* (**2002**), 3410–3415.
18. Chen, Y.; Yang, T.; Pan, H.; Yuan, Y.; Chen, L.; Liu, M.; Zhang, K.; Zhang, S.; Wu, P.; Xu, J. *J. Am. Chem. Soc. 136* (**2014**), 1686–1689.
19. Jin, R.; Zeng, C.; Zhou, M.; Chen, Y. *Chem. Rev. 116* (**2016**), 10346–10413.
20. Agrawal, S.; Rai, S.; Mahato, P.; Ali, A.; Mukherjee, S. *J. Phys. Chem. Lett. 15* (**2024**), 4880–4889.
21. Mahato, P.; Mandal, K.; Agrawal, S.; Chopra, D.; Mukherjee, S. *J. Phys. Chem. Lett. 15* (**2024**), 461–470.
22. Shekhar, S.; Sarker, R.; Mahato, P.; Agrawal, S.; Mukherjee, S. *Nanoscale 15* (**2023**), 15368–15381.
23. Chandrashekar, P.; Karmakar, A.; Aparna, R. K.; Singh, L.; Mondal, P. K.; Kundu, S.; Bhattacharyya, K.; Mandal, S. *Chem. Sci. 16* (**2025**), 5726–5734.
24. Chakraborty, I.; Pradeep, T. *Chem. Rev. 117* (**2017**), 8208–8271.
25. Mahato, P.; Shekhar, S.; Agrawal, S.; Pramanik, S.; Mukherjee, S. *ACS Appl. Nano Mater. 5* (**2022**), 7571–7579.
26. Shekhar, S.; Paria, K.; Agrawal, S.; Mukherjee, S. *Chemphyschem 26* (**2025**), e202401021.
27. Baghdasaryan, A.; Bürgi, T. *Nanoscale 13* (**2021**), 6283–6340.
28. Mohite, N.; Paria, K.; Mahato, P.; Mukherjee, S. *J. Surfactants Deterg. 28* (**2025**), 1115–1126.
29. Nguyen, T.-A. D.; Jones, Z. R.; Leto, D. F.; Wu, G.; Scott, S. L.; Hayton, T. W. *Chem. Mater. 28* (**2016**), 8385–8390.
30. Shekhar, S.; Mahato, P.; Yadav, R.; Verma, S. D.; Mukherjee, S. *ACS Sustain. Chem. Eng. 10* (**2022**), 1379–1389.
31. Basu, K.; Paul, S.; Jana, R.; Datta, A.; Banerjee, A. *ACS Sustain. Chem. Eng. 7* (**2019**), 1998–2007.
32. Zhang, L. L.-M.; Zhou, G.; Zhou, G.; Lee, H.-K.; Zhao, N.; Prezhdo, O. V.; Mak, T. C. W. *Chem. Sci. 10* (**2019**), 10122–10128.
33. Pyykkö, P. Strong Closed-Shell Interactions in Inorganic Chemistry. *Chem. Rev. 97* (**1997**), 597–636.
34. Agrawal, S.; Shil, D.; Gupta, A.; Mukherjee, S. *Nanoscale 16* (**2024**), 20556–20569.
35. van der Stam, W.; de Graaf, M.; Gudjonsdottir, S.; Geuchies, J. J.; Dijkema, J. J.; Kirkwood, N.; Evers, W. H.; Longo, A.; Houtepen, A. J. *ACS Nano 12* (**2018**), 11244–11253.
36. Gupta, R.; Agrawal, S.; Rai, S.; Sarkar, J.; Kumari, S.; Shil, D.; Mukherjee, S. *ACS Appl. Opt. Mater. 2*(**2024**), 1880−1890.
37. Lehn, J.-M. *Angew. Chem., Int. Ed. Engl. 27* (**1988**), 89–112.
38. Nag, A.; Pradeep, T. *ACS Nanosci. Au 2* (**2022**), 160–178.
39. Rival, J. V.; Nonappa; Shibu, E. S. *ACS Appl. Mater. Interfaces 12* (**2020**), 14569–14577.
40. Li, D.; Wang, G.; Cheng, L.; Wang, C.; Mei, X. *ACS Omega*, *3* (**2018**), 14755–14765.
41. Shi, L.; Zhu, L.; Guo, J.; Zhang, L.; Shi, Y.; Zhang, Y.; Hou, K.; Zheng, Y.; Zhu, Y.; Lv, J.; Liu, S.; Tang, Z. *Angew. Chem. Int. Ed Engl. 56* (**2017**), 15397–15401.
42. Kolay, S.; Maity, S.; Bain, D.; Chakraborty, S.; Patra, A. *Nanoscale Adv. 3* (**2021**), 5570–5575.
43. Bera, D.; Goswami, N. *J. Phys. Chem. Lett. 12* (**2021**), 9033–9046.
44. Wang, Y.-J.; Shi, X.-Y.; Xing, P.; Zang, S.-Q. *JACS Au 3* (**2023**), 565–574.
45. Wan, Q.; Yang, J.; To, W.-P.; Che, C.-M. *Proc. Natl. Acad. Sci. U. S. A. 118* (**2021**), e2019265118.
46. Han, Z.; Zhao, X.; Peng, P.; Li, S.; Zhang, C.; Cao, M.; Li, K.; Wang, Z.-Y.; Zang, S.-Q. *Nano Res* 12 (**2020**), 3248–3252.
47. Chandra, S.; Nonappa; Beaune, G.; Som, A.; Zhou, S.; Lahtinen, J.; Jiang, H.; Timonen, J. V. I.; Ikkala, O.; Ras, R. H. A. Highly Luminescent Gold Nanocluster Frameworks. *Adv. Opt. Mater. 7* (**2019**), 1900620.
48. Zhu, H.; Li, J.; Wang, J.; Wang, E. *ACS Appl. Mater. Interfaces 11* (**2019**), 36831–36838.
49. Pan, S.; Liu, W.; Tang, J.; Yang, Y.; Feng, H.; Qian, Z.; Zhou, J. *J. Mater. Chem. B Mater. Biol. Med. 6* (**2018**), 3927–3933.
50. Nag, A.; Chakraborty, P.; Bodiuzzaman, M.; Ahuja, T.; Antharjanam, S.; Pradeep, T. *Nanoscale 10* (**2018**), 9851–9855.
51. Zhao, P.; Xu, L.; Li, B.; Zhao, Y.; Zhao, Y.; Lu, Y.; Cao, M.; Li, G.; Weng, T.-C.; Wang, H.; Zheng, Y. *Adv. Mater. 36* (**2024**), e2311818.
52. Zou, X.; Kang, X.; Zhu, M. *Chem. Soc. Rev. 52* (**2023**), 5892–5967.
53. Shibu, E. S.; Muhammed, M. A. H.; Tsukuda, T.; Pradeep, T. *J. Phys. Chem. C Nanomater. Interfaces 112* (**2008**), 12168–12176.
54. Wang, S.; Song, Y.; Jin, S.; Liu, X.; Zhang, J.; Pei, Y.; Meng, X.; Chen, M.; Li, P.; Zhu, M. *J. Am. Chem. Soc. 137* (**2015**), 4018–4021.
55. Ren, X.; Fu, J.; Lin, X.; Fu, X.; Yan, J.; Wu, R.; Liu, C.; Huang, J. *Dalton Trans. 47* (**2018**), 7487–7491.
56. Jana, A.; Jash, M.; Poonia, A. K.; Paramasivam, G.; Islam, M. R.; Chakraborty, P.; Antharjanam, S.; Machacek, J.; Ghosh, S.; Adarsh, K. N. V. D.; Base, T.; Pradeep, T. *ACS Nano 15* (**2021**), 15781–15793.
57. Fetzer, F.; Maier, A.; Hodas, M.; Geladari, O.; Braun, K.; Meixner, A. J.; Schreiber, F.; Schnepf, A.; Scheele, M. *Nat. Commun. 11* (**2020**), 6188.
58. Sun, J.; Wu, Q.; Yan, X.; Li, L.; Tang, X.; Gong, X.; Yan, B.; Xu, Q.; Guo, Q.; He, J.; Shen, H. *JACS Au 4* (**2024**), 3427–3435.
59. Mitsui, M. *J. Phys. Chem. Lett. 15* (**2024**), 12257–12268.
60. Liu, Z.; Luo, L.; Jin, R. *Adv. Mater. 36* (**2024**), e2309073.
61. Uoyama, H.; Goushi, K.; Shizu, K.; Nomura, H.; Adachi, C. *Nature 492* (**2012**), 234–238.
62. Song, Y.; Li, Y.; Zhou, M.; Liu, X.; Li, H.; Wang, H.; Shen, Y.; Zhu, M.; Jin, R. *Sci. Adv. 7* (**2021**), eabd2091.
63. Zhu, J.; Zhao, R.; Shen, H.; Zhu, C.; Zhou, M.; Kang, X.; Zhu, M. *Aggregate (Hoboken)*, *6* (**2025**) e720.
64. Yang, T.-Q.; Peng, B.; Shan, B.-Q.; Zong, Y.-X.; Jiang, J.-G.; Wu, P.; Zhang, K. *Nanomaterials (Basel) 10* (**2020**), 261.
65. To, W.-P.; Wan, Q.; Tong, G. S. M.; Che, C.-M. *Trends Chem. 2* (**2020**), 796–812.
66. Farokhi, A.; Lipinski, S.; Cavinato, L. M.; Shahroosvand, H.; Pashaei, B.; Karimi, S.; Bellani, S.; Bonaccorso, F.; Costa, R. D. *Chem. Soc. Rev. 54* (**2025**), 266–340.
67. Cuttell, D. G.; Kuang, S.-M.; Fanwick, P. E.; McMillin, D. R.; Walton, R. A. *J. Am. Chem. Soc. 124* (**2002**), 6–7.
68. Rival, J. V.; Mymoona, P.; Lakshmi, K. M.; Nonappa; Pradeep, T.; Shibu, E. S. *Small 17* (**2021**), e2005718.

69. Lin, H. T.; Cai, K. B.; Huang, H. Y.; Lin, T. N.; Shen, J. L.; Lin, C. A. J.; Yuan, C. T. *J. Lumin. 187*(**2017**), 269–273.
70. Talite, M. J. A.; Lin, H. T.; Jiang, Z. C.; Lin, T. N.; Huang, H. Y.; Heredia, E.; Flores, A.; Chao, Y. C.; Shen, J. L.; Lin, C. A. J.; Yuan, C. T. *Nanotechnology 27* (**2016**), 345701.
71. Wu, Z.; Liu, J.; Gao, Y.; Liu, H.; Li, T.; Zou, H.; Wang, Z.; Zhang, K.; Wang, Y.; Zhang, H.; Yang, B. *J. Am. Chem. Soc. 137* (**2015**), 12906–12913.
72. Jana, A.; Jash, M.; Dar, W. A.; Roy, J.; Chakraborty, P.; Paramasivam, G.; Lebedkin, S.; Kirakci, K.; Manna, S.; Antharjanam, S.; Machacek, J.; Kucerakova, M.; Ghosh, S.; Lang, K.; Kappes, M. M.; Base, T.; Pradeep, T. *Chem. Sci. 14* (**2023**), 1613–1626.
73. Sagadevan, A.; Murugesan, K.; Bakr, O. M.; Rueping, M. *Chem. Commun. (Camb.) 60* (**2024**), 13858–13866.
74. Yang, J.; Yang, F.; Zhang, C.; He, X.; Jin, R. *ACS Mater. Lett.* **2022**, *4* (7), 1279–1296.
75. Chakraborty, S.; Sagarika, P.; Rai, S.; Sahi, C.; Mukherjee, S. *ACS Appl. Mater. Interfaces 13* (**2021**), 36938–36947.
76. Rai, S.; Mukherjee, S. *Proc. 15th National Symposium on Radiation and Photochemistry (NSRP-2023)*, Goa, India, Jan 5–7, 2023; p 61.
77. Zhou, C.; Sun, D.-W.; Ma, J.; Qin, A.; Tang, B. Z.; Lin, X.-R.; Cao, S.-L. *ACS Appl. Mater. Interfaces 16* (**2024**), 6533–6547.
78. Pramanik, S.; Chithra, S.; Rai, S.; Agrawal, S.; Shil, D.; Mukherjee, S. *J. Phys. Chem. B 127* (**2023**), 6608–6619.
79. Mahato, P.; Thomas, A. S.; Yadav, R.; Rai, S.; Shekhar, S.; Mukherjee, S. *Chem. Asian J. 18* (**2023**), e202300442.
80. Lu, J.; Shao, B.; Huang, R.-W.; Gutiérrez-Arzaluz, L.; Chen, S.; Han, Z.; Yin, J.; Zhu, H.; Dayneko, S.; Hedhili, M. N.; Song, X.; Yuan, P.; Dong, C.; Zhou, R.; Saidaminov, M. I.; Zang, S.-Q.; Mohammed, O. F.; Bakr, O. M. *J. Am. Chem. Soc. 146* (**2024**), 4144–4152.
81. Shi, W.-Q.; Zeng, L.; He, R.-L.; Han, X.-S.; Guan, Z.-J.; Zhou, M.; Wang, Q.-M. *Science 383* (**2024**), 326–330.
82. Ho-Wu, R.; Yau, S. H.; Goodson, T., 3rd. *J. Phys. Chem. B 121* (**2017**), 10073–10080.
83. Dong, X.-Y.; Si, Y.; Yang, J.-S.; Zhang, C.; Han, Z.; Luo, P.; Wang, Z.-Y.; Zang, S.-Q.; Mak, T. C. W. *Nat. Commun. 11* (**2020**), 3678.
84. Cai, Y.-S.; Chen, J.-Q.; Su, P.; Yan, X.; Chen, Q.; Wu, Y.; Xiao, F.-X. *Chem. Sci. 15* (**2024**), 13495–13505.

Saptarshi Mukherjee *is a Professor of Physical Chemistry at the Indian Institute of Science Education and Research Bhopal, India. He completed his B.Sc. and M.Sc. at Jadavpur University, Kolkata, followed by his Ph.D. at IACS Kolkata, under the supervision of Late Professor Kankan Bhattacharyya. He pursued postdoctoral research with Professor H. Peter Lu at Bowling Green State University, Bowling Green, Ohio. He is a Fellow of the Indian Academy of Sciences, Bangalore (FASc), the National Academy of Sciences, India (FNASc), and the Royal Society of Chemistry (FRSC). He is the recipient of the Bronze Medal from the Chemical Research Society of India (CRSI), Young Scientist Award from CRSI, and INSA Medal for Young Scientists, Indian National Science Academy, New Delhi. He also serves as a senior editor of Chemical Physics Impact.*

Sameeksha Agrawal *is currently a Ph.D. student at the Department of Chemistry, Indian Institute of Science Education and Research Bhopal, India. She did her B.Sc. from the Government Model Science College (Autonomous), Jabalpur, followed by her M.Sc. from Dr. Hari Singh Gour University, Sagar, Madhya Pradesh, India. She is carrying out her Ph.D. research work under the supervision of Professor Saptarshi Mukherjee. Her research primarily focuses on spectroscopic and morphological elucidation of dynamic Copper Nanocluster assemblies and their excited-state behaviours.*

Deep Eutectic solvents and ionizing radiation: An overview of generation of highly energetic species and search of a radiation stable DES

Laboni Das
Radiation and Photochemistry Division, Bhabha Atomic Research Centre
Trombay, Mumbai- 400085
Email: laboni@barc.gov.in

Abstract

Deep eutectic solvents (DESs) are complex hydrogen bonded mixtures of suitable hydrogen bond donor and hydrogen bond acceptor, resulting in the formation of a low melting eutectic with melting point much lower than its constituent components. Known for their unique physico-chemical properties these environmentally benign solvents are being explored as an alternative media not only to volatile organic solvents but also to the Ionic Liquids (ILs). In the applications where reactive species or ionizing radiation is involved, the radiation chemical studies of these solvents offer in depth understanding of redox processes and their influence on stability. The effect of ionizing radiation, transient reactive species formation and radiolytic stability of the DESs are a major area of research and needs to be considered before their application in radioactive environment. In this regard the generation of supremely reductive species, the solvated electrons and pre-solvated electrons, their yield, and reactivity in the DESs, reline, ethaline, and glyceline has been reviewed. In addition, the redox and radiation stability of different hydrogen bond donors (HBDs) and hydrogen bond acceptors (HBAs) that constitutes the type III DESs have been screened computationally. Comparison of their fundamental electronic properties based on the long-range corrected density functionals; ωB97XD and LC-BLYP indicated Choline acetate and Malonic acid to be the most appropriate combination among those studied for formation of a redox and radiation stable DES. Synthesis of this new DES with the calculated stoichiometric ratio and study of its fundamental properties along with comparison of radiation stability of this DES with known counterparts of aliphatic ILs forms the crux of this discussion.

1. Introduction

The growing interest for green and sustainable chemistry has provided incessant challenges in the direction of research for neoteric solvents which adheres to the green chemistry principles. However, after a decade of constant research and innumerable publications on ILs, the so called "green" character of these solvents is challenged based on their toxicity and environmental persistence (non-biodegradable) nature.[1] Several bioassays carried out to investigate the eco-toxicity of ILs have evaluated them as toxic towards organisms of varied tropic levels.[2] In addition, their high production and purification cost reduce their overall acceptance and applications in diverse fields. Therefore, efforts to synthesize biodegradable and bio-renewable ILs were betiding. This continuous investigation led to the emergence of a new category of solvents known as the DESs, in the beginning of 21st century. These solvents were first introduced in 2001 by Abbott and co-workers [3] and further defined as Deep Eutectic Solvents in 2003 [4].

DESs are complex hydrogen bonded mixture of HBD and HBA [5]. These eutectics have melting point much lower compared to the individual components forming the mixture; the reason

being the presence of innumerable and different kinds of H-bonds between the components which lower the melting point of the overall eutectic. They can be symbolized by the general formula: $Cat^+ X^- zY$; where

Cat^+: any metal halide or ammonium, sulphonium, imidazolium or phosphonium cation

X^-: Lewis base e.g. halide anion

zY: z number of molecules of Lewis or Bronsted acid Y

These solvents are classified into five major types as shown in table 1.

Table 1. Five different categories of DESs with formula and composition

Classification	Formula	Definition
Type I	$Cat^+ X^- zMCl_x$	MCl_x: Metal halide; where M: metals e.g. Zn, Sn, Fe, Al, Ga, In
Type II	$Cat^+X^- zMCl_x.yH_2O$	$MCl_x.yH_2O$: Hydrated metal halide; M: Cr, Co, Cu, Ni, Fe
Type III	$Cat^+ X^- zRZ$	Cat^+: Ammonium/ sulphonium/ phosphonium/ Imidazolium RZ: amides, acids or alcohols
Type IV	MCl_x + RZ	M: Al, Zn and Z: $CONH_2$, OH
Type V	Non-ionic DES	Composed of only molecules as HBD and HBA

DESs with promising physico-chemical properties viz. non-toxicity, biodegradability, recyclability, low volatility, non-flammability, easy availability and cost-effectiveness are widely acknowledged as green solvents and can further be tailor-made for specific applications.[5] By virtue of their exceptional properties, they are finding wide-spread applications in chemical and nanomaterial synthesis, separation industry, electrochemistry and energy related applications. They are also being explored for efficient storage and removal of radioactive contamination including ^{131}I [6] as well as use in the reprocessing of spent nuclear fuels [7-9] including extraction of minor actinides from raffinate solution [10]. When applied in spent fuel reprocessing these solvents encounter high ionizing alpha, beta and gamma radiations from the nuclear fuel which can result in the oxidation, reduction, primary radical reaction, bond dissociation and several other chemical changes [11]. In all such applications where reactive species or ionizing radiation is involved, the radiation stability of the solvent is a primary concern that needs to be addressed. These versatile solvents being relatively new, present ample opportunities for basic research on the interactions of ionizing radiation in order to appropriately use them in radiation related applications or wherever electron transfer and transport processes are involved.

In the present discussion, the type III DESs (Table 1) are the topic of interest because of their versatility and wide-ranging applications.[5] Since a wide variety of HBDs are easily available hence this particular type of DES is quite adaptable. There is ample scope of tailoring their properties to suite specific application by variation of the HBD. The fundamental and foremost issue that is being addressed in the discussion is the existence and properties of solvated electrons in DES. Further, the pre-solvated electron capture by inorganic ions and DNA base has also been investigated using nanosecond pulse radiolysis which throws light on reductive DNA damage.

In this perspective, the current discussion provides a brief introduction to radiation chemistry of DESs, draws attention to some key findings in the generation of reactive species within such solvent [12], and gives an insight on the radiation stability of DESs [13], [14]. Scheme 1 gives an overall view of the reactions that may

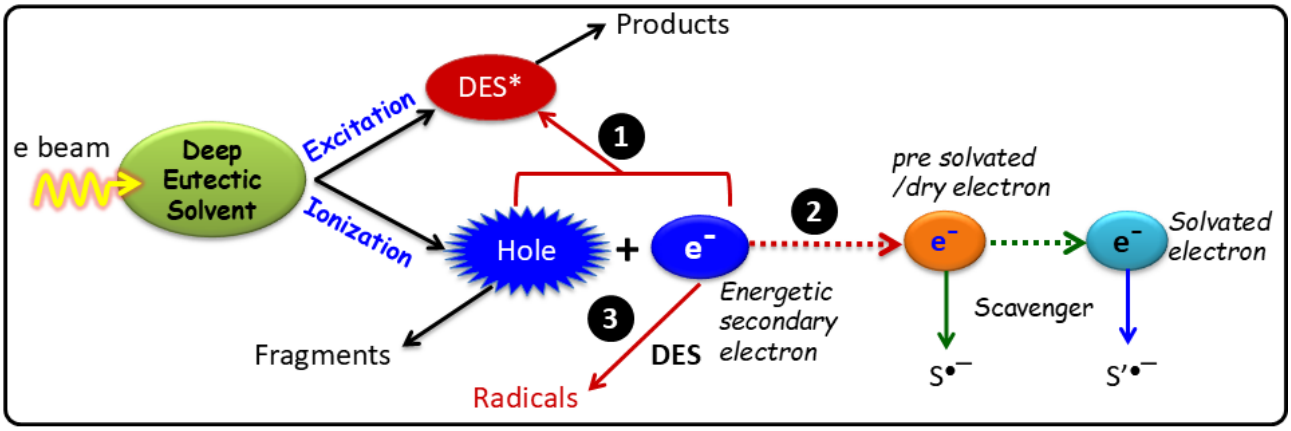

Scheme 1*. Illustration showing the different possible reaction pathways and product formation when Deep Eutectic Solvents interact with ionizing radiation.*

be occurring following the interaction of ionizing radiation with DESs.

In addition, the chemical and radiation stability of a series of type III DESs was also investigated by altering their composition (i.e. the cation, anion and hydrogen bond donor). An enormous number of combination of cations, anions and hydrogen bond donors are possible for synthesis of DES, herein three different commonly available cations (1) Choline (2) Tetra butyl ammonium (TBA) (3) Tetrapropyl ammonium (TPA); five common anions (1) chloride (2) bromide (3) fluoride (4) acetate (5) nitrate; and ten different hydrogen bond donors (1) Oxalic acid (2) Malonic acid (3) Succinic acid (4) Glutaric acid (5) Adipic acid (6) Citric acid (7) Urea (8) Acetamide (9) Methyl urea (10) Dimethyl urea were chosen.

Studies of ΔE_g, IP and EA of the constituent HBAs and HBDs considered can confer an idea about the relative stability of the DES. The energy gap between HOMO and LUMO is an indication of kinetic stability of the molecules. Higher HOMO-LUMO gap implies difficulty in addition of electrons to high energy LUMO as well as to remove electrons from low energy HOMO which makes the molecule chemically unreactive (indicating kinetic stability with respect to formation of any activated complex) [15]. IP indicates the ability of the compound to lose electron and EA defines the power of gaining electron. These parameters can be used as a measure of chemical stability of the compound under oxidizing and reducing conditions, respectively [16,17]. Under the effect of radiation, the DESs can undergo ionization and excitation, further leading to the formation of various radicals and other degradation products, here also IP and EA can give an idea of stability of the DES.

A systematic computational study carried out on the stability of different HBA and HBD based on HOMO-LUMO energy gap, IP and EA gave an idea of the most stable HBA and HBD components (having the highest ΔE_g, IP and EA) that were used for constructing phase diagram theoretically and to predict the melting point and eutectic composition. Later the same predicted composition was used to synthesize the new DES. DSC (differential scanning calorimeter), density, viscosity and FTIR (Fourier transform infra-red) experiments were conducted to characterize the newly synthesized DES. Computational study supported the 1:2 molar ratio of complex formation, stability and H-bonding interactions in the newly formed DES. Further experiments to analyse the radiation stability of the synthesized DES were carried out after irradiating it under gamma source. Finally, the gaseous by-products generated due to irradiation were quantified.

2. Materials and methods:

Experimental:

Choline chloride (≥99%), Choline acetate (>95%), urea (98%), anhydrous ethylene glycol (99.8%), glycerol (≥99.5%), malonic acid (99%), sodium nitrate, pyrene (99%, sublimed grade), and adenosine 5′-diphosphate (ADP) monopotassium salt (≥95%) have been obtained from Sigma-Aldrich and used without purification. Choline acetate has been dried in vacuum oven for 48 h at 100°C (i.e. above its melting point) to remove any absorbed moisture. Choline chloride and urea were vacuum dried at 80°C and 65°C, respectively for 48 h. The DESs were prepared by mixing HBA and HBD in 1:2 ratios at 80°C and stirring continuously until a homogeneous colourless liquid is being formed. After synthesis the DESs were vacuum dried at 65°C for 48 h to remove any volatile impurities and moisture and then stored in vacuum dessicator. The water content in DESs were measured using Karl-Fischer titration [18]. The viscosity of vacuum dried DESs were measured using Anton Paar Physica MCFR10 [19]. The pulse radiolysis experimental setup used (with 7MeV electrons) has been described elsewhere [20], which has been further modified in order to obtain a variable pulse duration using a high voltage pulse-slicer unit [21]. High purity argon gas was used to remove any dissolved oxygen from the solvent and high purity N_2O was used wherever mentioned; and purged for 20 minutes prior to the pulse radiolysis experiments. Dosimetry was carried out using an air-saturated aqueous solution containing 1 x 10^{-2} mol dm^{-3} KSCN assuming $G\varepsilon\,(SCN)_2^{\cdot-} = 2.6 \times 10^{-4}$ m^2 J^{-1} at 475 nm [22]. All pulse radiolysis experiments were carried out at room temperature using 200 ns electron pulses and the dose per pulse was 30 Gy.

Computational:

Geometrical parameters of all the molecular and complex systems have been carried out applying density functional theory (DFT). Three density functionals, a popular correlated hybrid density functional, B3LYP and its modified version to include empirical dispersion correction (B3LYP-D3) as well as range separated dispersion corrected correlated hybrid density functional, namely,ωB97XD and LCBLYP have been considered for the calculations. Hybrid density functional, ωB97XD is known to account H-bond interactions quite accurately. It is reported that range separated DFT functional, namely, LC-BLYP performs well to produce orbital energy gap in a cost-effective way [23]. The basis set 6-311++G(d,p)) was considered for all the calculations. Hessian calculations were also carried out to examine if the equilibrium structures obtained are true minima. All these calculations have been carried out applying *ab initio* quantum chemistry software, Gaussian 16 on a LINUX cluster platform [24]. Visualization of molecular systems is carried out by MOLDEN program [25].

Phase diagram:

Phase diagram is a graphical representation of the thermodynamic properties of a system and it can be constructed from the knowledge of Gibbs energy functions of all phases involved in the system. The phase diagram describes the stability of different phases formed between the interactions of different ratios of Malonic Acid and Choline acetate over a range of temperatures. CALPHAD methodology was applied to obtain a thermodynamic description of the phase through an optimization procedure [26,27]. The basis of modelling of solution phases has been discussed by Sundman [26]. The phase diagram was constructed by minimization of Gibbs energy of possible phases present in Malonic Acid and Choline acetate system. From the calculated binary phase diagram, it was possible to obtain the eutectic composition of the Malonic Acid and Choline acetate mixture. In the present study phase diagram module of FACTSAGE software was used for binary phase diagram calculation [28].

3. Results and discussion:

Three different Type III DESs (i.e. (1) Reline (1:2 mixture of choline chloride and urea) (2) Ethaline (1:2 mixture of choline chloride and

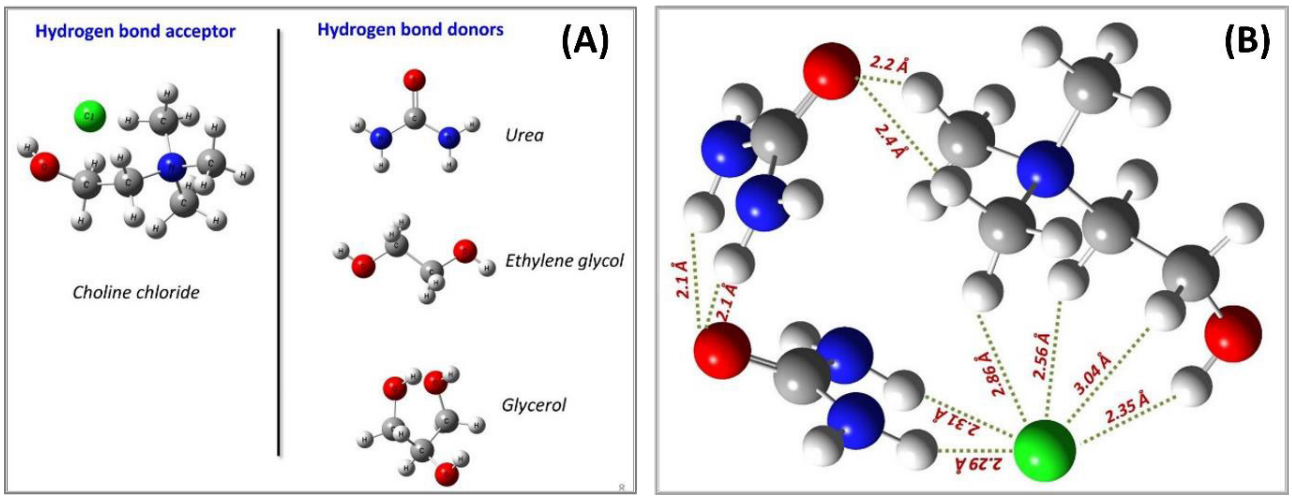

Figure 1. *(A) Chemical structures of the hydrogen bond donors and acceptor used in the study. (B) Hydrogen bonded structure of deep eutectic solvent, reline consisting of choline chloride and urea in the molar ratio 1:2.*

ethylene glycol) (3) Glyceline (1:2 mixture of choline chloride and glycerol)) that have been studied using nanosecond pulse radiolysis technique confirmed the generation of solvated electrons in these media [12]. The individual structures of the HBA (choline chloride) and HBDs have been shown in fig. 1. Fig. 1(B) shows the overall optimized geometry of reline DES.

3.1. Characteristic transient absorption spectra, radiolytic yield, average lifetime and decay rate constant of solvated electron (e^-_{sol}) in the DESs reline, ethaline and glyceline

The solvated electron is the simplest form of an extremely reactive intermediate species which has received supreme attention in physics, chemistry and biology since its inception. The solvated electron could be detected within DES solvent for the first time and its reactivity, radiation chemical yield, average lifetime reviewed. Additionally, there was evidence of the existence of pre-solvated electron in DESs and its capture by DNA bases which focuses on the reductive DNA damage pathway.

The characteristic transient absorption spectrum of solvated electron obtained from de-aerated DESs reline, ethaline and glyceline after the electron pulse radiolysis shows the e^-_{sol} peak at 760nm, 650nm and 610nm respectively. In reline a broad peak at 760nm and a relatively sharp peak at 350nm was observed as shown in fig. 2. The peaks are assigned to the solvated electron, based on evidences of their faster decay, and near complete disappearance in presence of appropriate concentrations of NO_3^- ions, scavenging by N_2O and formation of pyrene anion. The relatively sharp transient absorption peak at the lower wavelength region (i.e. 350nm) remained unaltered even in the presence of these above-mentioned scavengers. This indicates that this particular peak may be due to the hole itself or hole generated species (fig 2(B)).

Table 2. **Comparative study of the absorption maxima, decay rate constant and yield of e^-_{sol} in reline, ethaline and glyceline (at 500 ns).**

DESs	$\lambda_{max}\, e^-_{sol}$ *(nm)*	$k(e^-_{sol})$ (s^{-1})	τ_{avg} *(ns)*	$G_{(e^-sol)}$ *(μmol/J)*
Reline	760	$(7.00\pm0.05) \times 10^5$	1400 ± 10	0.093
Ethaline	650	$(1.22 \pm0.01) \times 10^6$	800 ± 5	0.163
Glyceline	610	$(9.60\pm 0.03) \times 10^5$	1000 ± 3	0.160

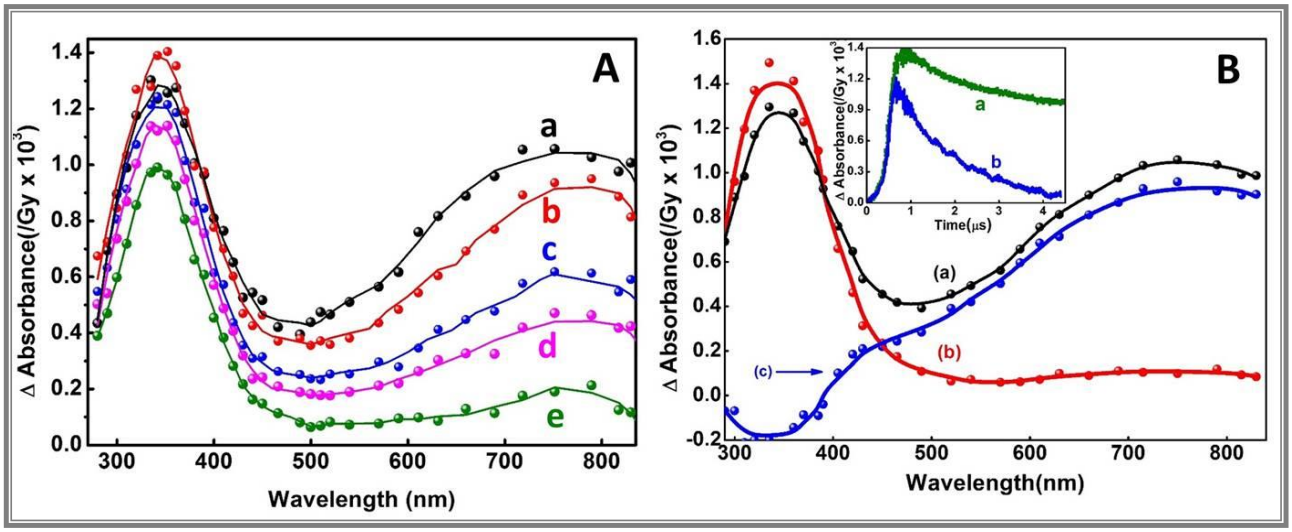

Figure 2. (A) *Transient absorption spectra observed on nanosecond pulse radiolysis of argon purged neat reline at different time scales (a) 700 ns (b) 940 ns (c) 1500 ns (d) 2000 ns (e) 3500 ns* ***(B)*** *Transient absorption spectra obtained at 700 ns in argon purged (a) neat reline (b) reline containing 150 mM sodium nitrate (c) subtracted spectra (a-b).* ***Inset****. Kinetic traces obtained in argon purged neat reline at (a) 340 nm and (b) 760 nm.*

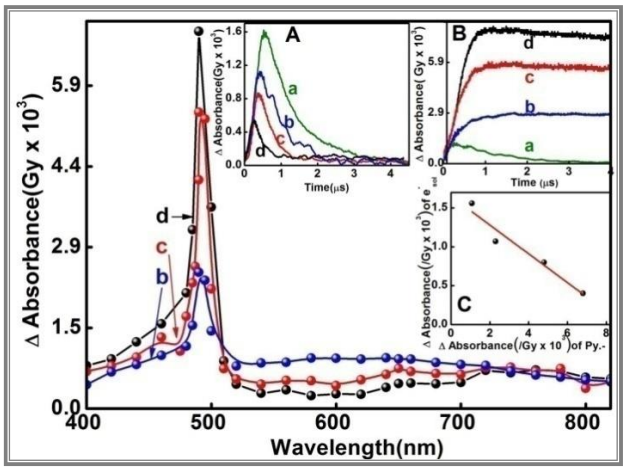

Figure. 3. *Transient absorption spectra of pyrene radical anion at 600 ns at different concentrations of pyrene (b) 1 mM (c) 5 mM and (d) 10 mM added to ethaline, showing an increase in 490 nm peak with an increase in pyrene concentration.* ***Inset (A)*** *Decay traces of solvated electron in ethaline at 650nm showing an increase in decay rate with increase in added pyrene. (a) 0 mM (b) 1 mM (c) 5 mM and (d) 10 mM.* ***Inset (B)*** *Formation traces of pyrene at 490 nm with increase in concentration of added pyrene (a) 0 mM (b) 1 mM (c) 5 mM and (d) 10 mM.* ***Inset (C)*** *Plot of absorbance of solvated electron at 650 nm (y-axis) and pyrene radical anion at 490 nm (x-axis) in ethaline at different concentrations of pyrene (0, 1, 5, 10 mM) from left to right.*

For measurement of solvated electron yield, its reaction with pyrene was observed in the DES (fig. 3). The radiolytic yield of solvated electron in ethaline was calculated to be 0.163 μmolJ^{-1}. In reline and glyceline G (e^-_{sol}) it was found to be 0.093 and 0.16 μmolJ^{-1}, respectively (Table 2).

A comparative data of the obtained absorption maxima, fitted decay rate constant, average lifetime and yield of solvated electron in the three DESs has been shown in table 2. A noteworthy observation is that G(e^-_{sol}) in ethaline and glyceline is almost same but much higher than that in reline. The main difference between reline and the other two DESs is polarity and the number of hydroxyl groups involved in solvating the electron. Among the three DESs reline has the lowest polarity. Further, in reline the hydrogen bonding of only one hydroxyl group is responsible for solvating. These reasons might be responsible for a lower G(e^-_{sol}) value in reline. On the other hand, a higher polarity in ethaline and glyceline as well as involvement of larger number of hydroxyl groups in solvation might lead to higher yield. However, it is difficult to accurately explain the reason of lower radiolytic yield of solvated electron in reline at this stage as

a more detailed study of its solvation dynamics at picosecond time scale is necessary.

The solvated electron decays by first order kinetics in all the three solvents. Average lifetime of solvated electron in reline, ethaline and glyceline has been found to be 1400ns, 800ns and 1000ns, respectively (table 2).

The probable reactions of decay of solvated electron in these media are the following:

$$e^-_{sol} + e^-_{sol} \rightarrow H_2 + 2\text{solvent}(-H)^- \quad [1]$$

$$e^-_{sol} + Me_3N^+CH_2CH_2OH \text{ (choline cation)} \rightarrow Me_3N^+CH_2CH_2O^- + H^\bullet \quad [2]$$

$$e^-_{sol} + HOH_2CCHO \rightarrow HOH_2CCHO^- \quad [3]$$

$$e^-_{sol} + CO(NH_2)_2 \rightarrow CO(NH_2)_2^- \quad [4]$$

As the solvated electron yield is low and also the viscosity of the DES is high so the second-order reaction [1] is unfavorable. Reaction of solvated electron with choline cation is the most appropriate channel for first-order decay. Reline has the highest viscosity so the decay of solvated electron is fastest whereas in ethaline as the viscosity is lowest the decay is slowest (table 2). In ethylene glycol, an early radiation product is glycoldehyde (HOH_2CCHO). Glycoldehyde has been found to be reactive with solvated electron (reaction [3]). Reaction [4] i.e. the reaction of solvated electron with urea is ultraslow, which is an important factor for highest average lifetime of solvated electron in reline.

Earlier quantum chemical calculations in DESs have shown that stabilization occurring by both conventional hydrogen bonds and multiple weak non-covalent interactions such as C-H… lone pair, C-H ….π [29]. Due to existence of such a huge number of different types of H-bonds, it is termed as "an alphabet soup of H-bonds differing in strength and number" [30]. These complex nature of H-bonds [31] controls the solvation environment. Further studies of solvation dynamics in DESs using picosecond electron pulses can give a clearer picture of solvation time and nature; however, it is expected that DESs provide a completely different solvation environment compared to the conventional molecular liquids. And due to this reason, there is probability of existence of precursors of solvated electrons for longer timescale.

3.2. Existence of pre-solvated electron and its efficient capture using DNA nucleobase

A major precursor of solvated electron is its pre-solvated form, which is more reactive than the solvated one. It has higher potential energy and higher mobility than the solvated one since it is less deeply trapped. Also, the yield of pre-solvated electron $G(e^-_{pre\text{-}sol})$ is double than that of solvated electron $G(e^-_{sol})$. So, the identification of existence of pre-solvated electron in a medium is important for determining the total reducing environment present in a solvent at early timescale. Evidence of pre-solvated electron has been obtained by femtosecond spectroscopy in water [32,33] and picosecond in ILs [34]. In the studies, decrease in initial yield of solvated electron was observed on addition of nitrate ions as well as the DNA nucleobase Adenosine, which gives the primary evidence of existence of pre-solvated electrons (fig. 4 (A) and (B)). In recent times the role of pre-solvated electrons in reductive damage of DNA is under significant consideration. Hydroxyl radicals are known to induce indirect radiation damage to DNA; but even this reductive damage could account for the total damage caused in radiation induced DNA damage. In a recent study with DNA nucleotides, it has been shown that the effective reductive damage caused by e^-_{presol} in water is twice than the amount of damage caused by the oxidative pathway (by hydroxyl radicals).[35]

3.3. Radiation stability of DESs

The effectiveness of the application of DES will depend upon the stability of the DES (chemical and radiation). Chemical stability of the DES both under reducing and oxidizing conditions is an important aspect for its consideration as electrolytes in batteries and supercapacitors and any other electrochemical applications. Apart

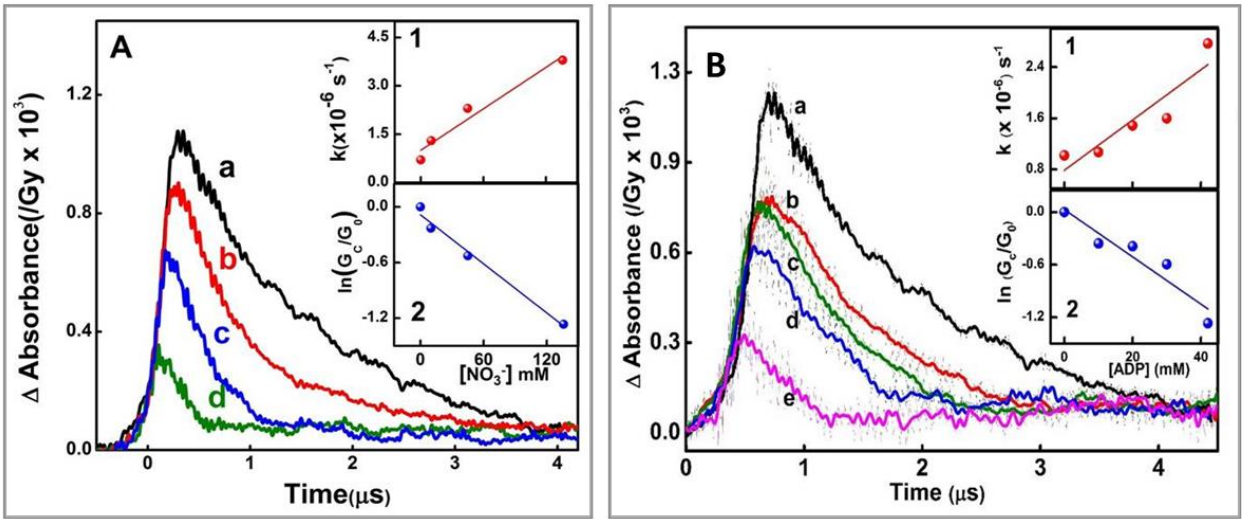

Figure 4. (A) *Decay traces of solvated electron at 760 nm in argon purged reline showing an increase in decay rate with the increase in nitrate ion concentration (a) 0 mM, (b) 10 mM, (c) 45 mM and (d) 136 mM.* ***Inset (1):*** *Plot of observed first order decay rate constant of solvated electrons with increasing concentrations of nitrate ion in reline.* ***Inset (2):*** *Plot of ln(G_c/G_0) versus concentration of added nitrate ions in reline.* ***B)*** *Decay traces of solvated electron at 760nm in argon purged reline with increasing concentration of adenosine 5′-diphosphate monopotassium salt (ADP) (a) 0 mM, (b) 10 mM, (c) 20 mM, (d) 30 mM and (e) 42 mM.* ***Inset (1):*** *Plot of observed rate constants of e^-_{sol} decay vs. concentration of ADP in reline.* ***Inset (2):*** *Plot of ln (G_c/G_0) vs. concentration of ADP in reline.*

from that, radiation stability of the DES is the primary concern to be considered for applications in nuclear science and technology. The Type III DESs which are our present topic of discussion are composed of HBA and HBD as was discussed earlier. Accordingly, the overall redox and radiation stability of DES is expected to depend primarily on the stability of the individual HBA and HBD. The detailed list of fifteen HBAs and ten HBDs along with their optimized geometry (after consideration of all possible conformers) which was studied is tabulated in ref [36].

A systematic computational study was carried out on the stability of different HBA and HBD based on HOMO-LUMO energy gap, IP and EA. The most stable HBA and HBD components (having the highest ΔE_g, IP and EA) were chosen based on the comparison of the relative HOMO-LUMO energy gap, IP and EA. The screening based on these fundamental electronic properties of molecular systems was applied to select choline acetate and malonic acid as the suitable HBD and HBA pair to form radiation and redox stable DES.

This pair of HBA and HBD was used for constructing phase diagram theoretically to predict the melting point and eutectic

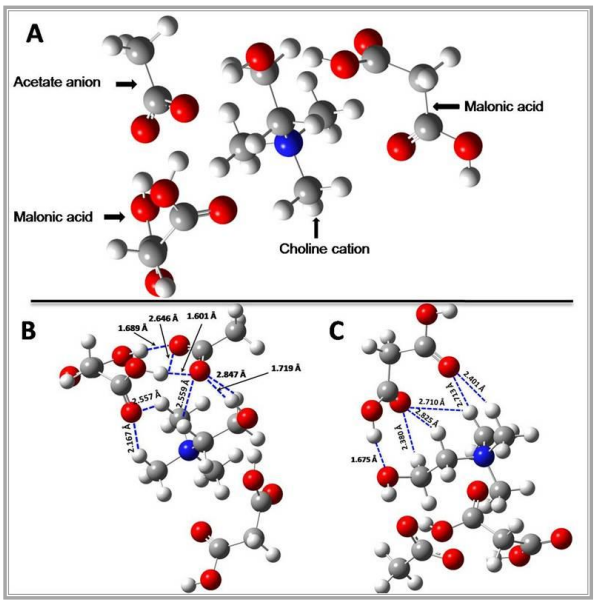

Figure 5. (A) *Optimized geometry of 1:2 complex of choline acetate and malonic acid at ωB97XD/6-311++G(d,p) level of theory* ***(B)*** *H-bonds and H-bond distances between choline, acetate and one malonic acid molecule in the 1:2 mixture* ***(C)*** *H-bonds and H-bond distances between the second malonic acid and choline molecule.*

Table 3. Comparison of physical properties of the new synthesized DES with other popular DESs.

DES	HBA	HBD	Mp or T_g (°C)	Density (g cm^{-3})	Viscosity (Cp)
Reline	ChCl	Urea	12[4], 1[37]	1.24[5]	632[5]
Ethaline	ChCl	Ethylene glycol	-66[39]	1.12[5]	36[5]
Glyceline	ChCl	Glycerol	-40[39]	1.18[5]	376[5]
Maline	ChCl	Malonic acid	-14 (T_g)[40]	1.19[40]	547.9[40]
New DES	$ChCH_3COO^-$	Malonic acid	-75 (T_g)	1.25	497.5

composition. Later on, the theoretically predicted composition was used to synthesize the new DES consisting of 1:2 Choline acetate: Malonic acid, following the standard protocol for DES synthesis as discussed in the experimental section. However, the calculated value of melting point of the DES (331K) and experimental[37] (351K) (obtained from DSC) results showed a close coherence. The deviation of 20K between the real (experimental) and ideal (calculated from phase diagram) eutectic point is the key factor behind the formation of a deep eutectic solvents[38], which results from the extensive hydrogen bonded interaction between the components. Computational study supports the 1:2 molar ratio of complex formation, stability and H-bonding interactions in the DES (fig. 5)

The new DES was characterized experimentally and compared to the commonly used DESs. (Table 3). Further experiments to analyze the radiation stability of the synthesized DES were carried out after irradiating it under gamma source. Finally, the gaseous by-products generated due to irradiation have been quantified.

3.4. Gamma radiolysis of the synthesized DES

The radiation stability of the newly synthesized DES was investigated by irradiating the solvent using Co-60 gamma source at a constant dose of 100kGy. However, the absorbance and FTIR spectra of the samples recorded before and after irradiation does not show any considerable changes indicating no new products are being formed in the liquid medium after irradiation. To identify the gaseous by-products generated after irradiation GC-MS analysis has been conducted. The gaseous radiolytic products obtained in GC-MS along with their yield have been provided in table 4.

Table 4. *The major degradation products detected in gas phase; generated upon radiolysis of Choline acetate: Malonic acid (1:2) DES with 100kGy gamma radiation.*

Gaseous products	H_2	CO	CH_4	CO_2
Radiolytic yield (μmole/J)	0.016	0.016	0.022	0.66

During radiolysis of the compounds a homolytic bond cleavage occurs which can generate several free radicals. These free radicals further combine with each other to form stable molecular products.[41] The most common gaseous products are hydrogen and short chain volatile carbon species. In the new DES since, malonic acid is present in higher concentration (2 moles in each unit); the radiolytic yield of carbon dioxide is comparatively higher. Earlier reports of hydrogen generation on irradiation of ionic liquids by Laverne et al.[42] have shown that ILs containing aromatic moiety give lower $G(H_2)$ than the aliphatic ones containing tertiary or quaternary ammonium entities. However, in this case although quaternary ammonium cation, choline is present yet the $G(H_2)$ value (0.16 molecules/100eV) is less than that reported for ammonium based ILs like $[N_{1114}]$ $[NTf_2]$ (0.73 molecules/100eV). A more detailed analysis of the reason behind this anomaly needs further investigation.

Conclusion:

Radiation sensitivity of a polymorph of choline salt has been investigated and demonstrated that the chain reaction, which resulted in extensive radiolytic damage does not take place in IL containing choline cation [43]. Although solvated electron reacts with choline cation in both choline NTf_2 IL and in reline, however the average lifetime of solvated electron is longer in reline compared to that in Choline NTf_2 IL. This directs towards an enhanced protection from radiolytic damage which is provided most probably by the presence of urea to the DES in reline.

The lowest yield of solvated electron in reline among the three DESs can be attributed firstly, to the highest viscosity, which leads to increased geminate recombination and secondly, to the least number of hydroxyl groups available for solvation process. Existence of pre-solvated electrons in DESs in nanosecond time scale could be verified using nitrate and DNA nucleobase as scavenger. The C_{37} value of nitrate ions is lowest in ethaline [12] among the DESs studied, which hints at the slowest solvation process occurring in ethaline. Scavenging of pre-solvated electron by DNA nucleobase, adenosine is an important aspect and could be conveniently monitored in DES medium at much longer time scale compared to those reported in aqueous solution.

Choline acetate is particularly important for applications in enzyme-based industrial processes [44]. In a study by Hoppe et.al. Choline acetate based DESs exhibited enhanced enzymatic activity. Purification of Kraft cellulose under mild conditions could be achieved by using choline acetate based DESs [45]. Dugoni et.*al*. have demonstrated the efficient applicability of some selected DESs as co-solvent in improving the extraction efficiency of minor actinides wherein particularly choline acetate based DESs showed the best results.[10] In the present study computational analysis based on electronic properties of molecular systems have been applied to select choline acetate and malonic acid as the HBD and HBA pair to form radiation and chemically stable DES. Radiolytic yield of hydrogen shows it to be comparably stable to the aromatic ILs; however, a number of other gaseous by-products like carbon monoxide, methane and carbon dioxide are also generated. Further, comparison of radiation stability of the new DES with other commonly used DESs based on experimental results would establish its efficacy.

Acknowledgement:

The author thanks Dr. A. C. Bhasikuttan, Head, RPCD and Associate Director, Chemistry group and Dr. M. C. Rath, RPCD for their constant support and encouragement. The author also acknowledges all the members associated with RPCD LINAC facility for their help in the e-beam LINAC experiments. The author also expresses sincere gratitude for the support and inspiration received from both current and former colleagues of RPCD.

References:

1. Welton, T. Green Chem. 13 (2011) 225.
2. Flieger, J.; Flieger, M. Int. J. Mol. Sci. (2020) 21.
3. Abbott, A. P.; Capper, G.; Davies, D. L.; Munro, H. L.; Rasheed, R. K.; Tambyrajah, V. ChemComm (2001) 2010.
4. Abbott, A. P.; Capper, G.; Davies, D. L.; Rasheed, R. K.; Tambyrajah, V. ChemComm (2003) 70.
5. Smith, E. L.; Abbott, A. P.; Ryder, K. S. Chem. Rev. 114 (2014) 11060.
6. Li, G.; Yan, C.; Cao, B.; Jiang, J.; Zhao, W.; Wang, J.; Mu, T. Green Chem. 18 (2016) 2522.
7. Yang, W.; Jung, C.; Cha, H. L.; Park, J. W.; Foster, R. I.; Amphlett, J. T. M.; Liu, S.; Bae, S.-E.; Yun, J.-I.; Choi, S. J. Nucl. Mater. 575 (2023) 154229.
8. Patil, S.; Paul, S.; Gupta, R.; Dumpala, R. M.; Goswami, P. G. Sep. Purif. Technol. 318 (2023) 123923.
9. Gamare, J.; Vats, B. G. Eur. J. Inorg. Chem. 26 (2023) e202300441.
10. Colombo Dugoni, G.; Mossini, E.; Macerata, E.; Sacchetti, A.; Mele, A.; Mariani, M. ACS Omega 6 (2021) 3602.
11. Shkrob, I. A.; Marin, T. W.; Chemerisov, S. D.; Wishart, J. F. J. Phys. Chem. B. 115 (2011) 3872.
12. Das, L.; Adhikari, S. J. Phys. Chem. B. 122 (2018) 8900.
13. Das, L.; Mukherjee, S.; Kumar Maity, D.; Adhikari, S. J. Mol. Liq. 360 (2022) 119377.
14. Das, L.; Koonathan, L. D.; Kunwar, A.; Neogy, S.; Debnath, A. K.; Adhikari, S. MATER ADV 2 (2021) 4303.
15. Aihara, J.-i. J. Phys. Chem. A. 103 (1999) 7487.
16. Zhan, C.-G.; Nichols, J. A.; Dixon, D. A. J. Phys. Chem. A. 107 (2003) 4184.
17. Ilawe, N. V.; Fu, J.; Ramanathan, S.; Wong, B. M.; Wu, J. J.

Phys. Chem. C. 120 (2016) 27757.
18. Ma, C.; Guo, Y.; Li, D.; Zong, J.; Ji, X.; Liu, C.; Lu, X. J. Chem. Eng. Data. 61 (2016) 4172.
19. Yadav, A.; Pandey, S. J. Chem. Eng. Data. 59 (2014) 2221.
20. Guha, S. N.; Moorthy, P. N.; Kishore, K.; Naik, D. B.; Rao, K. N. Proceedings of the Indian Academy of Sciences - Chemical Sciences 99 (1987) 261.
21. Upadhyay, J.; Sharma, M. L.; Navathe, C. P.; Toley, M. A.; Shinde, S. J.; Nadkarni, S. A.; Sarkar, S. K. Rev. Sci. Instrum. 83 (2012) 024709.
22. Buxton, G. V.; Stuart, C. R. J. Chem. Soc. Faraday Transactions 91 (1995) 279.
23. Iikura, H.; Tsuneda, T.; Yanai, T.; Hirao, K. J. Chem. Phys. 115 (2001) 3540.
24. Frisch, M. J.; Trucks, G. W.; Schlegel, H. B.; Scuseria, G. E.; Robb, M. A.; Cheeseman, J. R.; Scalmani, G.; Barone, V.; Petersson, G. A.; Nakatsuji, H.; Li, X.; Caricato, M.; Marenich, A. V.; Bloino, J.; Janesko, B. G.; Gomperts, R.; Mennucci, B.; Hratchian, H. P.; Ortiz, J. V.; Izmaylov, A. F.; Sonnenberg, J. L.; Williams; Ding, F.; Lipparini, F.; Egidi, F.; Goings, J.; Peng, B.; Petrone, A.; Henderson, T.; Ranasinghe, D.; Zakrzewski, V. G.; Gao, J.; Rega, N.; Zheng, G.; Liang, W.; Hada, M.; Ehara, M.; Toyota, K.; Fukuda, R.; Hasegawa, J.; Ishida, M.; Nakajima, T.; Honda, Y.; Kitao, O.; Nakai, H.; Vreven, T.; Throssell, K.; Montgomery Jr., J. A.; Peralta, J. E.; Ogliaro, F.; Bearpark, M. J.; Heyd, J. J.; Brothers, E. N.; Kudin, K. N.; Staroverov, V. N.; Keith, T. A.; Kobayashi, R.; Normand, J.; Raghavachari, K.; Rendell, A. P.; Burant, J. C.; Iyengar, S. S.; Tomasi, J.; Cossi, M.; Millam, J. M.; Klene, M.; Adamo, C.; Cammi, R.; Ochterski, J. W.; Martin, R. L.; Morokuma, K.; Farkas, O.; Foresman, J. B.; Fox, D. J. Guassian Inc, Wallingford, CT, 2016.
25. Schaftenaar, G.; Vlieg, E.; Vriend, G. J. Comput. Aided Mol. Des. 31 (2017) 789.
26. Lukas, H.; Fries, S. G.; Sundman, B. Computational Thermodynamics: The Calphad Method; Cambridge University Press, 2007.
27. Kaufman, L.; Bernstein, H. Computer calculation of phase diagrams With special reference to refractory metals; Academic Press Inc: United States, 1970.
28. FactSage In The Integrated Thermodynamic Data Bank System, ; Version 7.2 ed.; GTT Technologies, GmbH: Germany, 1976–2015.
29. Wagle, D. V.; Deakyne, C. A.; Baker, G. A. J. Phys. Chem. B. 120 (2016) 6739.
30. Ashworth, C. R.; Matthews, R. P.; Welton, T.; Hunt, P. A. Phys. Chem. Chem. Phys. 18 (2016) 18145.
31. Hammond, O. S.; Bowron, D. T.; Edler, K. J. Green Chem. 18 (2016) 2736.
32. Jonah, C. D.; Miller, J. R.; Matheson, M. S. J. Phys. Chem. 81 (1977) 1618.
33. Pimblott, S. M.; LaVerne, J. A. J. Phys. Chem. A. 102 (1998) 2967.
34. Wishart, J. F.; Funston, A. M.; Szreder, T.; Cook, A. R.; Gohdo, M. Faraday Discuss. 154 (2012) 353.
35. Nguyen, J.; Ma, Y.; Luo, T.; Bristow, R. G.; Jaffray, D. A.; Lu, Q.-B. Proceedings of the National Academy of Sciences 108 (2011) 11778.
36. Das, L.; Kumar, R.; Maity, D. K.; Adhikari, S.; Dhiman, S. B.; Wishart, J. F. J. Phys. Chem. A. 122 (2018) 3148.
37. Gilmore, M.; Swadzba-Kwasny, M.; Holbrey, J. D. J. Chem. Eng. Data. 64 (2019) 5248.
38. El Achkar, T.; Greige-Gerges, H.; Fourmentin, S. Environ. Chem. Lett. 19 (2021) 3397.
39. García, G.; Aparicio, S.; Ullah, R.; Atilhan, M. Energy Fuels 29 (2015) 2616.
40. Florindo, C.; Oliveira, F. S.; Rebelo, L. P. N.; Fernandes, A. M.; Marrucho, I. M. ACS Sustain. Chem. Eng. 2 (2014) 2416.
41. Morco, R.; Joseph, J.; Wren, J. RSC Adv. 2015.
42. Dhiman, S. B.; Goff, G. S.; Runde, W.; LaVerne, J. A. J. Phys. Chem. B. 117 (2013) 117, 6782.
43. Shkrob, I. A.; Marin, T. W.; Wishart, J. F.; Grills, D. C. J. Phys. Chem. B. 118 (2014) 10477.
44. Hoppe, J.; Drozd, R.; Byzia, E.; Smiglak, M. Int. J. Biol. Macromol. 136 (2019) 296.
45. Colombo Dugoni, G.; Mezzetta, A.; Guazzelli, L.; Chiappe, C.; Ferro, M.; Mele, A. Green Chem. 22 (2020) 8680.

Dr. Laboni Das, *Scientific Officer/F, Radiation and Photochemistry Division, Chemistry Group of BARC, works in the field of Radiation Chemistry. She received her M.Sc. degree in Chemistry in the year 2012, with gold medal from The University of Burdwan. After that she joined Bhabha Atomic Research Centre in 2013, after completion of one year orientation course. She is the receiver of Homi Bhabha gold medal in Chemistry, 56th batch of training school. Dr. Das obtained her PhD in the year 2022, from Homi Bhabha National Institute, Mumbai, India. She pursued her post-doctoral research on "High temperature high pressure Radiation Chemistry" from 2023-2025 in the University of Notre Dame, USA. Her research interests include radiation chemical investigation of novel solvents, radiation chemistry under high temperature high pressure conditions as well as utilizing the novel solvents under radiation conditions to synthesize nanomaterials for societal applications. Apart from her directed research she is also involved in DAE relevant research project.*

Synthesis and Biological Activities of Selenium Functionalized Biopolymers

M. Nayak[1,2], J. Aishwarya[1,2], B.G. Singh[1,2], A. Barik[1,2], A. Kunwar[1,2,*]
[1]*Radiation & Photochemistry Division, Bhabha Atomic Research Centre, Trombay, Mumbai-400085, India*
[2]*Homi Bhabha National Institute, Anushaktinagar, Mumbai –400094, India*
Email – kamit@barc.gov.in

Abstract

Selenium functionalization of bio-polymers has emerged as a novel approach for designing multifunctional therapeutic agents for various health care applications. On a similar approach, our group has recently reported the development of macromolecular therapeutics by covalently conjugating the naturally occurring biopolymers such as albumin and melanin with a pharmacologically relevant diselenide moiety. The detailed biological evaluations of these selenium functionalized biopolymers (seleno-albumin and seleno-melanin) have established their utilities as the anticancer and radio-sensitizing agents. The present article gives the brief account of our recent work on these aspects.

1. Introduction

Macromolecular therapeutics comprises high molecular weight compounds including but not limited to polymeric nanomedicines, polymer-drug conjugates, peptides, proteins, antibodies, polysaccharides and nucleic acids which are engineered for various therapeutic applications [1,2]. It has gained significant attention in recent times for several advantages such as preferable pharmacokinetics, enhanced uptake and lower side effects [1,2]. Biopolymers obtained from natural origin are the most commonly used carriers for developing macromolecular therapeutics. Briefly, a macromolecular therapeutic is designed either by covalently conjugating a predetermined pharmacophore moiety or by entrapping a known drug within the biopolymer of choice [1,2]. Here, the choices of pharmacophore moiety and the biopolymer are an important criterion in order to achieve the multifunctionality of the therapeutic system. Organo-selenium compounds have recently been established as the therapeutically relevant class of molecules with wide ranging pharmacological applications such as antioxidant, anticancer, radio-modulatory and anti-inflammatory among others [3]. The pharmacological activities of organo-selenium compounds are primarily attributed to their redox activities leading to alteration in the cellular redox status (GSH/GSSG, NAD/NADH and NADP/NADPH) [4]. Among the various chemical forms, organodiselenide (R-Se-Se-R) form is considered to be highly redox active. For instance, they can undergo reduction either by acting as the substrate of intracellular redox enzymes such as thioredoxin reductase (TrxR), glutathione reductase (GR), and glutathione S-transferase (GST) or by directly reacting with cellular glutathione (GSH) to form selenenyl sulphide (R-Se-S-G) or selone (R-Se=C) [3,4]. The reduced species in turn can catalyse the reduction of hydrogen peroxide into water molecules by a glutathione peroxidase (GPx)-like catalytic mechanism. On the contrary, organodiselenides can also exhibit pro-oxidant activity or take part in ROS generation by oxidizing cellular GSH in futile cycle or by inhibiting thiol containing redox enzymes like GR, TrxR and GST through covalent modifications [3,4]. Moreover, organodiselenides are also reported to induce proteotoxic or endoplasmic reticulum (ER) stress by disrupting the folding of cysteine proteins [5]. Together, these paradoxical behaviours of diselenides make them excellent pharmacophore moieties for the design of next generation therapeutics. Accordingly, the -Se-Se- functionalized biomaterials are expected to be more efficient therapeutic system. In this context, our group hypothesized to synthesize the synthesize -Se-Se- functionalized derivative of bovine serum albumin

(BSA, transport protein) and melanin (a polymeric pigment responsible black/red pigmentation of skin and hair in human) for anticancer applications [1,6]. The rational of choosing above biopolymers was their well-established usage as excipients for several pharmaceutical grade formulations, less immunogenicity and biodegradability [1,6].

2. Methods

All chemicals with maximum available purity were employed in the study. The synthesis of selenium functionalized BSA and melanin were carried out as given in our previous reports [1,6]. The purity of newly synthesized selenium derivatives of BSA were checked by various spectroscopic techniques (such as FTIR, XPS, Raman, HPLC, MALDI-TOF-MS, SDS-PAGE and AAS. The purified derivatives of BSA and melanin were evaluated in detail for their pharmacological (anticancer and radio-sensitization) activities employing the cellular models and standard assays.

3. Results & Discussion

3.1 Anticancer effect of selenium functionalized BSA against lung cancer

The albumin protein was chosen as the host molecule for selenium functionalization as it is the most abundantly present transport protein in the mammals [7]. Serum albumins being circulatory protein may offer advantage as therapeutic systems as they are well documented for prolong circulation half-lives and for acting as the natural carriers of drug molecules [7]. Additionally, few reports also suggest that the tumor cells show higher uptake for serum albumin as compared to noncancerous cells due to the presence of albumin specific receptors such as FcRn, gp60, gp18, megalin, cubilin, SPARC, and CD36 on their plasma membrane [7]. These features may allow the selective toxicity of serum albumin-based therapeutic systems towards cancer cells. Among the serum albumins, BSA is cost effective and shares high level of sequence homology with human serum albumin (HSA) [7]. Moreover, all the optimisation with BSA can easily be translated to an HSA-based system [7]. Accordingly, BSA is widely used as a model of serum albumin. On the other hand, selenium in the chemical form of 3-3'-diselenodipropionic acid (DSePA) was used as a pharmacophore moiety considering that DSePA having carboxylic (COOH) group can be conjugated to free amine (NH_2) functional group through amide linkage by using well-known carbodiimide coupling chemistry. Additionally, DSePA *per se* is well reported for various therapeutic activities including antioxidant, radioprotection and anticancer [5]. Briefly, the conjugation of DSePA with BSA was performed by EDC/sulfo-NHS coupling method as shown in the scheme of figure 1A. Previous studies have established that the primary amine of lysine residue is the most preferred site for carbodiimide coupling [8]. Therefore, the yield of conjugation depends on the availability of the primary amine of lysine residue in the host protein. Importantly, BSA contains a total of 59 lysine residues of which 30-35 have primary amines [9]. In order to allow all the ligable lysine residues of BSA available for conjugation, it needs to be completely denatured but this may also favour aggregation or the cross-linking during the conjugation reaction. Therefore, to evade the aggregation or cross-linking of modified BSA, the reaction conditions were optimised in such a way that the native structure of BSA was minimally disturbed. For instance, the reaction was carried out in aqueous buffered medium instead of organic solvents by fixing BSA concentration at 10 mg/ml. Other parameters such as the ratio metric concentrations of DSePA, EDC and sulfo-NHS and reaction time were chosen based on previous optimisation by our group [8]. It is also worth mentioning here that EDS/sulfo-NHS activation of a carboxylic group requires an acidic medium which can induce denaturation of BSA. Accordingly, to overcome this issue, DSePA was initially activated with EDC/sulfo-NHS at acidic pH (~ 6) in pure water followed by addition of buffered BSA solution to the activated DSePA solution to facilitate the coupling reaction at physiological pH (~7.4).

By following these reaction conditions, a series of batches (n = 5) of Se-Se-BSA was prepared. Each batch was checked for the purity, protein recovery and selenium content in order to validate the reproducibility of the conjugation reaction. The various spectroscopic characterizations (FTIR, Raman, XPS, HPLC and AAS) of the purified product from

Table 1: Biophysical parameters of Se-Se-BSA versus native BSA

Sample	Hydrodynamic size (nm)	Isoelectric point (pH)	Secondary structure
Native BSA	~8 nm	~ 4.4	α-Helix – 39.1%, β-Sheet – 14.2%, β-Turn – 15.8%, and Random coil – 31.4%
Se-Se-BSA	~11 nm	~ 4.7	α-Helix – 26.9%, β-Sheet – 17.7%, β-Turn – 17.8%, and Random coil – 38.3%

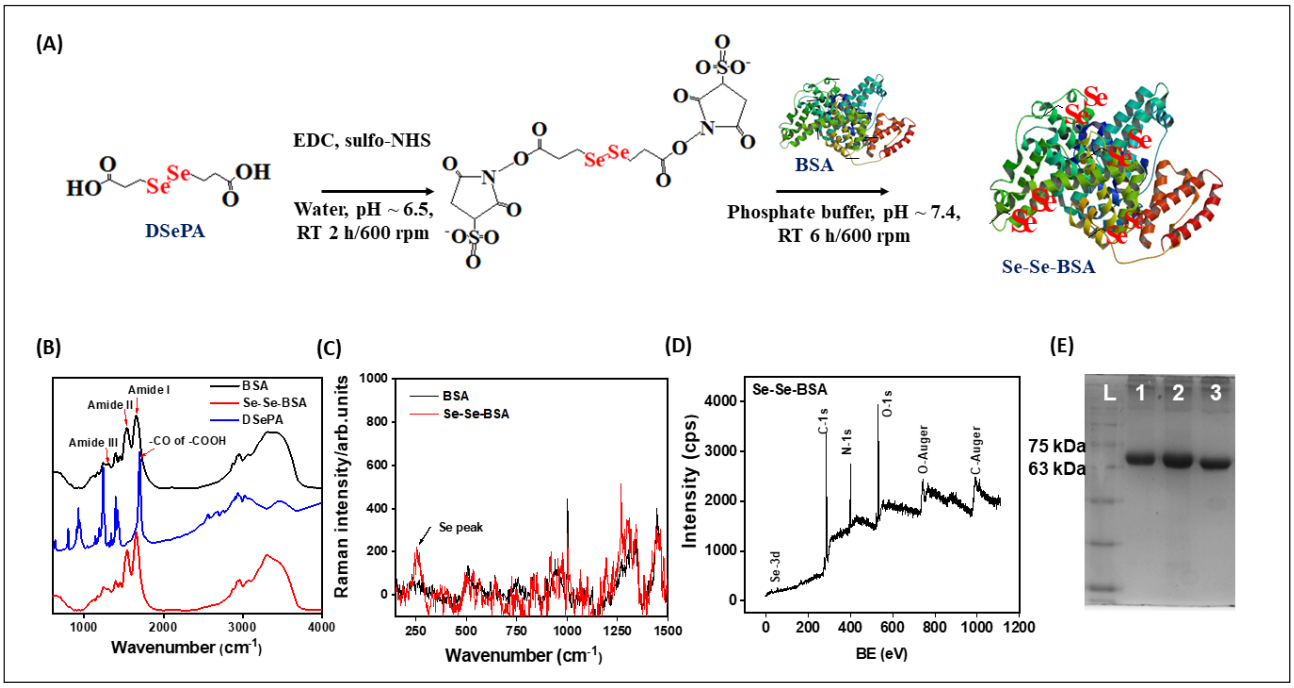

Figure 1. *(A) Schematic shows steps involved in the synthesis of Se-Se-BSA. (B) SDS-PAGE (12%) of neat BSA and Se-Se-BSA of representative batches: L- Molecular ladder, Lane 1 - 2 µg of Se-Se-BSA (Batch 1), Lane 2 - 4 µg of Se-Se-BSA (Batch 2), Lane 3 – 2 µg of neat BSA. (B) IR spectra of neat BSA, neat DSePA and freshly synthesized Se-Se-BSA (C) Raman spectra of neat BSA and freshly synthesized Se-Se-BSA (D) XPS survey-scan spectrum showing photo peaks of C 1s, O 1s, N 1s, and Se 3d in freshly synthesized Se-Se-BSA.*

successive batches (n = 5) confirmed the conjugation of DSePA with BSA (Fig. 1B-E). Bradford assay indicated recovery of 93.0 ± 3.2 % of protein (with respect to the amount of protein taken as the starting material) content in the final product. The average selenium content of the final product estimated from AAS was 12.8 ± 2.0 µg/mg of protein. Since DSePA has two carboxylic groups, it can be argued that a single molecule of DSePA may engage two BSA monomers resulting in the crosslinking or the aggregation of BSA monomer. However, the MALDI-TOF-MS along with SDS-PAGE confirmed that Se-Se-BSA was in monomeric form and about ~5 molecules of DSePA were attached to per BSA monomer. The plausible explanation for DSePA engaging just one BSA molecule could be the steric hindrance between the considerably bulkier BSA molecules as compared to DSePA. Notably, with regard to accessibility, the BSA monomer has the three most accessible (surface exposed) and five easily accessible lysine residues with primary amine group [9]. Therefore, from the above stoichiometry, it could be inferred that the conjugation of DSePA to BSA was restricted mostly to the surface and easily accessible lysine residues.

Further, biophysical characterisation of the Se-Se-BSA indicated that conjugation of DSePA led to a nominal alteration with respect to hydrodynamic radius, isoelectric point (IEP) and secondary structures as compared to native BSA (Table - 1).

These observations further supported the assumption that conjugation of DSePA did not involve the buried lysine residues of BSA. In other words, if conjugation would have happened to buried lysine residues of BSA, it would have led to the extensive change in the secondary structure of the protein. After completing the synthesis and characterisation of Se-Se-BSA, it was used for studying biological activity. The cytotoxic effect of Se-Se-BSA was evaluated in a panel of cancerous (A549, LN229 and MCF7) and noncancerous (WI38 and WI26) cell types by MTT assay. Briefly, the cells were treated with increasing concentrations (0.1 - 5 mg/ml of protein equivalent containing 1.2 - 64 µg/ml of selenium equivalent) of Se-Se-BSA for 48 h prior to MTT assay. The viability -concentration plot was used to determine the half maximal inhibitory concentration (IC_{50}) of Se-Se-BSA for inhibiting the proliferation of above cell types by 50%. The IC_{50} values estimated for antiproliferative activity of Se-Se-BSA in A549, LN229, MCF7, WI26 and WI38 cell lines were 1.8 ± 0.5 mg/ml, 1.3 ± 0.1 mg/ml, 2.5 ± 0.5 mg/ml, 5.2 ± 0.5 mg/ml and 6.8 ± 0.3 mg/ml respectively with respect to protein equivalent and 24.1 ± 6.4 µg/ml, 16.5 ± 1.9 µg/ml, 32.7 ± 6.9 µg/ml, 66.4 ± 6.7 µg/ml and 87.7 ± 4.5 µg/ml respectively with respect to selenium equivalent. This clearly suggested that Se-Se-BSA exhibited selective toxicity towards cancerous cell types. Notably, the native BSA at equivalent protein concentrations did not cause any toxicity in above cell types. This confirmed that the anticancer activity of BSA was due to functionalization

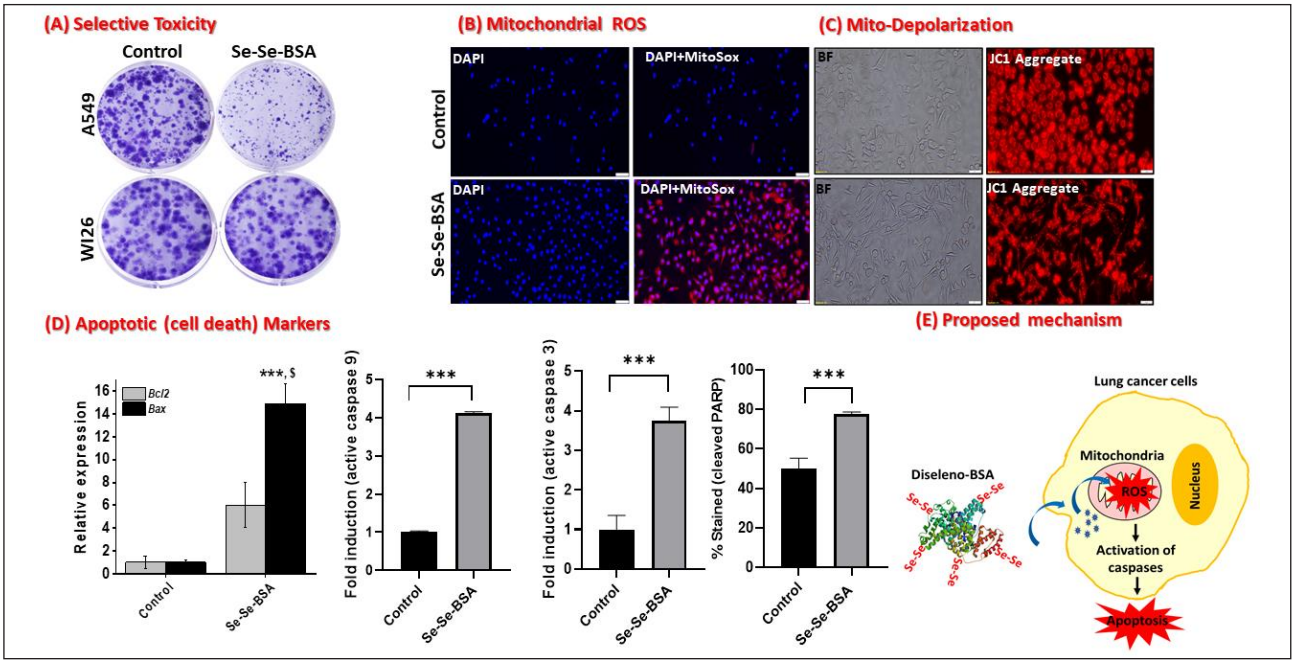

Figure 2. *Anticancer activity of Se-Se-BSA (1.5 mg/ml protein equivalent containing 20 µg/ml of selenium equivalent) in lung cancer (A549) cells: (A) Photographs show the effect of Se-Se-BSA on the viability of A549 and WI26 cell lines by clonogenic assay. (B) Representative images of A549 cells show the effect of Se-Se-BSA on the mitochondrial ROS generation in terms of mito-SOX fluorescence. The cells were counterstained with the nucleus localizing dye, DAPI. 20x Magnification. (C) Representative images of A549 cells show the effect of Se-Se-BSA on the mitochondrial integrity in terms JC1 fluorescence. 20x Magnification. (D) Plots shows the relative mRNA expressions of Bcl-2 and Bax after treatment with Se-Se-BSA with respect to the control group by RT-PCR. The β-actin expression was used as an internal control. Other plots under this panel correspond to the fold induction of the activities of cleaved caspase 9, cleaved caspase 3 and cleaved PARP in A549 cells after treatment with Se-Se-BSA. (E) Proposed mechanism of action of Se-Se-BSA in A549 lung cancer cells. ***P<0.005 as compared to control group. $P<0.05 as compared to Bcl-2 of Se-Se-BSA group.*

with selenium. To further validate the selective toxicity of Se-Se-BSA, its long-term toxicity in A549 versus WI26 cells was studied by clonogenic assay (Fig. 2A). Briefly, A549 and WI26 cells were treated with increasing concentrations of Se-Se-BSA (0.05 – 0.5 mg/ml of protein equivalent containing 0.06 – 0.6 µg/ml of selenium equivalent) for 14 days, allowed to form the microscopic colonies and analyzed by crystal violet staining. The result showed that the treatment of Se-Se-BSA led to a concentration dependent decrease in the size as well as number of colonies of both A549 and WI26 cells. By plotting the survival fraction as a function of the treatment concentrations, the D_{50} dosages (concentration required to reduce the survival fraction by 50%) of Se-Se-BSA for A549 and WI26 cells were estimated as 0.072 ± 0.007 mg/ml and 0.14 ± 0.01 mg/ml respectively with respect to protein equivalent and 0.89 ± 0.07 µg/ml and 1.79 ± 0.10 µg/ml respectively with respect to selenium equivalent. Thus, the above results together corroborated the selective toxicity of Se-Se-BSA in A549 cells as compared to WI26 cells.

Further, to characterize the type of cell death, A549 cells were treated with Se-Se-BSA (1.5 and 2 mg/ml of protein equivalent containing 20 and 25 µg/ml of selenium equivalent) for varying time points (24 h and 48 h) and analyzed by Annexin V-PI assay. The treatment of Se-Se-BSA showed the concentration and time dependent significant increase of the percent count of primary (Annexin $V^{+ve}PI^{-ve}$) and secondary (Annexin $V^{+ve}PI^{+ve}$) apoptotic cells as compared to the control group. On the other hand, treatment of Se-Se-BSA did not cause any significant change of the percent count of necrotic (Annexin V^{-ve} PI^{+ve}) cells as compared to the control group. Together, these results suggested that Se-Se-BSA primarily induced apoptosis in A549 cells. Further, diselenide moiety is well documented for redox modulation [3-5]. Anticipating a similar mechanism, the effect of Se-Se-BSA (1.5 mg/ml protein equivalent containing 20 µg/ml of selenium equivalent) on the overall cellular and mitochondrial ROS levels was evaluated in A549 cells by measuring the fluorescence intensities of the oxidized DCFDA and mito-SOX respectively through fluorescence microscopy. The results indicated that the cells treated with Se-Se-BSA did not show any significant change in the fluorescence intensity of DCF as compared to the healthy control group. On the other hand, treatment of Se-Se-BSA led to a significant increase in the fluorescence intensity of mito-SOX (Fig. 2B). The mitochondrial ROS generation may compromise the integrity of mitochondrial membrane followed by loss of mitochondrial membrane potential (MMP). Therefore, to corroborate the observations of mito-SOX-based fluorescence measurement, the effect of Se-Se-BSA treatment on the MMP was also evaluated by staining the cells with JC1 and monitoring the emissions at desired wavelengths by fluorescence microscope. Notably, the cells treated with Se-Se-BSA showed significant reduction in the red emission as compared to control cells confirming the loss of MMP (Fig. 2C). It is well known that mitochondrial depolarization is regulated by the ratio of the expressions of *Bax* (pro-apoptotic) and *Bcl-2* (anti-apoptotic) genes [10]. Accordingly, the effect of the treatment of Se-Se-BSA on the expressions of above genes were examined by RT-PCR. The results indicated that the treatment of Se-Se-BSA led to a significant increase in the expression of *Bax* by 14.9 ± 1.7 folds while marginally increasing the expression of *Bcl-2* by 6.0 ± 1.9 folds (Fig. 2D). The significantly higher increase in the expression of *Bax* as compared to *Bcl-2* is in agreement with the loss of MMP as observed through JC1 assay. Further, the loss of MMP is followed by apoptosis through the involvement of terminal effectors like caspase 9, caspase 3 and PARP [10]. Therefore, the effect of the treatment of Se-Se-BSA (1.5 mg/ml protein equivalent containing 20 µg/ml of selenium equivalent) on the expressions of active caspase 9, active caspase 3 and cleaved PARP were evaluated through flow cytometry at 48 h post treatment (Fig. 2D). The results indicated that treatment of Se-Se-BSA led to significant inductions of the activities of caspase 9 and caspase 3 and of the level of cleaved PARP as compared to the control group thus confirming the execution of apoptosis. Finally, in order to know whether mitochondrial ROS was indeed the trigger for Se-Se-BSA induced cell death or apoptosis, the cells were preincubated with mito-TEMPO (5 µM, mitochondrial ROS scavenger) followed by treatment with Se-Se-BSA and the analysis of sub-G1 phase by PI assay at 48 h post treatment.

As per the cell cycle distribution, the pre-treatment of mito-TEMPO significantly abrogated the Se-Se-BSA induced cell death. This confirmed the role of mitochondrial ROS as one of the triggers for the anticancer effect of Se-Se-BSA in A549 cells. Together, the above studies established the efficacy of Se-Se-BSA as an anticancer agent through redox modulation as shown in scheme E of figure 2.

3.2 Radio-sensitizing effect of selenium functionalized melanin against lung cancer

In another study, melanin was chosen as the host molecule for selenium functionalization. Melanin is a heterogenous polymeric pigment present in all domains of life, including bacteria, fungi, plants, animals and humans [11]. Melanin is synthesized from an amino acid precursor called tyrosine [11]. Briefly, tyrosine undergoes hydroxylation to form L-DOPA, which then oxidizes and polymerizes to form melanin. Over the years, it has been established that melanin and its derivatives can protect cells from high-energy ionizing radiation-induced toxicity [12,13]. Very recently, Cao et al provided evidence for the biological existence of selenomelanin [14]. The group also showed that selenomelanin was more effective than other derivatives of melanin in protecting healthy (NHEK) cells from radiation-induced toxicity [14]. While radioprotection is the novel function exerted by melanin and its derivatives, the same may compromise the efficacy of radiotherapy (a major treatment modality) in tumor cells. This becomes even more concerning, considering that melanoma cells endogenously synthesize melanin and are known to be radioresistant [15]. Therefore, there is a need to study the radio-modulatory activity of melanin in cancerous cells. However, to the best of our knowledge, there is no such study available on selenomelanin. Accordingly, the objective of the present study was to investigate the radio-modulatory activity of chemically synthesized selenomelanin in cancerous cells. In order to avoid the contribution of endogenously synthesized melanin, the study was

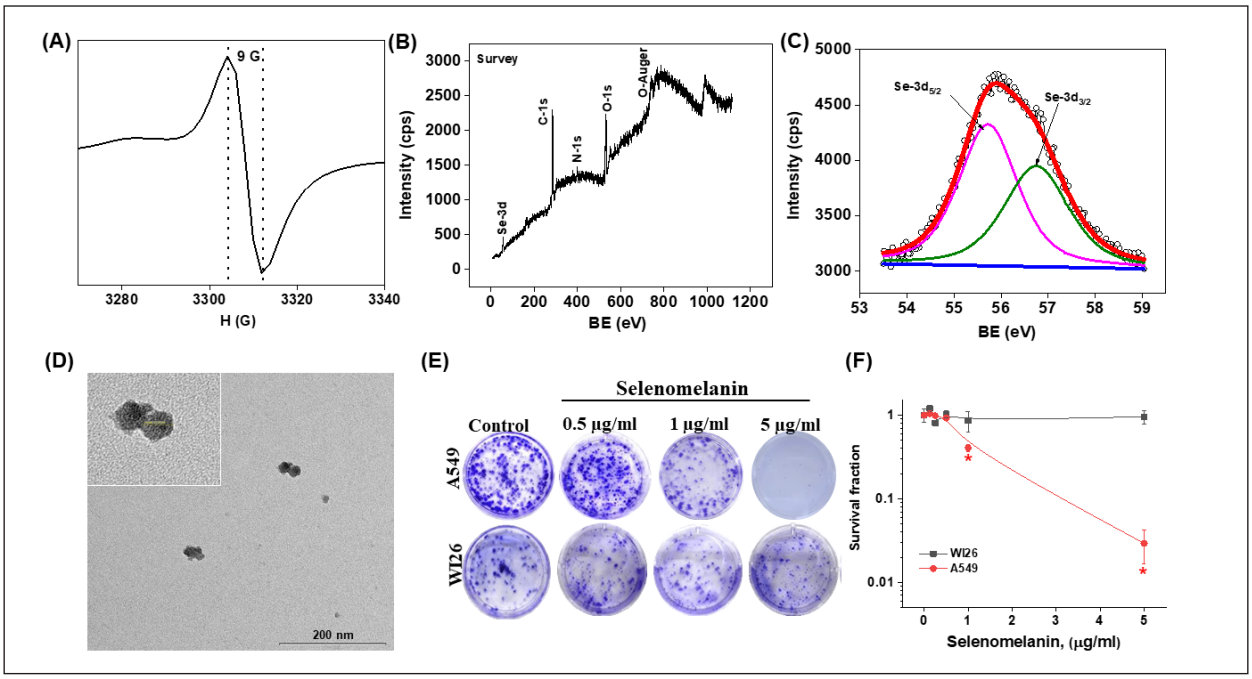

Figure 3. *(A) EPR spectrum of selenomelanin. (B) XPS survey-scan spectrum showing photo peaks of C 1s, N 1s, O 1s and Se 3d in selenomelanin. (C) High-resolution XPS spectra of Se 3d in selenomelanin. (D) TEM image of selenomelanin. The inset shows zoomed in pictures of the region of interest. (E) Representative photographs show the effect of selenomelanin on the clonogenic potential of A549 and WI26 cell lines by clonogenic assay. About ~500 and ~1000 cells were seeded for A549 and WI26 cell types, respectively, for the above experiment. (F) Survival curve of A549 and WI26 cells upon treatment with increasing concentrations (0.125 – 5 µg/ml) of selenomelanin by clonogenic assay. The results are presented as mean ± SEM (n = 3). *p<0.05 as compared to control by t-test.*

carried out in lung carcinoma (A549) cells, which do not synthesize melanin. Briefly, selenomelanin was synthesized by following the recently reported methodology which deals with the oxidation of 3,4-dihydroxy phenylalanine in the presence of the selenocystine [14]. The most important characteristic of melanin is its radical (unpaired electrons) nature [14]. Therefore, the *as-synthesized* reaction product was characterized through EPR spectroscopy to probe the presence of unpaired electrons. The EPR spectrum, as shown in figure 3A indeed confirmed the presence of unpaired electrons in the reaction product.

For instance, the number of unpaired electrons in the reaction product was calculated as 2.12×10^{18} spin/g. Subsequently, the reaction product was characterized by XPS and AAS to probe the presence of selenium. Notably, the XPS survey spectrum of the reaction product showed the characteristic peaks corresponding to $3d_{5/2}$ and $3d_{3/2}$ energy levels of selenium at 55.7 eV and 56.7 eV, respectively (Fig. 3B & 3C). Similarly, selenium content estimated through AAS was 5.78 ± 0.25 µg/mg of the reaction product. Together, these characterizations confirmed the formation of selenomelanin. Further, Cao et al have previously reported that synthetic selenomelanin exhibits the nanoparticulate nature [14]. Accordingly, the *as-synthesized* selenomelanin was suspended in water (pH ~ 7) and characterized for absolute size by TEM and for colloidal properties such as hydrodynamic size and surface charge by DLS and zeta sizer, respectively. These studies indeed confirmed the near spherical nanoparticulate nature of selenomelanin with the absolute size, average hydrodynamic size and surface charge of 15.1 ± 3.6 nm, 201.0 ± 3.6 (PI = 0.21) nm and -20.5 ± 0.4 mV, respectively (Fig. 3D). The fully characterized selenomelanin was subsequently used for biological studies. The cytotoxicity evaluation of selenomelanin (72 h treatment with 5-50 µg/ml) in A549 cells by MTT assay indicated that it did not affect the cell viability up to a concentration of 15 µg/ml followed by a concentration-dependant toxicity with the half maximal inhibitory concentration (IC_{50}) of 72.03 ± 7.13 **µg/ml**. Subsequently, the long term (14 days of incubation) toxicity of selenomelanin in A549 cells was examined by clonogenic assay. Notably, the considerably lower concentration range (0.125 – 5.0 µg/ml) of selenomelanin was chosen for clonogenic assay as this assay provides the cumulative toxicity of the test compound accumulated over a period of incubation through various death mechanisms. The results of the clonogenic assay revealed that the treatment of selenomelanin up to a concentration of 0.5 µg/ml did not cause any significant reduction in the number and size of colonies (Fig. 2E and 2F). Whereas treatment of selenomelanin at concentrations > 0.5 µg/ml showed a concentration dependant decrease in the number and size of colonies (Fig. 2E and 2F). The concentration of selenomelanin needed to reduce the survival fraction of A549 cells by 50% or D_{50} dosage estimated from the clonogenic assay was 0.85 ± 0.16 µg/ml. Further, to know whether selenomelanin-mediated toxicity was specific to A549 cells, its toxicity was also examined in normal epithelial derived fibroblast cell line (WI26-VA4) of lung origin by MTT and clonogenic assays. The results of the MTT assay (72 h incubation with 5-50 µg/ml of selenomelanin) in WI26 cells showed a similar toxicity pattern as that seen in A549 cells with IC_{50} value of 81.56 ± 1.63 **µg/ml**. On the contrary, the results of the clonogenic assay (14 days incubation with 0.125 - 5.0 µg/ml) indicated the differential toxicity of selenomelanin in WI26 versus A549 cells with D_{50} value of > 5 µg/ml (Fig. 2E and 2F). Thus, the long-term treatment with low concentration (0. 5 to 5 µg/ml) of selenomelanin can selectively kill A549 cancerous cells without affecting the viability of normal WI26 cells. The above results also concur with previous reports that indicate melanin *per se*, depending on its chemical composition, may be potentially damaging to cells [16]. For instance, red hair melanin (pheomelanin) is shown to induce lysis of Ehrlich ascites tumor cells [16]. The clonogenic assay is the gold standard method for examining the radiation response of cellular systems [17]. Thus, a clonogenic assay was employed to examine the radiation response of selenomalanin in A549 cells. Briefly, cells pre-treated with 0.125 to 1.0 µg/ml of selenomelanin (non-toxic concentration range for normal, noncancerous cells) were exposed to a fixed dose of γ-radiation (4 Gy) and then analysed for survival fraction by clonogenic assay (Fig. 4A). As expected, exposure to radiation (4 Gy) led to a significant decrease in the survival fraction (marked by a reduction in size as well as number of

colonies) as compared to the sham control group (Fig. 4A). The pre-treatment of selenomelanin showed the concentration dependant enhancement in the radiation toxicity. For instance, the combined (selenomelanin + radiation) treatment groups comprising 0.25 to 1.0 µg/ml of selenomelanin showed a significantly lower survival fraction as compared to the radiation (4 Gy) control group (Fig. 4A). In another experiment, cells pre-treated with a fixed concentration (0.25 µg/ml, minimum effective dose observed from the above dose escalation study) of selenomelanin were exposed to varying doses (2 Gy, 6 Gy and 7 Gy) of γ-radiation and analyzed for survival fraction by clonogenic assay. As expected, the exposure to γ-radiation led to a dose-dependent decrease in the survival fraction as compared to sham control. The pre-treatment of selenomelanin showed augmentation of radiation toxicity at all absorbed doses (2 Gy, 6 Gy and 7 Gy). However, the radio-sensitization effects of combined treatment groups were significant only at higher absorbed doses (> 2 Gy). On contrary to the above observations, the pre-treatment of selenomelanin up to a concentration of 0.5 µg/ml did not show any significant modulation of the radiation (4 Gy)-induced toxicity in WI26 cells by clonogenic assay. Whereas the subsequent higher concentration of 1.0 µg/ml showed an increase in radiation-induced toxicity even in the WI26 cells. Thus, the above studies together suggested that selenomelanin, depending on the concentration range, specifically radio-sensitized A549 cells of cancerous origins. The radio-sensitizing effect of selenomelanin could be due to its ability to enhance the radiation-induced acute changes comprising of ROS generation, DNA damage and cell death [18]. In order

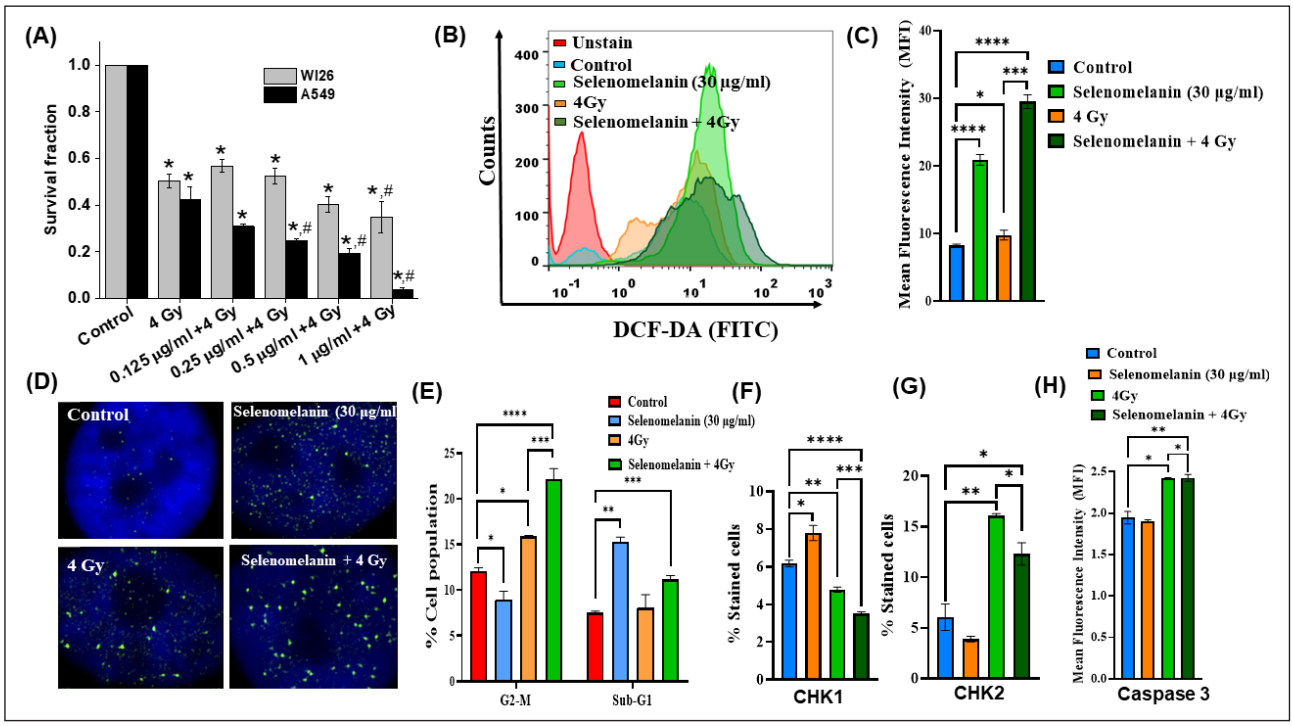

Figure 4. *Radio-sensitizing activity of selenomelanin in lung cancer (A549) cells. (A) The plot shows the effect of the sequential treatments of selenomelanin (0.125 – 1 µg/ml) and γ-radiation (4 Gy) on the survival fraction of A549 and WI26 cells by clonogenic assay. The results are presented as mean ± SEM (n = 3). (B) Representative histograms show the fluorescence intensity distribution of DCF-DA-stained cells of the various experimental groups by flow cytometry. (C) The plots show the mean fluorescence intensity of DCF under various experimental groups by flow cytometry. (D) Representative images show the γ-H2AX foci (marker of DNA damage) in the DAPI-stained nucleus of the various treatment groups by immunofluorescence. (E) The plot shows the effect of the above treatment on the percentage of cells in the G2/M and sub-G1 phases of the cell cycle by PI staining followed by flow cytometry. (F-H) The plots show the expression levels of phospho-CHK1, phospo-CHK2 and cleaved caspase 3 respectively by flow cytometry. The results are presented as mean ± SEM (n = 3). *p<0.05, **p<0.01, ***p<0.001, ****p<0.0001 by t-test.*

to address these issues, the mechanistic investigations were carried out in A549 cells by employing the combinatorial treatment of selenomelanin at a fixed concentration of 30 µg/ml and γ-radiation at a fixed absorbed dose of 4 Gy. These studies revealed that selenomelanin *per se,* as well as in combination with radiation, led to significantly higher ROS generation as compared to the control group by DCF-DA assay (Fig. 4B and 4C). Previously, several reports have shown that melanin-rich in unpaired electrons can produce ROS like superoxide radicals and hydrogen peroxide under an aerobic environment [16]. Similarly, selenium moiety, depending on its chemical surroundings is also known to contribute to ROS (superoxide radical and hydrogen peroxide) production under aerobic environment [19]. Thus, selenomelanin-mediated ROS generation is assumed to be due to its interaction with the aerobic and redox environment of cells. Subsequent studies indicated that selenomelamin *per se* caused DNA damage and also augmented radiation-induced DNA damage through additive effects (Fig. 4D). Ionizing radiation mostly produces double strand breaks (DSBs) and single strand breaks (SSBs), which are recognized by DNA damage-sensing proteins like ATM/ATR, followed by activation or phosphorylation of downstream signalling proteins comprising p53, CHK1 and CHK2 [20].

The phosphorylated forms of these proteins further regulate the expression of cyclin proteins, DNA repair proteins, cyclin dependant kinase inhibitors and phosphatases involved in the cell cycle progression to facilitate cell cycle arrest at G1/S and G2/M checkpoints in order to allow the repair of damaged DNA [20]. However, in case of irreparable DNA damage, the above proteins can trigger apoptosis by activating the caspase cascade [20]. The flow cytometry-based analysis of cell cycle progression and expression profiling of phospho-p53, phospho-CHK1, phospho-CHK2 and cleaved caspase 3 at 48 h post-irradiation indicated that radiation did not alter the level of phospho-p53 at the investigated time point while upregulating and downregulating the phospho-CHK2 and phospho-CHK1 respectively as compared to sham control (Fig. 4E-H). Simultaneously, the radiation control group also exhibited G2/M arrest and an increase in the expression of cleaved caspase 3 as compared to the sham control group (Fig. 4E-H). The radiation-induced manifestation of G2/M arrest accompanied with an increase of phospho-CHK2 and cleaved caspase 3 is attributed to the accumulation of irreparable DSBs, as indicated in previous reports [20]. Notably, combinatorial (selenomelanin + radiation) treatment showed significant augmentation of G2/M arrest accompanied with significant downregulation of CHK1 and CHK2 and a marginal increase of cleaved caspase-3 and sub-G1 count as compared to the radiation control group. The augmented G2/M arrest in the combinatorial group is attributed to the higher DNA damage as compared to the radiation control group. Further, a recent study has shown that the downregulation of CHK1 and CHK2 favours radiation-induced apoptosis by forcing the irradiated cells to undergo division with the damaged DNA [21]. Accordingly, it is inferred that selenomelanin-mediated downregulation of phospho-CHK1 and phospho-CHK2 in the irradiated cells favoured the cell death through apoptosis. Interestingly, selenomelanin *per se,* despite causing ROS generation and DNA damage, did not show any significant alteration in the expressions of phospho-p53, phospho-CHK2 and cleaved caspase 3. On the other hand, selenomelanin *per se* showed a marginal increase in the expression of phospho-CHK1. The activation of CHK1 is generally linked to SSBs [22]. Thus, it is inferred that

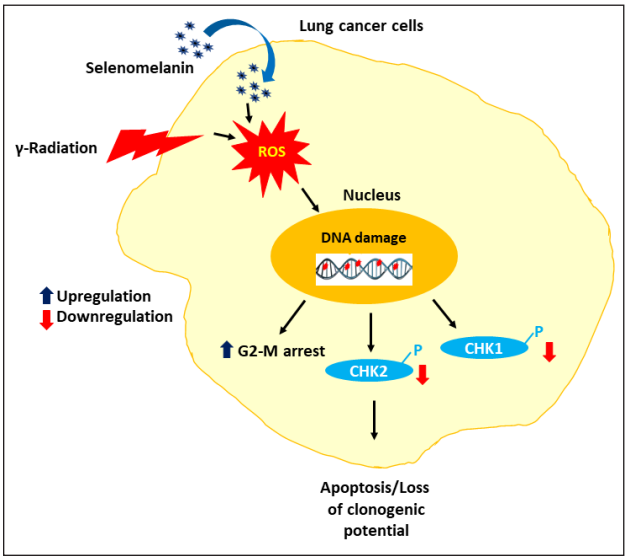

Figure 5. *Schematic depicts the mechanism of radio-sensitization by selenomelanin in A549 cells*

selenomelanin *per se* probably induced SSBs, and since SSBs are mostly reparable types of DNA damage, it did not induce apoptosis or toxicity. Together, the overall investigation confirmed that selenomelanin radio-sensitized A549 cells by augmenting G2/M and downregulating phospho-CHK1 and phospho-CHK2 as shown in the figure 5.

4. Conclusions

In conclusion, our studies report the synthesis and characterisation of novel selenium derivatives of BSA and melanin. The cellular studies provided the proof of the concept of the therapeutic utility of Se-Se-BSA as an anticancer agent and selenomelanin as the radio-sensitizing agent. The future studies will be focused on pharmacokinetic, biodistribution, *in vivo* efficacy evaluation and to delineate the molecular mechanisms responsible for the redox modulatory effects of Se-Se-BSA and selenomelanin.

5. Acknowledgements

The research work presented in the manuscript is a part of doctoral thesis to be submitted by Ms. Minati Nayak to Homi Bhabha National Institute. We acknowledge all the co-authors and collaborators of our published papers cited in the references. We thank Dr. A.C. Bhasikuttan, Head, RPCD and Associate Director, Chemistry group, BARC, India, for encouragement and support.

6. References

1. Nayak M, Das RP, Kumbhare LB, Singh BG, Iwaoka M, Kunwar A. Int J Biol Macromol. 2024;279(Pt 2):135141
2. M. Rütter, N. Milošević, A. David, J Control Release 330 (2021) 1191–1207.
3. V. Gandin, P. Khalkar, J. Braude, A.P. Fernandes, Free Radic Biol Med 127 (2018) 80–97.
4. M. Álvarez-Pérez, W. Ali, M.A. Marć, J. Handzlik, E. Domínguez-Álvarez, Molecules 23 (2018) 628.
5. V.V. Gandhi, K.A. Gandhi, L.B. Kumbhare, J.S. Goda, V. Gota, K.I. Priyadarsini, A. Kunwar, Free Radic Biol Med 175 (2021) 1–17.
6. Aishwarya J, Das RP, Barik A, Kunwar A, Colloids Surf B Biointerfaces. 252 (2025)114680.
7. E.N. Hoogenboezem, C.L. Duvall, Adv Drug Deliv Rev 130 (2018) 73–89.
8. R.P. Das, B.G. Singh, J. Aishwarya, L.B. Kumbhare, A. Kunwar, Biomater. Sci. 11 (2023) 1437–1450.
9. C.M. Anthony-Regnitz, A.E. Wilson, K.L. Sweazea, E.J. Braun, J Mol Evol 88 (2020) 653–661.
10. C. Wang, R.J. Youle, Annu Rev Genet 43 (2009) 95–118.
11. Guo L, Li W, Gu Z, Wang L, Guo L, Ma S, et al. Int J Mol Sci. 2023;24(5):4360.
12. Kunwar A, Adhikary B, Jayakumar S, Barik A, Chattopadhyay S, Raghukumar S, et al. Toxicol Appl Pharmacol. 2012;264(2):202–11.
13. Dadachova E, Casadevall A. Curr Opin Microbiol. 2008;11(6):525–31.
14. Cao W, McCallum NC, Ni QZ, Li W, Boyce H, Mao H, et al. J Am Chem Soc. 2020;142(29):12802–10.
15. Krayem M, Ghanem GE, Van Gestel D. Curr Opin Oncol. 2022;34(2):131–8.
16. Menon IA, Persad S, Ranadive NS, Haberman HF. Can J Biochem Cell Biol. 1985;63(4):278–83.
17. Raghuraman M, Verma P, Kunwar A, Phadnis PP, Jain VK, Priyadarsini KI. Met Integr Biometal Sci. 2017;9(6):715–25.
18. Ashwell S, Zabludoff S. Clin Cancer Res. 2008;14(13):4032-7.
19. Yan L, Spallholz JE. Biochem Pharmacol. 1993;45(2):429–37.
20. Azzam EI, Jay-Gerin JP, Pain D. Cancer Lett. 2012;327(1–2):48–60.
21. Gao QL, Ye F, Xing H, Xie DX, Lu YP, Zhou JF, Ma D. Zhonghua Zhong Liu Za Zhi. 2009;31(3):178-82.
22. Smith J, Tho LM, Xu N, Gillespie DA. Adv Cancer Res. 2010;108:73–112.

	***Miss M. Nayak*** *is currently the Senior Research Fellow (SRF) of Homi Bhabha National Institute (HBNI). She joined Radiation & Photochemistry Division, BARC in 2021 for PhD programme after completion of her M.Sc. in Zoology. She is working on the redox biology organoselenium compounds with an aim to develop potent chemotherapeutic agent for lung cancer.*
	***Miss J. Aishwarya*** *received her M.Sc. by research in Medical Biochemistry from Jawaharlal Institute of Medical Education and Research (JIPMER), Puducherry in 2021. She is currently pursuing her Ph.D. from Advanced Centre for Treatment Research and Education in Cancer (ACTREC), Navi Mumbai in collaboration with BARC, Mumbai in the domain of cancer biology. Her work essentially focuses on development of selenium based nanotherapeutics for the treatment of glioblastoma multiforme.*
	***Dr. Beena G. Singh,*** *Scientific Officer/G in the Radiation and Photochemistry Division, BARC. Her main area of interest is investigating the reaction mechanism of radiation induced redox reactions of organic molecules/nanoparticles and development of drug delivery systems. She is the recipient of Carl Storm International Diversity Award from the organizers of Gordon Research Conference in Radiation Chemistry (2012), Scientific & Technical Excellence Award (2015) and Group Achievement Award (2017) from Department of Atomic Energy.*
	***Dr. Atanu Barik*** *joined Radiation & Photochemistry Division, BARC after graduating from BARC Training School in 2000. He has obtained Ph.D. degree in Chemistry from University of Mumbai in the year 2006. During the year 2007-2008 he was post-doctoral fellow at Laboratoire de Radiolyse, CEA Saclay, France. He was the recipient of DAE young scientist award and group achievement award in the year 2009 and 2017 respectively. He is also associated with Homi Bhabha National Institute, Mumbai as an Associate Professor. His current research activities focus on free radical chemistry and excited state properties of molecules employing photochemical and radiation chemical techniques. Email: atanu@barc.gov.in*
	***Dr. Amit Kunwar*** *joined Radiation & Photochemistry Division, BARC in 2005 after graduating from BARC Training School (48th Batch, Bioscience discipline). After completing Ph.D. from Homi Bhabha National Institute in 2010, he received "Richard and Edith Strauss Postdoctoral Fellowship in Respiratory Medicine" to pursue postdoctoral research at Meakins Christie Laboratories, McGill University, Montreal, Canada, 2012-2014. He is the recipient of "Outstanding Doctoral Thesis Award" from Homi Bhabha National Institute, "Young Scientist Award" from DAE, "Young Scientist Award" from Indian Academy of Biomedical Sciences and "Homi Bhabha Science & Technology Manpatra Award" from DAE. He is the fellow of Maharashtra Academy of Sciences.*

INDIAN SOCIETY FOR RADIATION AND PHOTOCHEMICAL SCIENCES
(Reg. No. 617/1985, GBBSD, Bombay; Trust No. F-10965)
Radiation & Photochemistry Division
Bhabha Atomic Research Centre, Mumbai - 400 085

Member Enrolment Form

1. Name in Block Letters:
2. Date of Birth:
3. Highest Academic Qualification:
4. Present Position:
5. Addresses:

Photograph

Office	Residence
Telephone E-mail	Telephone E-mail

6. Address for Correspondence: Office / Residence
7. Category of Membership Applied for: Annual / Life /Corporate member

Category	Fees	Admission fee	Total Amount
Annual	Rs 200/-	Rs 100/-	Rs 300/-
Life Member	Rs 2000/-	Rs 100/-	Rs 2100/-
Corporate Member	Rs 20000/-	Rs 1000/-	Rs 21000/-

8. *Remittance: DD in favour of 'ISRAPS' payable at MUMBAI
For Bank Transfer:
A/c No.10536133801, SBI, BARC Branch, IFSC SBIN0001268
(e-mail the money transfer details along with the details requested above to: **israps.secretary@gmail.com** and copy to **mathip@barc.gov.in)**
**Payment can be made after the approval of application by Secretary, ISRAPS*

9. Brief Resume of activities and research interests:
(min. 500 words, in a separate attachment)
10. List of memberships of other professional bodies, if any:
11. List of prizes/awards/fellowships received, if any:
12. Number of Publications
(Pl. attach complete list)

I agree to abide by the constitution and bye-laws, and rules and regulations of the SOCIETY.

Place:

Signature

Date:

Published by ISRAPS, C/o RPCD, BARC, Mumbai 400 085

Designed and Printed at **Ebenezer Printing House**
Tel.: 2446 2632/3872 E-mail: outworkeph@gmail.com